

分类号: O572
密 级: 公开

单位代码: 10422
学 号:



山东大学
SHANDONG UNIVERSITY

博士学位论文

Dissertation for Doctoral Degree

论文题目: Measurement of the π^0 Inclusive Cross
Section in ep Scattering and the Design of Electromagnetic
Calorimeter for SoLID Program at Jefferson Lab

作者姓名 田野
培养单位 前沿交叉科学研究院
专业名称 粒子物理与原子核物理
指导教师 冯存峰 教授
合作导师 Jian-ping Chen Senior Staff Scientist

A Dissertation Submitted to Shandong University for the Degree of Doctor

**Measurement of the π^0 Inclusive Cross
Section in ep Scattering and the Design of
Electromagnetic Calorimeter for SoLID
Program at Jefferson Lab**

Ye Tian

Prof. Cunfeng Feng
Co Supervisor:
Senior Staff Scientist Jian-ping Chen

Contents

ABSTRACT	XI
摘要.....	XIV
ABBREVIATIONS	XV
1 Introduction	1
1.1 Introduction of QCD.....	1
1.2 Nucleon structure.....	3
1.2.1 Spin and mass of nucleon	3
1.3 Study the nuclear structure with electromagnetic probe method.....	5
1.4 Upgrade project in JLab	7
2 Introduction of SoLID program and generator	9
2.1 The physics target of SoLID.....	9
2.1.1 The SIDIS program	10
2.1.2 The PVDIS program.....	11
2.1.3 The J/ψ program	11
2.2 Monte Carlo (MC) event generator in SoLID program.....	12
2.2.1 Monte Carlo generator introduction	13
2.2.2 The Wiser generator	14
2.2.3 The modified Hall D MC generator	14
2.2.4 Comparison	19
2.3 The motivation of π^0 cross section measurement	20
2.4 DVCS experiment in JLab	21
2.4.1 DVCS process introduction.....	21
2.4.2 The DVCS experiment.....	21
3 The experimental setup	24
3.1 The Continuous Electron Beam Accelerator Facility (CEBAF)	25

3.2	Hall A general instrument.....	26
3.2.1	The beam line	27
3.2.2	The Target System	30
3.3	The High Resolution spectrometer(HRS).....	32
3.4	The DVCS Electromagnetic Calorimeter	34
3.5	The Data Acquisition (DAQ) System	36
3.5.1	General Hall A Data Acquisition System.....	36
3.5.2	DVCS calorimeter DAQ system.....	37
3.5.3	The trigger system	38
4	The strategy for extracting inclusive π^0 cross section from DVCS experiment data	41
4.1	Basic principle to extract inclusive π^0 cross section.....	41
4.2	The data analysis of DVCS experiment	43
4.2.1	Exclusivity of the DVCS process by missing mass method.....	43
4.2.2	DVCS event selection	44
4.3	The inclusive π^0 events in DVCS experiment data	45
4.4	Restriction and problems in using DVCS data.....	46
4.4.1	Low energy photon	46
4.4.2	Vertex of π^0	47
4.4.3	Calorimeter geometry acceptance of π^0	47
4.4.4	Target window.....	48
4.5	Event selection cut for π^0 analysis	48
4.5.1	Trigger.....	48
4.5.2	Electron identification.....	49
4.5.3	Tracking and S2m scintillator.....	50
4.5.4	Vertex.....	51
4.5.5	Beam current	52
4.6	Summary.....	53
5	DVCS Calorimeter analysis and calibration	55
5.1	Waveform analysis	56
5.1.1	Baseline fitting	56
5.1.2	One-pulse fitting.....	57
5.1.3	Two-pulse fitting.....	58

CONTENTS

5.1.4	Waveform analysis optimization	59
5.2	Calorimeter time calibration and optimization	60
5.2.1	ARS stop trigger jitter.....	62
5.2.2	Calorimeter block time offset	62
5.2.3	S2m scintillator paddle offset	63
5.2.4	Propagation time in scintillator	63
5.2.5	Electron path/momentum in LHRS.....	63
5.2.6	Time walk correction.....	65
5.2.7	Conclusions	65
5.3	Calorimeter Energy Calibration	66
5.3.1	Cosmic rays uniformity calibration.....	66
5.3.2	Elastic calibration	67
5.3.3	Radiation damage calibration by π^0 event	68
5.3.4	Low energy photon correction	71
5.3.5	Summary	71
5.4	Cluster algorithm	72
5.4.1	Pulse selection in bunch	72
5.4.2	Build cluster with cellular automaton algorithm.....	73
5.4.3	Cluster reconstruction	75
5.5	Summary.....	76
6	Inclusive π^0 cross section extraction	77
6.1	Data used in analysis	77
6.2	Calorimeter cut.....	78
6.2.1	Photon energy cut	79
6.2.2	Calorimeter Geometry cut	80
6.2.3	Beam bunch selection	80
6.2.4	Time difference between two photons	80
6.2.5	ϕ angle cut on π^0	82
6.2.6	π^0 cut.....	82
6.3	Charge calculation.....	83
6.4	Simulation	84
6.4.1	Generator description	84
6.4.2	Vertex distribution along target (Z dependence)	85

6.4.3	Target window simulation.....	86
6.4.4	Detector simulation process	87
6.4.5	π^0 yield from simulation.....	88
6.5	Data analysis.....	90
6.5.1	Vertex assumption.....	91
6.5.2	Vertex weight.....	91
6.5.3	Extract π^0 events yield from fitting	92
6.5.4	Extract π^0 s from three clusters events.....	93
6.5.5	π^0 s yield in data.....	95
6.5.6	Dummy target data.....	95
6.6	Result.....	96
6.6.1	π^0 cross section result	97
6.6.2	Comparison of two 4-pass results.....	97
6.7	Error estimation.....	98
6.7.1	Statistical error	101
6.7.2	Systematic uncertainty error.....	102
6.8	Summary and discussion	106
7	The SoLID spectrometer and Electromagnetic Calorimeter.....	108
7.1	General description of SoLID detectors	108
7.1.1	SIDIS configuration.....	109
7.1.2	PVDIS configuration	110
7.1.3	SoLID spectrometer function and requirement.....	112
7.2	SoLID ECal.....	113
7.2.1	Desired performance and challenge	113
7.2.2	Shashlik ECal design.....	115
7.2.3	Scintillator Pad Detector(SPD)	118
8	Electromagnetic calorimeter principle.....	120
8.1	The Electro-magnetic Calorimeter.....	120
8.1.1	The light yield of SoLID Ecal.....	122
8.2	Scintillator.....	123
8.3	Wave length shifting(WLS) fiber.....	124
8.4	PMT.....	126
8.5	Summary.....	128

CONTENTS

9	Material Selection of ECal Prototype and assembly	129
9.1	Scintillator.....	130
9.2	Reflective layer.....	130
9.2.1	Tyvek paper	131
9.2.2	Powder coating.....	132
9.2.3	3M TM Enhanced Specular Reflector(ESR)	133
9.3	Fiber.....	133
9.3.1	Fibers selection	134
9.3.2	Fiber end mirror	135
9.3.3	Fiber connection and polishing	137
9.4	Assembly	138
9.5	The material of shashlik prototype module.....	139
9.6	Summary.....	140
10	ECal prototype detectors test result.....	141
10.1	PMT test	141
10.1.1	PMT test setup	142
10.1.2	SPE gain	143
10.1.3	Maximum linear current.....	145
10.2	Cosmic ray test system.....	146
10.2.1	Cosmic ray test setup and DAQ	147
10.2.2	Flash Analog-to-Digital Converter(FADC).....	147
10.3	Cosmic test result.....	148
10.3.1	Shashlik ECal test result.....	148
10.3.2	Preshower test result.....	150
10.4	Beam test	150
10.4.1	A preliminary beam test in JLab Hall A.....	152
10.5	Summary.....	154
11	Conclusion and outlook	155
	APPENDIX.....	157
A.	Large-angle SPD(LASPD) time resolution test	157
A..1	"Three-bar test" of trigger scintillators.....	157
A..2	LASPD test.....	159
	REFERENCES.....	162

ABSTRACT

One of the key goals in high- and medium-energy hadronic physics is to study the internal structure of the nucleon and to understand how QCD works in the non-perturbation region. The subatomic structure of the nucleon remains a frontier topic in hadronic physics research. The goal of the nucleon structure study is to understand how quarks and gluons form the nucleon's energy/momentum and its spin. For this topic, the primary experiment tool used is electron scattering from a nucleon or a light-nuclear target. Recently, as advancement in electron scattering and in experimental setup that can allow higher and higher statistics, understanding the nucleon structure has advanced from extracting the momentum-dependent (1D) PDF to a more comprehensive view: the 3D structure of the nucleon. Semi-inclusive deep inelastic scattering (SIDIS) is used as the main experimental tool to access the nucleon 3D structure functions such as transverse-momentum distribution (TMD) functions.

In studying the internal structure of the nucleon, one of the frontier facility worldwide is Thomas Jefferson National Accelerator Facility, or Jefferson Lab (JLab), located in Newport News, Virginia. Electron scattering is a unique tool in subatomic physics study, providing unambiguous information on the nucleon structure that cannot be achieved by other methods such as hadron-hadron collisions or pure leptonic reactions. The superconducting continuous-wave electron accelerator at JLab provides the highest electron-scattering luminosity of the world. Its luminosity can reach up to $10^{39} \text{ cm}^{-2} \text{ s}^{-1}$ for unpolarized targets, and up to $10^{36} \text{ cm}^{-2} \text{ s}^{-1}$ for polarized-target experiments. In addition, JLab has just completed its upgrade and can now provide up to 11 GeV in beam energy to 3 of the 4 experimental halls (A, B and C), and up to 12 GeV to experimental Hall D. The high luminosity and this recent energy upgrade of JLab has made it possible to provide high-precision data in unprecedented areas.

A high-intensity, large-acceptance spectrometer called SoLID (Solenoid Large Inten-

sity Device) is planned for JLab's experimental Hall A, which contain three main physics programs: Semi-Inclusive Deep Inelastic Scattering (SIDIS), Parity-Violating Deep Inelastic Scattering (PVDIS) and J/ψ program.

This dissertation contains two main topics, both are central to the SoLID program at JLab. The first topic is a measurement of the π^0 inclusive cross section in e+p scattering process, where the photons decayed from π^0 are the important background in SoLID experiment. The second topic is to research and design one shashlik-type electromagnetic calorimeter (ECal) for SoLID experiment.

The DVCS(Deeply Virtual Compton Scattering) experiment E12-06-114 of JLab is one of initial experiments after 12 GeV upgrade in Hall A. Due to no special π^0 cross section experiment, this E12-06-114 experiment, including kinematic configuration kin48_2, kin48_3, kin48_4, is used to measure the inclusive π^0 cross section in this dissertation. Thanks to the DIS (Deep Inelastic Scatter) trigger mode and ARS (Analog Ring Sampler) digitizer of the calorimeter used this experiment, the inclusive π^0 events can be extracted from ARS recorded which anti-coincidence with LHRS electron trigger signal.

The Monte Carlo event generator of SoLID is a modifier generator of Hall D at JLab. The π^0 yield in the process of electron colliding with liquid Hydrogen target was simulated with this generator.

The π^0 events yield are measured in energy bin from 1 GeV to 8 GeV and each polar angle bin from 8 degree to 20 degree at 8.5 GeV and 11 GeV beam energy. The π^0 cross section of measured result are derived by comparing with the simulation results. This scale factor from comparison will be used to fix the generator simulation π^0 production in the future SoLID experiment.

The second work is to study the design of electromagnetic calorimeter (ECal) for SoLID spectrometer. SoLID's ECal will utilize a new sampling technique called the "shashlik" design, in which each module is made of 194 each of 0.5mm-thick lead and 1.5mm-thick scintillator layers. The light signal is guided out by wavelength-shifting (WLS) fibers penetrating through all layers through pre-drilled holes. The light of the module was guided into one photomultiplier tube by the fiber and transferred to electronic signal. Such technique provides a good balance between particle ID capability, energy resolution, radiation hardness, and cost. Total 2000 modules will be built as plan, which will be an onerous work.

The energy resolution of ECal is greatly influenced by the statistics of light yield, and

ABSTRACT

the design study in this dissertation is mostly focus on the improvement of light yield. We studied the material selection, light collection, machining process and the assembly. A few prototypes of this shashlik ECal have been assembled with varied scintillator material, fiber type, fiber end mirror, reflector layer and package layer. To measure the light yield, few testing system was built for testing the performance of the PMT and the light yield of ECal prototype.

In this dissertation, from chapter 2 to 6 will describe the inclusive π^0 cross section measurement work, the chapter from 7 to 10 is the design and test of SoLID ECal.

Keywords: π^0 inclusive cross section, SoLID, Electromagnetic Calorimeter, ECal, shashlik, light yield

摘要

高能和中高能强子物理的一个关键目标是研究核子的内部结构和理解量子色动力学在非微扰区域是如何工作的。核子的亚原子结构仍然是强子物理研究的前沿课题。核子结构研究的目的是了解夸克和胶子如何形成核子的能量或动量以及自旋。对于这些课题的研究,通过电子散射轻的核子靶的过程是主要实验工具。最近,随着电子散射和实验设备的进步,可以允许越来越高的统计量,对核子结构的理解已经从提取一维动量 PDF 到一个更全面核子的三维结构。通过深度非弹性散射 (SIDIS) 为主要实验工具,可以获得横向动量分布 (TMD) 等核子的三维结构函数。

在核子内部结构的研究实验中,位于弗吉尼亚州纽波特纽斯的托马斯杰斐逊国家加速器实验室,或称做 JLab,是世界范围内的前沿实验室之一。电子散射是亚原子物理研究中一个独特的工具,提供了核子结构的明确信息,这是其他方法如强子-强子碰撞或纯轻子相互作用无法实现的。JLab 的超导连续电子加速器提供了世界上最高的电子散射亮度。非极化靶的亮度可达 $10^{39} \text{ cm}^{-2} \text{ s}^{-1}$,极化靶的亮度可达 $10^{36} \text{ cm}^{-2} \text{ s}^{-1}$ 。此外,JLab 刚刚完成了能量升级,现在可以向 4 个大厅中的 3 个 (A、B 和 C) 提供 11 GeV 能量的束流,以及向实验大厅 D 提供 12 GeV 能量束流。JLab 的高亮度和近期的能量升级为之前没有研究过的方面提供了高精度数据的可能。

JLab 的 A 实验大厅计划建造使一个能接受高亮度高探测器接受度的 SoLID(螺线管型高密度装置)谱仪装置。该谱仪包含三个主要物理项目:半单举深度非弹性散射 (SIDIS)、宇称破缺的深非弹性散射 (PVDIS) 和 J/ψ 项目。

这篇论文包含两个主要的课题,都与 JLab 的 SoLID 项目密切相关。第一个课题是 e+p 散射过程中单举 π^0 截面的测量,其中 π^0 衰变产生的光子是 SoLID 实验的重要背景。第二个课题是研究和设计一种用于 SoLID 实验中 shashlik 型取样量能器。

JLab 的 DVCS(深度虚光子康普顿散射)实验 E12-06-114 是 12 GeV 升级后,

在 A 厅进行的初始实验之一。由于没有专用的 π^0 截面测量实验，本论文使用 E12-06-114 实验中 kin48_2、kin48_3 和 kin48_4 设置的实验数据测量单举 π^0 的截面。得益于实验中的 DIS 触发模式和波形采样电子学插件 ARS， π^0 可以从与 LHRS 电子触发信号不符合的 ARS 的时间窗口中提取。

SoLID 所用的蒙特卡罗产生子是通过修改 JLab Hall D 的产生子获得的。电子打液态质子靶过程中 π^0 的产额可以用这个产生子模拟获得。

π^0 测量的能量范围从 1 GeV 到 8 GeV，角度是从 8 度到 20 度，该测量包括 8.5GeV 和 11GeV 两个束流能量的测量。实验数据中的截面是通过与模拟结果相比较获得的。该比值将会用于修正产生子中的截面，以及模拟中 π^0 的产额。

第二部分是 SoLID 项目中电磁量能器的设计。SoLID 的电磁量能器将采用一种名为“shashlik”的新型采样设计，每个模块由 194 个 0.5mm 厚的铅和 1.5mm 厚的闪烁体层组成。光信号由波长位移光纤引出，通过预先的钻孔穿透所有层。该模块产生的光通过光纤引导并收集到光电倍增管，最终转换成电信号。这种取样型量能器技术在粒子鉴别能力、能量分辨率、抗辐照性能和成本之间提供了良好的平衡。按计划，总共 2000 个模块将被建造，这将会是一项繁重的工作。

光产额的统计量对 ECal 的能量分解有很大的影响，本文对量能器的设计和研究主要体现在光产量的提高上。我们研究了材料的选择、光的收集、加工工艺和组装。几个 shashlik ECal 原型已经装配完成，分别采用了不同的闪烁材料、光纤、光纤端面反射层、反射层和封装。为了测量光产额，建立了测试 PMT 性能和 ECal 样机光产额的测试系统。

在本文中，从第 2 章到第 6 章将描述单举 π^0 截面的分析工作，第 7 章到第 10 章是 SoLID 的 ECal 的设计和测试工作。

关键词: 单举 π^0 截面测量，SoLID，电磁量能器，shashlik，光产额

ABBREVIATIONS

ADC	Analog to Digital Converter
ARS	Analog Ring Sample
BCM	Beam Current Monitor
BPM	Beam Position monitor
CEBAF	Continuos Electron Beam accelerator Facility
CODA	CEBAF Online Data Acquisition
DAQ	Data Acquisition
DIS	Deep Inelastic Scattering
DVCS	Deeply Virtual Compton Scattering
ECal	Electromagnetic Calorimeter
EPA	Equivalent Photon Approximation
ESR	Enhanced Specular Reflector
FA-	Forward Angle
FADC	Flash Analog to Digital Convertor
GC	Gas Cherenkov
GEM	Gas Electron Multiplier
GPD	Generalized Parton Distribution
HRS	High Resolution Spectrometer
HV	High Voltage
JLab	Thomas Jefferson National Accelerator Facility
LA-	Large Angle
LED	Light Emitting Diode
LH_2	Liquid Hydrogen (target)
LHRS	Left High Resolution Spectrometer

ABBREVIATIONS

MaPMT	Multi-anode Photo-Multiplier Tube
MC	Monte Carlo
MRPC	Multi-gap Resistive Plate Chamber
NPE	Number of Photon Electron
PDG	Particle Data Group
PID	Particle Identification
PMT	Photo-Multiplier Tube
PR	Pion Rejector
PVDIS	Parity-Violating Deep Inelastic Scattering
QCD	Quantum Chromodynamics
QDC	Charge to Digital Converter
S2m	Scintillator paddles in LHRS
SIDIS	Semi-Inclusive Deep Inelastic Scattering
SoLID	Solenoidal Large Intensity Device
SPD	Scintillator Pad Detector
SPE	Single Photo-Electron
TDC	Time to Digital Converter
TMD	Transverse Momentum Dependent
TOF	Time of flight
VDC	Vertical Drift Chamber
WLS	Wave-Length Shifting

Chapter 1

Introduction

The strong interaction, as one of four fundamental interactions, confines the quarks and gluons in nucleon, which contributes to the 99% of visible mass in the universe[1]. The Quantum Chromodynamics (QCD) is a theory developed to describe the strong interaction, and is a part of standard model. In QCD, the quarks and gluons are treated as fundamental degree of freedom, quarks interacts with each other through gluon exchange. The QCD theory has a rapid development in last several decades, however, the complexity of non-perturbative QCD is still a challenging to understand and observe in experiment.

1.1 Introduction of QCD

The origin of QCD can be traced back to 1964, when Gell-Mann[2] and Zweig introduced the quark conception to categorize the hadron. The quark conception is put forward with three flavors of quarks(u, d and s) and explained the "eight-fold way". They are awarded the Nobel Prize in 1969.

In 1969, Feynman put forward the parton model[3], and also described the behavior of hadron when it moves close to the speed of light, this shows the prospect of hadron collision experiment at high energy. At same year, first deep-inelastic scattering (DIS) experiment was carried out in SLAC. It shows the first evidence of the quark's existence, and also predicted the "Bjorken Scaling"¹[4]. The Nobel Prize was awarded to this exper-

¹The subsequent experiment result shows at large Q^2 and small x , this scaling is violated, implying the existence of gluon.

imental measurement in 1990.

in 1973, Gross, Politzer and Wilczek[5][6] discovered a property of the strong interaction by the non-Abelian gauge theories, which explains why quarks may behave almost as free particles only at high energies. The discovery laid the foundation for the theory of QCD. They are awarded the Nobel Prize in 2004.

Since QCD is a non-abelian gauge theory, and the gluon that has color charge as the mediator of the strong interaction, there are two special and famous features of QCD: the asymptotic freedom and the color confinement.

The asymptotic freedom could be described by the strong coupling constant α_S . In fact, it's not a constant, the value become large at low energy regime and decreases at high energy, which is shown in Fig.1-1 as a function of the energy Q. For the energy that infinitely large, the value of α_S is close to 0, the gluons and quarks will behave freely. For low energy region, the quark and gluons are confined in the nucleons and mesons, called QCD confinement, and in this region, the perturbative calculation is invalidated, make it hard to calculate the hadronic property from the first principle.

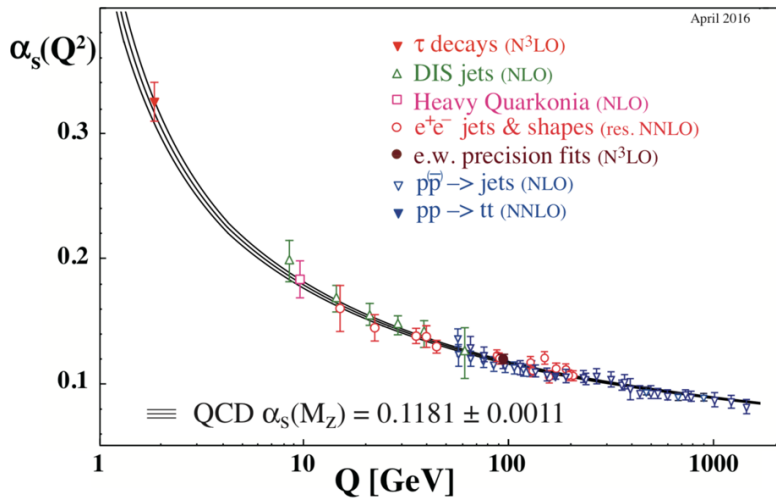


Figure 1-1: Summary of measurements of the strong coupling constant α_S as a function of the energy scale Q. The respective degree of QCD perturbation theory used in the extraction of s is indicated in brackets (NLO: next-to-leading order; NNLO: next-to-next-to leading order; res. NNLO: NNLO matched with resummed next-to-leading logs; N3LO: next-to-NNLO). The figure is acquired from [7].

Although in high energy regime, the quark and gluon behave freely, because of the

color confinement, we can't observe the single quark/gluon. The color confinement tell us that the quarks and gluons carry color charges, described through the Lund string fragmentation model[8]. When the quark or anti-quark has enough energy to move apart from hadron, the string's energy will increase until enough high to create a new quark-antiquark pair. As a result of this process, instead of seeing the individual quarks, new neutral color hadrons are generated, which is called hadronization.

1.2 Nucleon structure

The most fundamental theory to describe the nucleon structure is called Wigner distribution $\rho(x, \vec{b}_T, \vec{k}_T)$ [9], where x is longitudinal momentum fraction, \vec{b}_T is the parton transverse coordinate, and \vec{k}_T is the parton transverse momentum. It is a 5D quantum phase space distribution, related to the generalized transverse-momentum-dependent (GTMD) parton distribution, shown in Fig.1-2. By integrating over the \vec{k}_T , it's the impact-parameter-dependent (IPD) distribution. The generalized parton distribution (GPD) is related to IPD through the Fourier transformation. The GTMD is integrating over the \vec{b}_T will get the transverse-momentum-dependent (TMD) distributions. The TMD, GPD and IPD are 3D description of nuclear structure, establishing a bridge to the study of Wigner distribution. The parton distribution function (PDF) is acquired by integrating the transverse variable of TMD and GPD.

The Wigner distribution shows a full image of nucleon structure, however this 5D distribution couldn't be measured directly in experiment. Two important 3D distributions: TMD and GPD, could be performed experimentally to get a view of the nucleon structure. The TMD could be measured by the Drell-Yan process[10] and the semi-inclusive DIS (SIDIS) process. The GPD could be measured by the deeply virtual Compton scattering (DVCS) process, and the data used in the analysis of this thesis is from DVCS measuring experiment, more detail of this experiment will be described later.

1.2.1 Spin and mass of necleon

The original quark model show the nucleon spin is contributed by the quarks only. In the 1980s, the European Muon Collaboration (EMC) carried out a DIS experiment with polarized muon beam on a hydrogen target[11], and the result shows the quark only

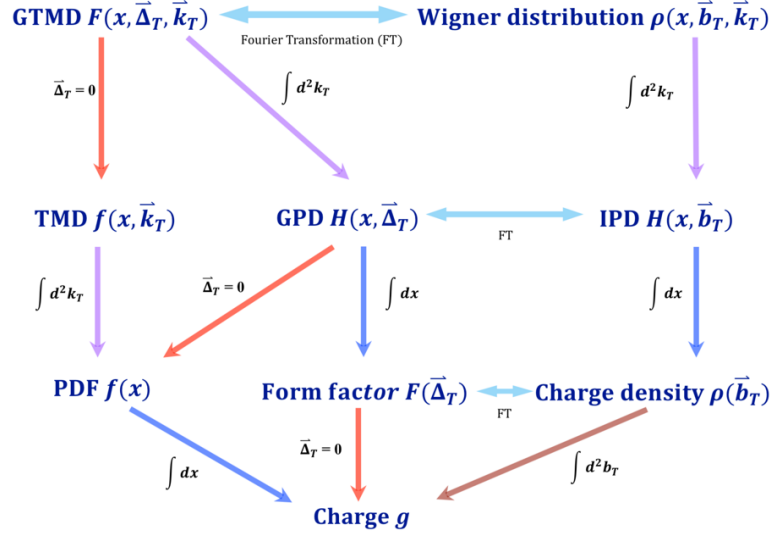


Figure 1-2: The nucleon structure from Wigner distribution to charge: how the transverse-momentum-dependent (TMD) distributions, the generalized parton distribution (GPD), the impact-parameter-dependent (IPD) distribution, and the parton distribution function (PDF) extracted from the Wigner distribution.

carry a small part of nucleon spin. This surprising result is known as "proton spin crisis". Present measurement shows the quarks' spin only contribute to 30% of total nucleon spin[12][13].

To understand the nucleon spin, different spin sum rules are put forward, which add the contribution of gluons. The first sum rule is proposed by Jaffe and Manohar[14]

$$\frac{1}{2} = L_q + \frac{1}{2}\Delta\Sigma + L_g + \Delta G \quad (1-1)$$

where L_q and $\Delta\Sigma$ are the orbital angular momentum (OAM) and spin angular momentum of quarks separately, L_g and ΔG are the orbital angular momentum (OAM) and spin angular momentum of gluons.

In 1997, Ji put forward a different sum rule, which is gauge invariant:

$$\frac{1}{2} = J_q + J_g = \frac{1}{2}\Delta\Sigma + L_q + J_g \quad (1-2)$$

where L_q and $\Delta\Sigma$ have same definition as Jaffe and Manohar's sum rule, J_g represents the total angular momentum of the gluons, which can't be decomposed to OAM and spin term.

Since these compositions are not gauge independent except L_q , they can't be measured directly, but we can measure other quantities that related to these compositions.

1.2.1.1 Mass

We know clearly the mass of nucleon, but how the nucleon acquire its mass from its constituents is still a mystery. The nucleon is composed of quark and gluon: the quarks have mass and gluons not. The quark get its mass though Higgs mechanism[15], which shows the sum of quarks' mass merely only contribute 1% of a proton or neutron's mass. From the recent theory model, the lattice QCD[16] tell us the mass of proton is shared with four separate contributions[17]: the quarks masses, the kinetic and potential energy of the quarks, the kinetic and potential energy of gluons and the conformal anomaly.

If we ignore the mass of quark, nearly all visible mass in the universe comes from the dynamics of quarks and gluons. The understanding of the nucleon mass is an important part of standard model, and help to understand and improve the lattice QCD.

1.3 Study the nuclear structure with electromagnetic probe method

One of most important experimental tools to study the nuclear structure is using the electromagnetic scattering, especially the lepton-nucleon deep inelastic scattering (DIS), which could be described as $l + N \rightarrow l' + X$. For the most simple situation that electrons scattered by the nucleon, as shown in Fig.1-3, a virtual photon q is assumed to transfer energy between electron and nucleon.

To describe this process, some important kinematic variables are defined as the following:

- The energy of virtual photon, equal to the energy loss of the electron, and energy transferred to the nucleon.

$$\nu = E - E' = E'_t - M \quad (1-3)$$

- The square of virtual photon' 4-momentum. It described the spatial resolution of the electromagnetic probe. Usually written as:

$$Q^2 \equiv -q^2 \quad (1-4)$$

- The invariant mass of the recoiling system W :

$$W = \sqrt{(P + q)^2} = \sqrt{M^2 + 2M\nu - Q^2} \quad (1-5)$$

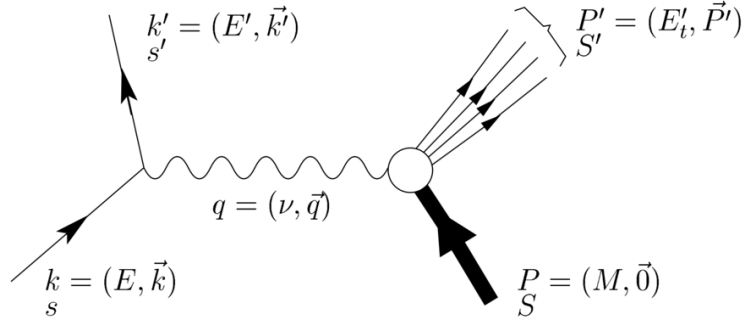


Figure 1-3: Electron scattering through a virtual photon and kinematic variable definition.

The incident electron has the 4-momentum $k=(E, \vec{k})$, and $k'=(E', \vec{k}')$ after scattering. The virtual photon with 4-momentum $q=(\nu, \vec{q})$. The still nucleon target with mass M is described as $P=(M, \vec{0})$ and $P'=(E', \vec{P}')$ separately. s and S are the spin of electron and nucleon target.

- For Deep-Inelastic Scattering process, the Bjorken scaling variable x_{Bj} describe the fraction of the nucleon's momentum carried by the struck quark in the light-cone frame. The x_{Bj} is defined as:

$$x_{Bj} \equiv x = \frac{Q^2}{2M\nu} = \frac{k}{P} \quad (1-6)$$

where k is the 4-momentum of the struck quark. As its name suggests, it shows the scaling character of the reaction to the first order.

With the help of these new variables, the cross section of electron nucleon scattering could be described as a function of Q^2 and ν . For the inclusive electron scattering measurement on a light nuclear target, which only the scattered electron is detected, the cross section is shown in Fig.1-4. From low invariant mass W to high, the spectrum go through different excitation states, including elastic scattering, quasi-elastic scattering, resonance and deep inelastic scattering region[18].

- The elastic scattering $e + A \rightarrow e + A$, A means the whole nucleus. After the scattering, the nucleus target in intact, the momentum of virtual photon is transferred to the whole nucleus.
- The quasi-elastic scattering $e + N \rightarrow e + N$, N means an individual nucleon. If the transferred energy ν larger than the binding energy between nucleons, a nucleon will be rejected from nucleus[19]. The study of quasi-elastic could explore the structure of nucleus.

- Resonance region $e + N \rightarrow e + N^*$. The quarks in nucleon absorb the virtual photon energy to form excitation state[20], which has the invariant mass $W^2 = M^2 + 2Mv - Q^2$. The first resonance state, as shown in Fig.1-4, is $\Delta(1232)$ with its mass $M_\Delta = 1.232\text{GeV}/c^2$. In this region, the structure of nucleon could be explored.
- Deep-inelastic scattering $e + q \rightarrow e + X$. It generally describes the scattering that $W > 2.3\text{ GeV}$ and $Q^2 > 1.0\text{ (GeV}/c)^2$. In this region, the virtual photon strikes on a quark, and this quark will be excited to generate new particles.

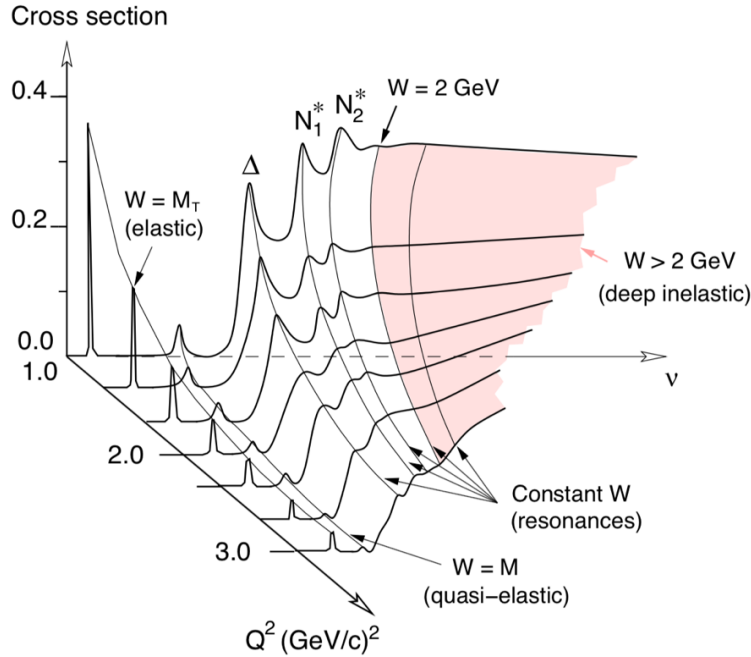


Figure 1-4: Cross section (in arbitrary unit) of inclusive electron in scattering on a light nuclear target as the function of v and Q^2 . M_T is the mass of the whole nucleus target, and M is the individual nucleon mass.

1.4 Upgrade project in JLab

Electron scattering is one of the most important experimental tools to probe the structure of matter. The current best electron scattering facility is Thomas Jefferson National Accelerator Facility, or JLab for short. The accelerator of JLab had been upgraded to the highest 12 GeV beam energy and the maximum current that can be delivered, summed over all four halls, is 200 μA .

The 12 GeV upgrade is accompanied by new detector upgrades. Although the currently envisioned program includes both high rate capability and large acceptance devices, there does not exist a single device capable of handling high luminosity (10^{36} – $10^{39} \text{cm}^{-2} \text{s}^{-1}$) over a large acceptance. The capabilities of the 12 GeV upgrade will not have been fully exploited unless a large acceptance high luminosity device is constructed. The SoLID (Solenoidal Large Intensity Detector) program is designed to fulfill this need. SoLID is made possible by developments in both detector technology and simulation accuracy and detail that were not available in the early stages of the 12 GeV program planning.

π^0 meson is the dominating background in most of SoLID experiments, and also affects the trigger design due to it decays two high energy gamma ray. This dissertation, from chapter 3 to 6, will present the π^0 inclusive cross section measurement in ep process by using the data of DVCS experiment E12-06-114 in JLab. The results are compared with the simulation results of SoLID generator in order to calibrate the generator.

The Shashlik type electromagnetic calorimeter is chosen as the SoLID electromagnetic calorimeter for electron identification. The second part of this dissertation, from chapter 7 to 10, studies this calorimeter, including material choice and assembly strategy. Few calorimeter prototypes have been assembled and tested by using cosmic ray.

Chapter 2

Introduction of SoLID program and generator

The SoLID (Solenoidal Large Intensity Device) is one part of Jefferson Lab (JLab) 12 GeV upgrade in Hall A. The SoLID program contains the whole experiments management, not only includes the device design and construction, but also the related physics study, the simulation of both experiments and detectors.

In this chapter, we will introduce the physical program in SoLID firstly, then the generator problem in SoLID simulation. To verify and correct the generator, we are trying to extract inclusive π^0 cross section from existing DVCS experiment data.

2.1 The physics target of SoLID

To fully exploit the potential of the JLab 12 GeV upgrade, the SoLID was proposed to a rich science program[21] that require both high luminosity and large acceptance. The SoLID apparatus are designed with two configurations: the "SIDIS" (Semi-Inclusive Deep Inelastic Scattering) configuration and the "PVDIS" (Parity-Violating Deep Inelastic Scattering) configuration, shown in Fig.2-1. More detailed introduction of SoLID detector will be described in Sect.7.1.

These two configurations are designed to satisfy 5 initially approved experiments: three SIDIS, one PVDIS and one J/ψ production, and also other low rated experiments.

New possible proposals are studying to expend the physics research of SoLID, such as the Time-like Compton Scattering (TCS) and the Double Deeply Virtual Compton Scattering (DDVCS) on GPD study. We will briefly introduce the three main physics program of SoLID, and more information about SoLID program could refer to the SoLID CDR [21].

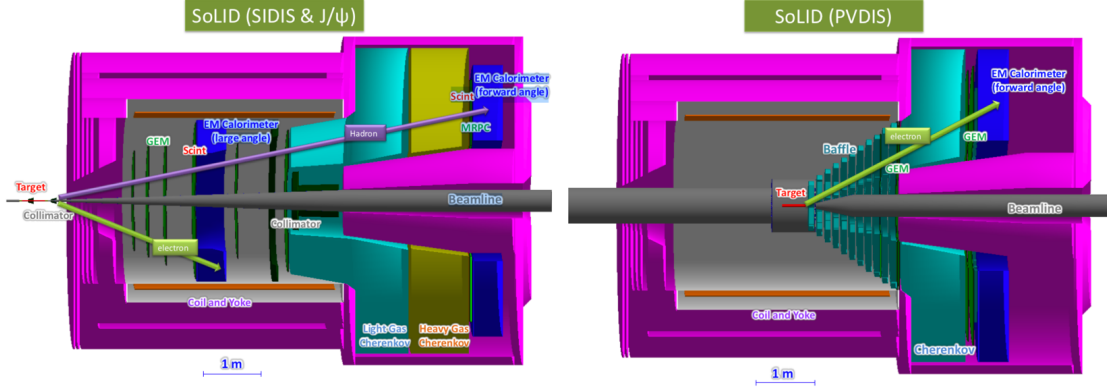


Figure 2-1: Left: SoLID SIDIS (and J/ψ) setup. Right: SoLID PVDIS setup.

2.1.1 The SIDIS program

The SIDIS program focus on the semi-inclusive charged pion production ($e + N \rightarrow e' + \pi^+/\pi^- + X$) to study the TMDs. As introduced in section 1.2, the TMDs describes the 3D momentum nucleon structure, help to reveal the full momentum and spin structure of the nucleon. The TMD function $f(x, \vec{k}_T)$ depend on both the longitudinal momentum fraction x and the transverse momentum \vec{k}_T . At leading twist (twist-two), there are eight TMD distributions, shown in Fig.2-2. When integrating over the transverse momentum of the quark \vec{k}_T , three are survived, they are both unpolarized, longitudinally polarized, and the transversely polarized quark distribution (transversity). The other five TMDs that vanish through \vec{k}_T integration, could provide important information about orbital angular momentum (OAM)[22] and constrain the nucleon spin sum rule.

This program includes three mains approved experiments: transverse ${}^3\text{He}$ [23], longitudinal ${}^3\text{He}$ [24] and transverse proton target[25]. Based on high luminosity and large acceptance of SoLID detectors, these TMD distributions will be measured with high precision.

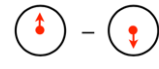
		Quark Polarization		
		U	L	T
Nucleon Polarization	U	f_1  unpolarized		h_1^\perp  Boer-Mulders
	L		g_{1L}  helicity	h_{1L}^\perp  longi-transversity (worm-gear)
	T	f_{1T}^\perp  Sivers	g_{1T}  trans-helicity (worm-gear)	h_1  transversity h_{1T}^\perp  pretzelosity

Figure 2-2: All eight TMDs at leading twist are categorized by the polarization of quark (f, g, h) and nucleon (U, L, T). The arrow out circle shows the nucleon spin, and arrow in circle is quark spin. The g_{1L} , for example, describe the probability that finding a longitudinally polarized quark inside a longitudinally polarized nucleon.

2.1.2 The PVDIS program

This program measure the parity-violating electroweak asymmetry APV in the deep-inelastic scattering of polarized electrons with high precision in order to search for physics beyond the Standard Model in lepton-quark neutral current interactions[26]. In electron-nucleon scattering, the atom parity-violating(APV) asymmetry could be measured by[27]:

$$A_{PV} = \frac{\sigma_R - \sigma_L}{\sigma_R + \sigma_L} \quad (2-1)$$

where σ_R and σ_L are the cross section of right and left handed electrons separately.

There are two other related measurements: the Charge Symmetry violation (CSV) at the quark level, and the higher-twist effects in the parity-violating asymmetry. All of them are the searching the physics beyond Standard Model, new discovery will reveal if these effects are large, otherwise the result shows the SM is reliable.

2.1.3 The J/ψ program

The main goal of J/ψ program is estimating the conformal anomaly contribution to the nucleon's mass. The anomaly contribution could be achieved by measuring the exclu-

sive electro-production of J/ψ near threshold on a proton[28]. This experiment detects exclusive reaction of electron-proton scattering that[29]

$$e + p \rightarrow e' + J/\psi(e^+, e^-) + p' \quad (2-2)$$

where the J/ψ is only detected through the (e^+, e^-) decay with 5.94% branch ratio. This reaction is also regarded as $\gamma^* + p \rightarrow J/\psi + p'$, which means a virtual photon is absorbed and generates the J/ψ particle. The virtual photon absorb energy is close to the threshold of J/ψ production energy, and the proposal of J/ψ measurement is shown in Fig.2-3.

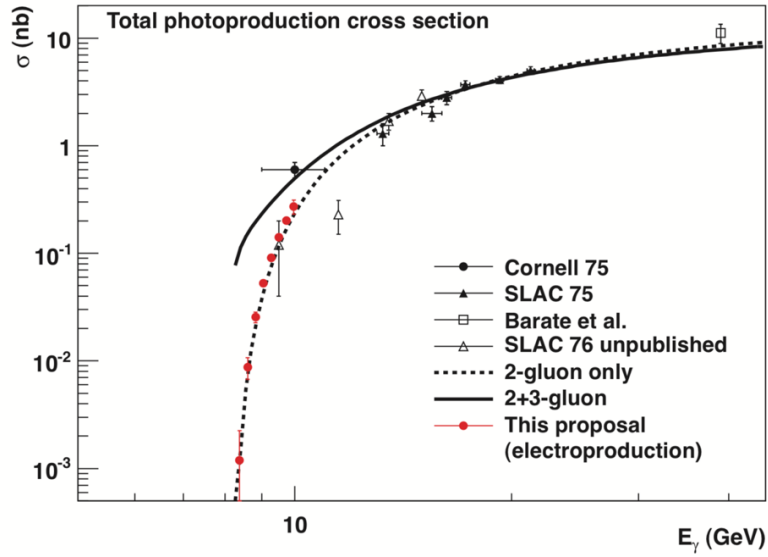


Figure 2-3: The total J/ψ photo-production cross section as a function of photon energy, except for the points of SoLID proposed electro-production measurement, which is as the function of equivalent photo energy. The model of J/ψ production interaction with nucleon is based on two or three gluon exchanges[30].

2.2 Monte Carlo (MC) event generator in SoLID program

The SoLID program deal with a very high rate experiment, and this high rate is main challenge of detector and trigger system design. The event rate could be estimated in simulation, based on the generator. An accurate generator will make sure the design of the detector and trigger system satisfy the SoLID requirement justly, and never failed in

real run situation or exceed the requirement with high cost.

The Wiser[31] generator has been widely used in other experiments of JLab to estimate the pion background since several decades ago. However, the comparison with data shows Wiser overestimates the background, and this high background is not acceptable for SoLID design. Then a modified Hall D MC generator is developed to apply for the SoLID generator, which shows a better consistence with data, and emphasized in the following content.

The background impact the physics result through three steps: the cross section, the online trigger and offline analysis. The cross section could be acquired from generator. To accept all the signal we need, the threshold of the online trigger is set very loose, which lead to a very high trigger rate. The background and accidental trigger could be subtracted from offline analysis, which highly suppress the background in trigger.

2.2.1 Monte Carlo generator introduction

Monte Carlo event generator provides fully exclusive simulations of everything that happens in high-energy collisions. They play an essential role in QCD modeling, in particular for aspects beyond fixed-order perturbative QCD. In data analysis, the generators are used together with detector simulation to provide a realistic estimate of the detector response to collision events and devise the analysis strategy. In the planning of new experiments, they are used to estimate signals and backgrounds in high-energy processes, and to study the requirement and imperfections of detector[7].

Since event generators must describe everything in explicit detail, they also necessarily cover less well understood physics. And some descriptions of physics are based on theory models, which may not perfect to describe the physics process. Each generator has slightly different origin, which emphasized on various physics aspects. Generally speaking, the generator is physics or model dependent. There are several general purpose Monte Carlo (GPMC) generators, such as Herwig[32], Pythia[33], Sherpa[34], which are widely used high energy physics experiment simulation. There are also a large number of other more specialized generators, just simulate one or several steps compared to general generator, mainly for some specific QCD physics process.

The generator is not only model dependent, but also parameters dependent in model. The generators are formulated in terms of effective parameters in model, however these

parameters are not determined or fitted by a limited amount of data. To check the accuracy of generator, specific data must be taken and are compared with the generator[35]. The generators, also the model, are developing with tuning the parameters according to the comparison with data.

2.2.2 The Wiser generator

Our first choice of generator is Wiser, which has been generally used in SLAC and JLab as pion background estimation in electron-production scattering experiment. The wiser code is based on the measurement of bremsstrahlung photon beam $\gamma + N \rightarrow X$ with 5, 7, 9, 11, 15 and 19 GeV energy electron on SLAC. Most of data were taken with a hydrogen target, also some deuterium data were taken. Pion, kaon, and proton are detected separately by the SLAC 8 GeV/c spectrometer. Since no neutral pion data is taken, the cross section of π^0 is assumed as the average cross section of π^- and π^+ :

$$\sigma_{\pi^0} = \frac{\sigma_{\pi^-} + \sigma_{\pi^+}}{2} \quad (2-3)$$

Wiser generator is modified from inclusive photon-production¹ data to apply for the electron-production². Comparing with pion data taken in JLab shows that Wiser code overestimates the pion rate by about a factor of two[36]. This high estimation rate of Wiser is not acceptable for SoLID detector design, which will exceed the 100k Hz "ceiling" trigger rate[21], and a more accurate generator is needed to perform the simulation.

2.2.3 The modified Hall D MC generator

Hall D MC generator[37] was studied and is modified as a potential candidate for SoLID experiment. The modified Hall D MC background generator gives better background results matching existing data, and used as SoLID hadron generator now, called as "bggen". The original Hall D generator is only a photo-production event generator. It uses various experimental data on a proton target(γP) to generate the photo-production cross section for photon energies below 3 GeV, and for photon energies above 3 GeV, it uses a modified version of PYTHIA. A simple comparison[38] of total photo-production

¹ γ beam hit the target. Both the data used in original Wiser and Hall D generator are photon-production data.

²Electron beam hit the target.

cross sections extracted from the Hall D generator agrees well with the PDG data[7] as shown in the Fig.2-4.

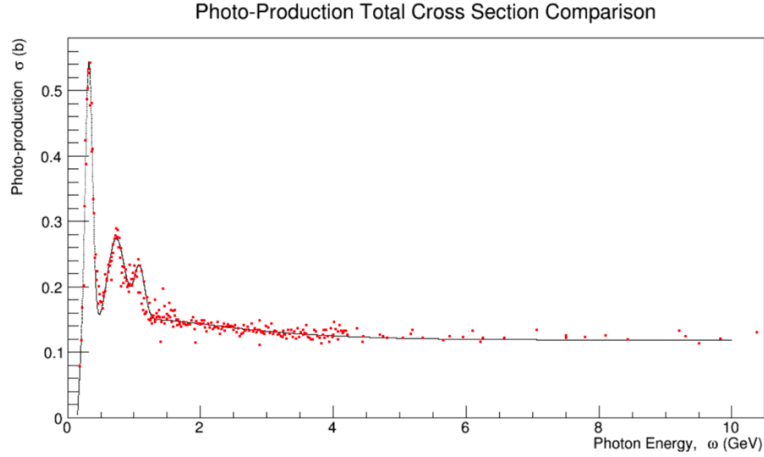


Figure 2-4: The comparison of photon-production cross section between Hall D generator and PDG. Black line: cross section from Hall D generator. Red points: from PDG.

SoLID experiment runs with electron beam, so it requires a electro-production MC generator. The Hall D MC generator is modified with similar method as Wiser generator to apply for the electron-production based on theory assumption. The assumption is described as: hadron production in electron scattering on a nucleon target can originate either from real bremsstrahlung photons radiated in the target or from the interaction of the virtual photon with the nucleons, which are called external and internal radiation separately. The following content will introduce these two radiation assumptions.

2.2.3.1 Hadron production with bremsstrahlung photons

This external part includes two processes: the electrons hit the target to generate the bremsstrahlung photons, then the bremsstrahlung photons interact with target to generate the secondary hadrons. The bremsstrahlung contribution is implemented following PDG, and the cross section of photon interaction with proton follows the Hall D generator.

As shown in Fig.2-5, the bremsstrahlung process dominate the electron energy loss if the electron energy above 100 MeV. A high energy electron loses energy by bremsstrahlung at a ratio nearly proportional to its energy. The cross section of the bremsstrahlung spectrum can be approximated as[39]:

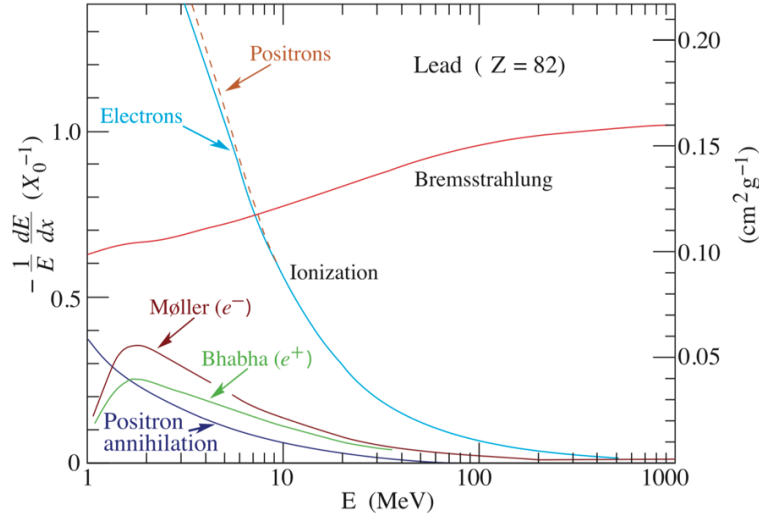


Figure 2-5: Fractional energy loss per radiation length in lead as a function of electron or positron energy.

$$\frac{d\sigma_{BREM}}{d\omega} = \frac{4\alpha r_e^2}{\omega} \left\{ \left(\frac{4}{3} - \frac{4}{3}y + y^2 \right) [Z^2(L_{rad} - f(Z)) + ZL'_{rad}] + \frac{1}{9}(1-y)(Z^2 + Z) \right\}, \quad (2-4)$$

where ω is energy of photon from bremsstrahlung, E is the energy of incident electron, $y = \omega/E$ is the fraction of the electrons' energy transferred to the radiated photon, $r_e = e^2/m_e c^2$ is classical electron radius, Z is atomic number, and L_{rad} and ZL'_{rad} is the constant. For small y , the last term in equation 2-4 ranges from 1.7% (low Z) to 2.5% (high Z) of the total. If we ignore it and take the definition of radiation length X_0 :

$$\frac{1}{X_0} = 4\alpha r_e^2 \frac{N_A}{A} \left\{ Z^2 [L_{rad} - f(Z)] + ZL'_{rad} \right\}, \quad (2-5)$$

we have

$$\frac{d\sigma_{BREM}}{d\omega} = \frac{A}{X_0 N_A \omega} \left(\frac{4}{3} - \frac{4}{3}y + y^2 \right). \quad (2-6)$$

To get the hadron production cross section due to bremsstrahlung photons, multiplying the photon-production cross section $\sigma_r(\omega)$ with the bremsstrahlung cross section,

$$d\sigma_{ep_BREM} = \sigma_r(\omega) N_{BREM}(\omega) \frac{d\omega}{\omega} \quad (2-7)$$

$$N_{BREM}(\omega) = \frac{1}{2} \times \frac{d}{X_0} \left(\frac{4}{3} - \frac{4\omega}{3E} + \frac{\omega^2}{E^2} \right) \quad (2-8)$$

where d is the relative radiation length of target, which is calculated as $d = \rho \cdot t$, ρ is density of target and t is the target thickness, the constant $1/2$ means using the average relative radiation length of the total target.

2.2.3.2 Hadron Production Approximated with the Equivalent Photon Approximation (EPA) method

The electro-production cross section from internal part is obtained using the Equivalent Photon Approximation (EPA) method[40]. The electron interacts with proton through a virtual photon, and the nucleon absorb the virtual photon to generate the secondary particles, which is shown in the left plot of Fig.2-6. The EPA method divide this process into two similar steps as bremsstrahlung: electron radiates "real" photon, then real photon interacts with proton. In this method, the virtual photon is regarded as a "real" photon and the cross section of which is based on the EPA. At the second step, that real photons interact with proton, the cross section is same as the bremsstrahlung photon. One restriction of EPA method is that it only works for proton target.

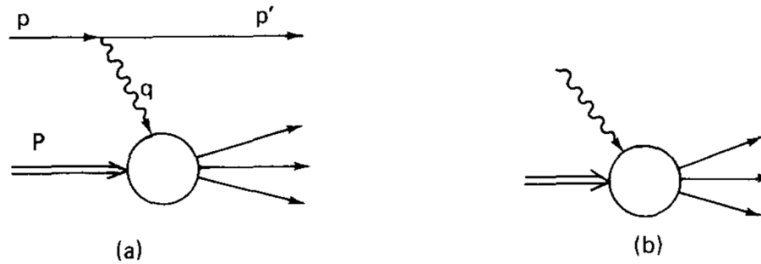


Figure 2-6: Electro-production(a) and photo-absorption(b) of Equivalent Photon Approximation method.

The idea of the equivalent photon approximation is put forwarded by Fermi[41][42], who paid attention to the fact, that the field of a fast charged particle is similar to an electromagnetic radiation. This radiation may be interpreted as a flux of photons distributed with some density $n(\omega)$ on a frequency spectrum. Therefore, the electromagnetic interaction of this particle with a nucleus is reduced to the interaction of photons with the nucleus. It is in essence a simple and convenience method for the approximate calculation of Feynman diagrams for the collision of fast charged particles.

The cross section for inelastic electron scattering off proton is expressed in terms of the cross section σ_{ep_EPA} for the absorption of real photons with energy ω :

$$d\sigma_{ep_EPA} = \sigma_r(\omega) \cdot dn(\omega). \quad (2-9)$$

where $\sigma_r(\omega)$ is the photo-production cross section from Hall D generator. The quantity $dn(\omega)$ in this equation is called the equivalent photon number or spectrum, and defined as:

$$dn(\omega) = \int_{q_{min}^2}^{q_{max}^2} dn(\omega, q^2) = N_{EPA}(\omega) \frac{d\omega}{\omega} \quad (2-10)$$

$$N_{EPA}(\omega) = \frac{\alpha}{\pi} \left[\left(1 - \frac{\omega}{E} + \frac{\omega^2}{2E^2}\right) \ln \frac{q_{max}^2}{q_{min}^2} - \left(1 - \frac{\omega}{2E}\right)^2 \ln \frac{\omega^2 + q_{max}^2}{\omega^2 + q_{min}^2} - \frac{m_\pi^2 \omega^2}{E^2 q_{min}^2} \left(1 - \frac{q_{max}^2}{q_{min}^2}\right) \right] \quad (2-11)$$

The total hadron production cross section in electro-production can be approximated to be the sum of bremsstrahlung photon contribution(eq. 2-7) and EPA approximated(eq. 2-9):

$$d\sigma_{ep} = d\sigma_{ep_EPA} + d\sigma_{ep_BREM} = \sigma_r(\omega)(N_{BREM}(\omega) + N_{EPA}(\omega)) \frac{d\omega}{\omega}. \quad (2-12)$$

With this implementation, the electro-production MC generator will now sample its photon energy based on the total hadron production cross section weighted photon distribution. Fig.2-7 shows the differential cross section of π^0 from modified Hall D generator.

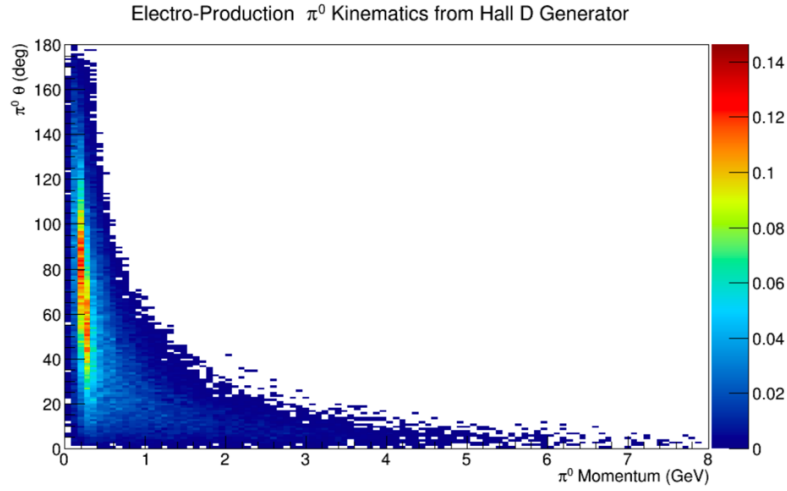


Figure 2-7: The π^0 cross section distribution for 11 GeV electron beam hit 40 cm proton target, acquired from modified Hall D generator.

2.2.3.3 Apply for the target with neutron

With these model assumptions, however, the modified Hall D generator only works for the proton target. To apply for the target with neutrons, isospin symmetry is assumed. Based on proton target cross section, the cross section of nucleus(A) is:

$$\sigma(A)_{\pi^0} = Z \cdot \sigma_{\pi^0} + N \cdot \sigma_{\pi^0} \quad (2-13)$$

$$\sigma(A)_{\pi^-} = Z \cdot \sigma_{\pi^-} + N \cdot \sigma_{\pi^+} \quad (2-14)$$

$$\sigma(A)_{\pi^+} = Z \cdot \sigma_{\pi^+} + N \cdot \sigma_{\pi^-} \quad (2-15)$$

where A, Z and N are the number of nucleons, protons and neutrons in target separately.

With all these model assumptions, the Hall D generator is modified from photo-production generator to a electro-production used for SoLID hadron production purpose.

2.2.4 Comparison

The cross section result of hadron are compared with three generators: modified Wiser, modified Hall D generator and also a Geant4 simulation. The Geant4 method regards the target as a sensitive detector and simulates the incident high energy electrons into detector with recording the generated particles. This process is based on Quark Gluon String model and Bertini cascade model(QGSP_BERT) built in Geant4[43] simulation software.

The comparison use 11 GeV electron beam incident to a 40 cm proton and deuterium targets separately, which is the same experiment setting in SoLID experiment. Table 2-1 and 2-2 show the total cross section of π^0 , π^- and π^+ for different generator.

Pion type	Total xs for proton target(theta<90°)			G4 vs. Hall D agreement
	Wiser xs	Hall D xs	Geant4 xs	
	(mb)	(mb)	(mb)	(%)
π^0	88.5	21.5	26.5	23
π^-	54.6	13.6	13.4	-1.5
π^+	123.7	29.6	29.3	-1

Table 2-1: Hadron cross section comparison for proton target.

Pion type	Total xs for Deuterium target(theta<90°)			G4 vs. Hall D agreement
	Wiser xs	Hall D xs	Geant4 xs	
	(mb)	(mb)	(mb)	(%)
π^0	189.7	43	84.8	97
π^-	191.6	43.2	38.1	-12
π^+	192.7	43.2	37.6	-13

Table 2-2: Hadron cross section comparison for Deuterium target.

The comparison result shows the Wiser generator is overestimated the total pion cross section about 4 times compared to modified Hall D generator. Comparing modified

Hall D generator and Geant4 result, there is a large difference in the π^0 cross section of both proton and deuterium targets, and for π^- and π^+ , proton target match well, deuterium target has a about 10% level difference.

2.3 The motivation of π^0 cross section measurement

As seen from the generator comparison result, there is a difference of hadron cross section between generators, especially for the neutral pion, which is one of the main pion background. We need experiment data to check and correct the generator. However there is no existing data of SoLID experiments' kinematics range, so new data must be taken to perform this comparison and correction.

One purpose of generator in SoLID program is acquiring accurate background estimation, and SoLID experiment will deal with very high trigger rate, which challenge the design of detector and trigger system. The online trigger rate limit of SoLID SIDIS configuration is 100k Hz now, which is restricted by the GEM DAQ, and we need these events are triggered by electrons, however it also could be triggered by photons, which pass through ECal detector behaving like electrons.

The π^0 is a main source of high energy photon, and the most background trigger rate contribution from π^0 . π^0 will decay to two photons, and photon usually come from the following ways:

$$\pi^0 \rightarrow \gamma + \gamma \quad (2-16)$$

$$e + P \rightarrow e' + P' + \gamma \quad (2-17)$$

$$e + N \rightarrow e' + N' + \gamma \quad (2-18)$$

The understanding of π^0 cross section will get a better estimation of the photon background, which highly effect the online trigger rate.

The other motivation is that photon could be regarded as an electron in the final physics analysis. We are trying to use other detectors to reject photon from electron in most case, however some accidental photon signal can't be distinguished considering the high background, which increases the possibility that a photon decay from pion is mis-identified as an electron. Although the mis-identification is inevitable, we can use an accurate generator to evaluate its influence and try to suppress its influence.

We are searching for any possible existing data to perform the comparison, but there is no electro-production data for the electron energy between 6 and 11 GeV, which means π^0 inclusive cross section in this kinematic range has never been measured before. The next section will introduce the DVCS experiment (E12-06-114), the data of which is used to extract the inclusive π^0 s.

2.4 DVCS experiment in JLab

The JLab DVCS (Deeply Virtual Compton Scattering) experiment E12-06-114[44] is one of initial experiments after JLab 12 GeV upgrade in Hall A. It's the first high luminosity ep scattering experiment of electron energy between 6-11 GeV in the world. The experiment is equipped with an additional calorimeter, which could be used to detect the decayed photon from neutral pion, so this experiment provides an excellent chance to find and reconstruct the π^0 events. This thesis will focus on the extraction of inclusive π^0 cross section from the DVCS data. More detailed information of test setup of DVCS experiment will be shown in Chapter 3.

2.4.1 DVCS process introduction

The Deeply Virtual Compton Scattering (DVCS) process[45] is a clean way to measure GPDs (Generalized Parton Distributions), as introduced in section 1.2, GPDs build a 3D tomography of the parton model to introduce functions which parametrize the nucleon structure by presenting the correlation between position and momentum of quarks and gluons. As shown in Fig.2-8, DVCS is a process where a lepton scatters off a quark via the exchange of a virtual photon. The quark absorbs the virtual photon and then emits a real photon.

2.4.2 The DVCS experiment

The DVCS experiment is the third generation DVCS experiment in Hall A of JLab. This experiment received high scientific rating by JLab Program Advisory Committee (PAC). Total 50 PAC days are approved initially, and extent to 130 days because of the low efficiency beam, which runs during 2016 run period. The experiment apply longitudinally

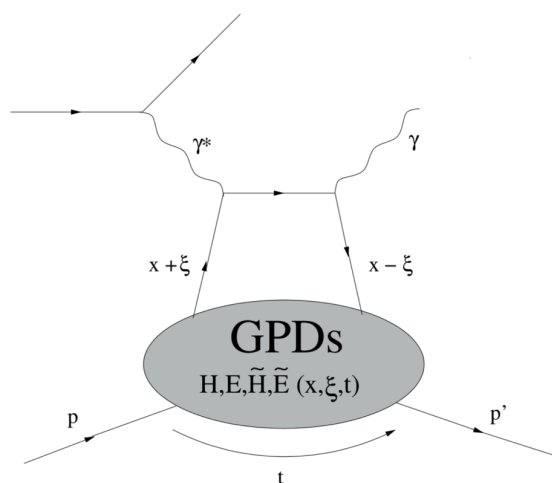


Figure 2-8: The handbag diagram for Deeply Virtual Compton Scattering (DVCS).

polarized electron beam of energy 6.6, 8.8 and 11 GeV to hit a 15 cm liquid hydrogen target, considering a normal $15 \mu A$ current, the luminosity is about 6×10^{37} . There are several configurations covering a wider Q^2 from 3 to $9 GeV^2$, and also performed at different x_B , i.e, 0.36, 0.48 and 0.6[46].

The DVCS process in this experiment is

$$e + p \rightarrow e' + p' + \gamma \quad (2-19)$$

where, e' is scattered electron, p' is recoiled proton, and γ is the real photon that emitted from excited proton.

This experiment utilize the polarized electron beam hitting the 15cm Liquid Hydrogen(LH_2) target, producing a scattered electron and recoiled proton, and also an emitted photon from DVCS process. In this experiment, only scattered electron and photon are detected, the recoiled proton is not detected and could be reconstructed from missing mass. As shown in Fig. 2-9, electron is detected in LHRS, and photon is detected in DVCS electromagnetic calorimeter.

The Table 2-3 shows the list of experiment E12-06-114 configurations, in which we focus on the electromagnetic calorimeter that for photon detection, and the LHRS setting is not shown. The detailed experiment setup will be introduced in next chapter.

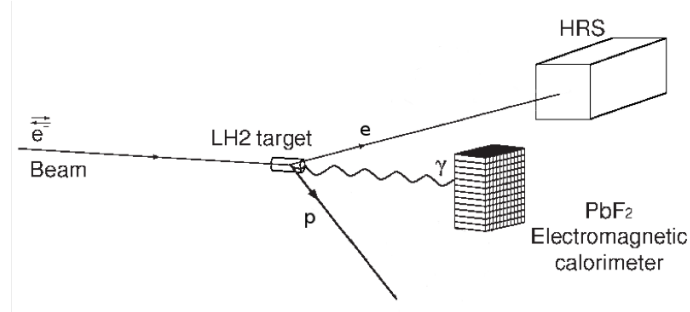


Figure 2-9: A simple schematic shows the setup of DVCS experiment, electron detected in left HRS, and photons are detected in Electromagnetic Calorimeter that placed at the other side of beam line.

DVCS kinematic setting	E_{beam} (GeV)	x_{Bj}	Calorimeter angle (degree)	Calorimeter distance (m)
kin48_1	4.487	0.48	15.198	1.50
kin48_2	8.851	0.48	15.184	2.00
kin48_3	8.847	0.48	11.728	2.50
kin48_4	10.992	0.48	10.069	2.50
kin60_1	8.521	0.60	15.892	1.50
kin60_2	8.521	0.60	14.050	2.00
kin60_3	10.591	0.60	11.014	2.50
kin60_4	10.591	0.60	9.633	3.00

Table 2-3: The main parameters of experiment E12-06-114 configurations. The energy is expected energy, and the actual energy is slightly different. The Calorimeter distance is the distance from calorimeter to the target center.

Chapter 3

The experimental setup

The Thomas Jefferson National Accelerator Facility (Jefferson Lab or JLab) is owned by the U.S. Department of Energy (DOE), located in Newport News, Virginia, USA, to investigate and understand the detailed structure and behavior of the nucleus of the atom. Since the foundation in 1984, more than 1,000 scientists from worldwide participate in performing the physics program, design and build the experimental equipment. The main accelerator equipment is called Continuous Electron Beam Accelerator Facility (CEBAF), offering a longitudinally polarized electron beam, to conduct the target hitting experiment in different Halls. With the maximum beam upgraded from 6 GeV to 12 GeV[47], a new Hall(D) was builded, and the pre-existing Hall A, B and C are also upgraded partly to satisfy the 12 GeV experiment.

The inclusive π^0 cross section analysis work is based on the data of DVCS experiment, which is the first 12 GeV experiment in Hall A. This chapter will introduce basic apparatus of CEBAF and Hall A, and also the additional detector and special DAQ configuration in DVCS experiment setup.

3.1 The Continuous Electron Beam Accelerator Facility (CEBAF)

The CEBAF accelerator has a max five-pass¹ recirculating superconducting radio-frequency linear accelerator, owning four independent Halls with different detector apparatus, could supply at most 12 GeV polarized electron beam, which is upgraded from 6 GeV recently. This upgrade will open a new era for high energy nuclear physics.

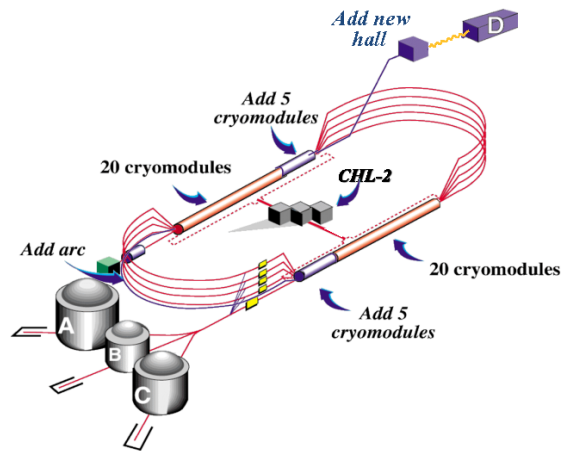


Figure 3-1: Layout of CEBAF upgrade to 12 GeV. Refrigerating system is located at the center of the circle, a second cryogenic plant is added in 12 GeV upgrade to supply additional power. Hall A, B and C are located at south, and the new built Hall D is located at north of CEBAF.

The electron beam generated from a GaAs photoemission electron gun, which is called as injector[48]. The injector play an important role in beam quality control, such as beam current, bunch structure and beam polarization. The injector can provide either a polarized or an unpolarized beam, and beam polarization to Hall A could reach about 80%. The injector operates with continuous wave(CW), offer up to $200\mu\text{A}$ current. The initial accelerator frequency is 1497 MHz, the radio-frequency (RF) separator cavity make the beam be delivered to four Halls simultaneously. 250 MHz or 500 MHz frequency

¹One pass means the electron beam runs one circle in accelerator.

beam could be sent to Hall A, the beam structure and the bunch length is shown in Fig.3-2.

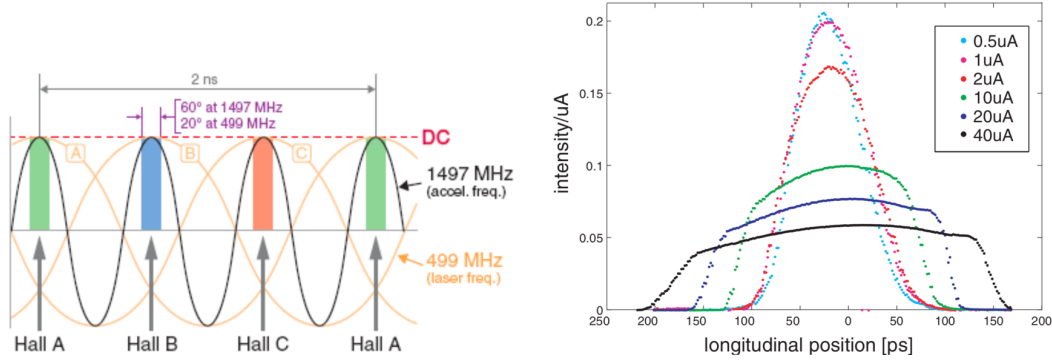


Figure 3-2: Left: the continuous beam structure. The Hall A time interval of two bunches shown here is 2 ns. Right: measured bunch length for different beam current[49].

The linac adopted superconducting radio-frequency (SRF) technology, which uses 2K liquid helium to cool cavity, achieved a higher energy than CEBAF's initial proposal, and also reserve spare room for future upgrade. As shown in Fig.3-1, the electron is accelerated by two linacs, each linac includes 25 cryo-modules of a pass, including 5 new added cryo-modules[50] which are more powerful than old ones. Accelerated energy is increased from 1.2 GeV to 2.2 GeV for each pass after this upgrade. After accelerated by each linac, re-circulation arcs bend the electrons to linac to accelerate again. Since the beam energy of each pass is different, each pass need unique arc to accommodate the beam momentum it transports, and total 10 arcs used in CEBAF. Accelerated by different passes, electron beam could be sent to Hall A, B and C with energy: 2.2, 4.4, 6.6, 8.8 and 11 GeV. The new Hall D only receives 5.5 pass beam, which has the maximum energy 12 GeV.

3.2 Hall A general instrument

The general layout of Hall A[51] shows in Fig.3-3, which is the largest Hall in CEBAF. The electron beam sent to Hall A must be measured and monitored before hitting the target, and these measurements make sure the quality of beam. The target system is located at the center of Hall A, inside of a vacuum scattering chamber.

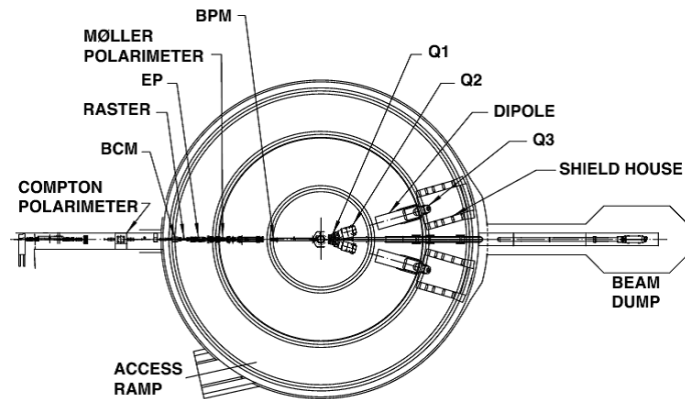


Figure 3-3: Top schematic view of Hall A. Target system is located at the center of Hall A. The equipments at left side(upstream) of target are the beam line monitor system, at the right side(downstream) of target, two HRSs(High Resolution Spectrometer) are equipped at each side of beam line. The un-scattered electrons will be deposited all their energy at beam dump.

3.2.1 The beam line

The beam line instruments monitor the beam quality, pay extra attention to the beam energy, current, polarization, position and transverse size. For each property measurement, at least two different independent methods are applied to improve the accuracy. Most of measurements are non-invasive, and are performed all the time during the run.

3.2.1.1 The Beam Current Monitor(BCM)

The beam current monitor is used to monitor the beam current continuously, and accumulated induction signal to get the charge of each run. The accuracy of charge measurement influences the cross section calculation directly, so the measurement error must be restricted. The BCM consists of two RF cavities and an Unser monitor, located 25 meters upstream of the target, and has a separate DAQ system besides the HRS DAQ. The cavities and the Unser are placed in a temperature-stabilized box to avoid magnetic affect and keep the measurement stable.

As shown in Fig.3-4, two RF (Radio Frequency) cavities are placed upstream and downstream of Unser monitor, they output a voltage level which is proportional to the beam current. The output signal of RF is split to two parts: sampled and integrated. For

the sampled data, it is sent a high-precision digital AC voltmeter, provide the RMS of the charge per second. The integrated data is sent to RMS-to-DC converter, then converted to the frequency by a Voltage-To-Frequency (VTOF) converter. The frequency is read out by 200 MHz scaler, accumulated and recorded as the total beam charge. The charge is recorded in DVCS experiment is about 10s. Since the BCM works from $5 \mu\text{A}$ to $200 \mu\text{A}$, two additional amplifiers with gain factor $\times 3$ and $\times 10$ are added to extend the non-linear region in lower currents with the expense of saturation at high current, which make the linear measurement over different ranges of beam current. Finally, 6 BCM data(U1 (upstream $\times 1$), U3, U10, D1, D3 and D10) are recorded for charge analysis, and amplifier $\times 3$ and $\times 10$ are used as current readout in the DVCS experiment.

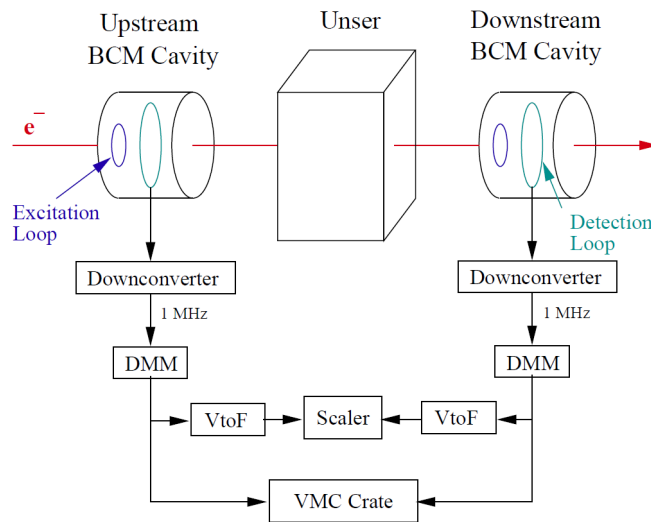


Figure 3-4: The schematic of the BCM system.

The Unser monitor is a Parametric Current Transformer which provides an absolute reference to beam current[52]. The monitor is calibrated with beam known current through a wire inside the beam pipe. And the Unser monitor is sensitive to the fluctuation of environment, extra shielding and temperature-stabilized equipment is needed to reduce noise and zero drift. However, the signal of Unser drift significantly over time, and can't be used to monitor beam current continuously, so it is just used to calibrate the RF cavities.

3.2.1.2 Absolute beam energy measurement

The energy of beam is measured by the Arc method[53], which determines the energy by measuring the deflection of the beam in arc section. At the arc, the beam is bent by 8 dipoles, according to bent angle in magnetic field, the beam momentum $p(\text{GeV})$ could be calculated as:

$$p = k \frac{\int \vec{B} \cdot d\vec{l}}{\theta} \quad (3-1)$$

where $k=0.299792 \text{ GeV rad } T^{-1}m^{-1}/c$, $\int \vec{B} \cdot d\vec{l}$ is the integrated field with trajectory, in Tm unit, measured by a reference magnet(9th dipole), θ is the actual bending angle measured from trajectory, based on a set of wire scanners, and the value is around 34.3° . This method is invasive and could reach a high precision of $\delta E/E = 10^{-4}$. The table 3-1 shows the beam energy test result in 2016 Autumn run period, and also the Experimental Physics and Industrial Control System(EPICS) calculation value from the accelerator setting. Result shows the deviation between measured value and EPICS calculated value is small.

Number of passes	Energy measured in Hall A(GeV)	EPICS calculation value
1	2.222	2.218
3	6.427	6.407
4	8.520	8.497
5	10.587	10.589

Table 3-1: Beam energy measurement result by Arc method and EPICS calculation.

3.2.1.3 Beam position and direction

To measure and monitor the position and direction of the beam at the target location, two Beam Position Monitor(BPMs) are located 7.524 m and 1.286 m separately upstream of target. Each BPM has four open-ended antennas for detecting the beam position and this measurement is non-invasive to the beam. The position is monitored by measuring the induced current at each antennas, and the ratio shows the position. The absolute position of the beam can be determined by wire scanner (superharps) calibration, which is located adjacent to the each BPMs. The thin wire will generate signal when they cross the electron beam, and also provide position calibration of BPMs. This wire scan survey performs at regular interval, especially after a long time beam shut down.

3.2.1.4 Beam polarimetry

The measurement of beam polarimetry make an important role in some experiment using polarized beam, which has a typical beam polarization 75%-85%. DVCS experiment use longitudinal polarized electron beam, and measured by two independent polarimeters: the Compton and the Møller polarimeters.

The inclusive π^0 cross section is not related to the beam polarimetry, and it is not considered in the analysis of this thesis.

3.2.1.5 Raster

Because the experiment runs with high beam current, a point-like beam may boil the liquid target, and result in the density of target less than normal, or even damage the target and target window. To avoid this issue, a raster is added between BCM and EP, to extend the transversal area of beam. The raster is a set of dipoles to spread the beam size to 4×4 mm(full width), which includes two sets of X and Y coils.

3.2.2 The Target System

The target system is placed in a cylindrical scattering vacuum chamber, includes: all kinds of targets mounted in a ladder, vacuum pump-out port, and target condition monitor electronics. The target ladder, as seen in Fig.6-5, is controlled remotely to move the target from one to another. The main target used in DVCS experiment is Liquid Hydrogen (LH_2), which is the Proton target. There are also other kinds of solid targets are used in experiment to test the beam quality and calibration purposes.

The LH_2 cryogenic target is the main target used in DVCS experiment. The size of target cell is 15 cm long and 6.35 cm in diameter, with an Aluminum entrance and exit window 127 μm and 152 μm in thickness. To keep the cryogenic target stable, sub-system like cooling, and temperature and pressure monitoring are mounted inside the scattering chamber. The normal density of LH_2 used in DVCS experiment is 0.0723 g/cm^3 , with the temperature 19 K and pressure 0.17 MPa. To cool the LH_2 target, a heat exchanger with 15 K helium coolant supplied by the End Station Refrigeration which also supply coolant to linac. The maximum cooling power is 1kW, allowing the current of raster beam up to 130 μA . Because the hydrogen is highly flammable and explosive, safety is a major

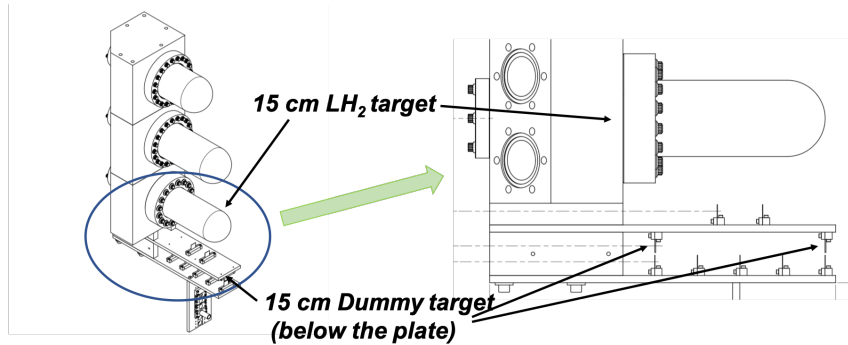


Figure 3-5: Schematic layout of the target ladder[54]. The 15 cm Liquid Hydrogen (LH_2) target and dummy target is emphasized in the picture.

consideration during the experiment, and an extra trained target operator is standby to monitor the condition of target, ready to deal with potential target problems.

Other solid targets in the target ladder includes:

- 15 cm dummy target: only has two upstream and downstream target windows, exactly same position and material as 15 cm cryogenic target, used to evaluate the the effect of target window. In data analysis, the influence of target window need to be subtracted from the total cryogenic target. Dummy target runs are carried out at each DVCS kinematics setting. To make the dummy target runs more efficient, the thickness of dummy target is about 7 times of real target window, which is 889 μm .
- Empty target: nothing in target, used for safety purpose. If there is no beam, target will be moved to this position. Also a good position to place the target while beam is still being sent to the Hall.
- The optic target: include five 1mm thickness carbon foil with fixed z position, which has 3.75 cm interval between each other. It used to perform the optical calibration of spectrometer, which acquire the vertex position along beam direction.
- Carbon hole target: a single carbon foil with 2mm hole in diameter, used to check the central position of beam.
- Carbon target: made of 1 mm single carbon foil.
- BeO target: give out light when hit by electron beam, the light could be visualized directly by a camera mounted near the target, used to check the beam centering.

3.3 The High Resolution spectrometer(HRS)

There are two High Resolution Spectrometers located at each side of beam line, as seen in Fig.3-3, called Left-HRS (LHRS) and right-HRS (RHRS). The LHRS and RHRS are mainly used to detect the electron and proton separately, the only difference is the pion rejector of RHRS has more radiation length to deposit the energy of particle than LHRS. Both HRSs include magnet to select particle with specific charge, angle and momentum, and detector package to measure the particle information. In DVCS experiment, only LHRS is used to detect the scattered electron, RHRS is not in use.

The charged particle will be selected by the super-conducting magnet system firstly, and bend the charged particle 45° upward to produce a better momentum resolution and also reduce the radiation damage on magnet system and detectors. As shown in Fig.3-6, the configuration of magnet is QQD_nQ design[51]: three quadrupoles(Q)are used to converge the particles and a dipole(D) used to bend the trajectory. The spectrometer has a high momentum resolution of 10^{-4} level over 0.8 to 4GeV/c momentum range, with $\pm 4.5\%$ momentum acceptance around the central momentum setting.

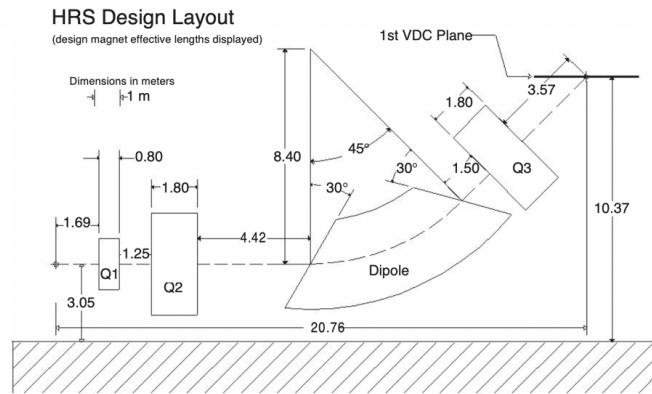


Figure 3-6: Schematic layout of a HRS device magnetic system, showing the geometrical configuration of the three quadrupoles and the dipole magnets.

The detector package of LHRS contains detectors for the function of trigger, tracking and particle identification (PID). As shown in Fig.3-7, along the particle trajectory, particle pass through Vertical Drift Chambers (VDCs), a scintillator paddle(S0), Gas Cherenkov (GS), 16 parallel scintillator paddles (S2m), and the lead-glass shower detector called Pion rejector(PR).

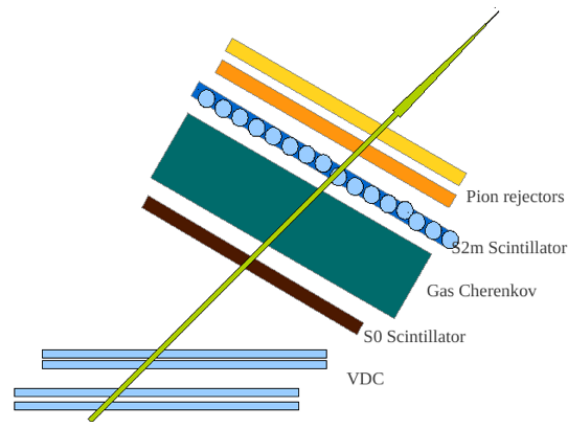


Figure 3-7: Schematic layout of LHRS side view. The arrow show a trajectory direction of charged particle.

The tracking information is provided by a pair of parallel VDCs, which have an angle of 45 degree with respect to the central trajectory. Each VDC has two wire planes with a 90° oriented UV configuration, to form a two-dimension position information. Tracking is acquired by combining of the two VDCs, which achieve a 100 μm position resolution and 0.5 mrad angular resolution. The number of particle pass through the magnet is rare, and most of trigger event only left one tracking information. The main purpose of tracking is, with the help of an optical matrix from magnet, reconstructing vertex² on target, and calculating particle's exact momentum and scattering angle under LHRS acceptance.

S0 and S2m are plastic scintillator paddles, mainly used in event trigger. S0 is a 10mm thick single paddle, read out by PMTs at each end, which is designed for sub-trigger and check the efficiency of other detectors. S2m[?] is used for main trigger and conclusive to time resolution. It consists of sixteen 2 inch thickness paddles, with the size 17×5.5 inch, also read out by a PMT at each end. The typical time resolution of S2m is about 300ps.

A gas Cherenkov detector filled with CO_2 at atmospheric pressure is mounted be-

²The vertex is electron hit position along the beam direction. For long target experiment, vertex is important to reconstruct the electron and secondary particle tracking. The deviation of hit position in transversal direction is ignored.

tween S0 and S2m. Only when the velocity of particle larger than its pre-set threshold, it will radiate Cherenkov light, so the pion that has same momentum however lower velocity is separated from electron. The refractive index of gas is 1.00041, to give the momentum threshold of Cherenkov light emittance for electron and pion is 17MeV/c and 4.8GeV/c separately. The Cherenkov light is collected by 10 large window PMTs, and the sum of these PMTs signal determine the trigger, which is about 15-20 photoelectrons produced by a single electron.

Two layers of lead glass are placed at the end of detector package, which are commonly called electromagnetic calorimeter, and also called pion rejector (PR) for the PID purpose. The total radiation length of PR is 11.8, the electron almost deposit all energy as a shower in PR, and pion only loss a small fraction of energy through ionization, this energy deposit difference also make a separation of pion from electron. The PR has two layers, electron deposit most of its energy at the first layer, and pion deposit similar energy in both layers, which add extra cut for pion rejection besides GC. The combination of gas Cherenkov and Pion Rejector provide a pion suppression with a factor of $2 * 10^5$ for above 2 GeV/c LHRS setting.

Any two combination of S0, GC, S2m and PR detector could decide the trigger, and recorded as a part of trigger in data. To detect the electron clearly and efficiently, the main trigger is chosen as the logic AND of GC and S2m, other triggers are also used to check mutually the detection efficiency of each detector.

3.4 The DVCS Electromagnetic Calorimeter

In the DVCS experiment E12-06-114, it needs to detect the generated photon, which is detected by DVCS electromagnetic calorimeter that placed at other side of beam line related to the LHRS. As shown in Fig.3-8, it is made of 208 lead-fluoride (PbF_2) blocks, arranged as an array of 13×16 [44]. The total radiation length for each block is $20 X_0$, with the size $3 \times 3 \times 18.6 \text{ cm}^3$. Each crystal block is coupled directly to a fast response PMT (Hamamatsu R7700). The Electromagnetic Calorimeter is mounted on a special cart, on which the distance to target and the angle to the beam line is adjustable for different kinematical configuration. The consideration of PbF_2 calorimeter choice is listed as the followings:



Figure 3-8: The front view of DVCS calorimeter. The PbF_2 blocks are revealed with removed front plate.

- PbF_2 calorimeter is a homogeneous Cherenkov calorimeter, and has the fastest response of all the available radiation resistance material[55]. It only produces instantly Cherenkov light, and there is no after-glow light. One challenge of calorimeter design in this experiment is to deal with high background pileup. Since there is a velocity threshold for Cherenkov light, the calorimeter is insensitive to low energy particles, including hadrons and low energy photons. It generates a clear and uniform pulse signal, and allows us to use the 1GHz Analog Ring Sampler (ARS) digitizer to minimize pileup.
- It has a large density (7.7 g/cm^3), and short radiation length (0.93 cm), which make the detector very compact in longitudinal direction, and minimize the light collection fluctuations.
- The small *Moliere* radius (2.2 cm) makes the photon/electron deposit most of its energy in central block, and a shower signal is restricted in 9 adjacent blocks. This small radius allows us to separate two close photons that decayed from a π^0 ,

and also minimize shower leakage at the boundary. The $3\text{cm} \times 3\text{cm}$ block size is optimized by position resolution and π^0 reconstruction.

- PbF_2 has better radiation resistance than other lead glass, and the radiation damage can be cured by blue light.

However, since the PbF_2 calorimeter produce Cherenkov light, the light yield is only $1 \sim 2$ photo-electron detected per MeV, which lead to a bad energy resolution. And the price of PbF_2 is very high, so it can't be used for large area detector.

The DVCS electromagnetic calorimeter is the only detector that used for π^0 detection, and π^0 events will be reconstructed by it. More attention will be paid to its property and calibration in Chapter 5.

3.5 The Data Acquisition (DAQ) System

The DAQ system includes the Hall A general DAQ mostly focus on LHRS and DAQ designed specifically for DVCS calorimeter, and they work together to form the final events trigger.

3.5.1 General Hall A Data Acquisition System

The general Hall A DAQ is controlled by a software called CODA (CEBAF On-line Data Acquisition), all the data of detectors including the DVCS electromagnetic calorimeter are controlled and monitored by it. It records the HRS detector signal read out by Time-to-Digital Converters (TDCs), Analog Digital Converters (ADCs) and scalers, which is mounted in VME crates, and also collects run status data from other Hall A apparatus, such as the status of beam line that introduced in section 3.2.1 and target.

When CODA software is running, the trigger supervisor (TS) will determine if the signal in detector satisfy the trigger setting. Once the system is triggered, the Read-Out Controller (ROC) will gather the detectors' data from the VME crate, and each VME crate has an individual ROC. An Event Builder (EB) collects data from all ROCs, and data is stored in disk by the Event Recorder (ER). The electronic is controlled by RunControl, by which users can select different experimental configurations, start and stop runs, as well as reset and monitor CODA components.

The CODA software will control both the electron detection in LHRS and photon detection in DVCS calorimeter.

3.5.2 DVCS calorimeter DAQ system

These is an additional DAQ system especially used for DVCS electromagnetic calorimeter, each calorimeter block is read out by a ADC and an Analog Ring Sampler (ARS) chip. Due to the high luminosity ($10^{37} s^{-1} cm^{-2}$) of this experiment and calorimeter is placed close to the target, it leads to a high rate on calorimeter and causes pile-up photon events problem. The conventional ADCs integrate all the charge within a fixed time window, which contain all pile-up events and no time information. Even so, the ADC has its advantage of fast readout, and will be used as calorimeter trigger supervisor. The ARS consist of an array of 128 capacitor with a continuous sample rate 1 GHz, to record a full 128 ns waveform. As seen in the left plot of Fig.3-9, the ARS works with continuously overwriting sampling PMT signal to the 128 capacitors, once a stop signal is issued, freezing the overwriting process, and the PMT signal in capacitor is stored and waiting for readout. As seen in right plot of Fig.3-9, the ARS data contain entire waveform, used to analyze elaborately offline to suppress the pile-up events, and could achieve a good time and energy resolution.

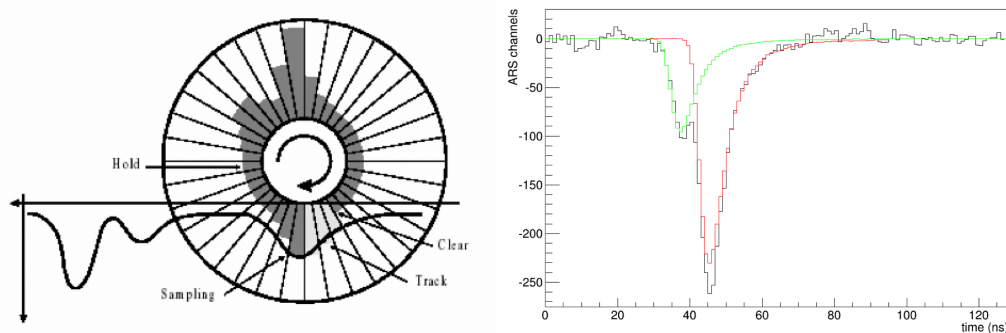


Figure 3-9: Left: digitization of the charge stored in ARS capacitors. Right: A example of ARS waveform and pile-up events. The waveform is fitted by a two-pulse fitting.

The ARS creates a large amount of data ($208 \text{ blocks} \times 128 \text{ samples} \times 11 \text{ bits per event}$) compared to all other detectors in LHRS. For a typical 200 Hz data taking rate,

the data taking for calorimeter is about 8Mbyte/s. The readout time contribute to the total dead time.

3.5.3 The trigger system

The main DVCS trigger need both electron and photon detections, the coincidence need a two-level trigger. The electron is detected in LHRS, and the photon is detected in DVCS calorimeter. Because the electrons are precisely detected and cleanly recognized in LHRS than photons in calorimeter, the trigger system will search the electron signal firstly, then search for the coincidence photon signal in DVCS calorimeter.

3.5.3.1 Trigger in LHRS

The coincidence of S2m and Cherenkov detector in LHRS generate the first level trigger. The Cherenkov detector in trigger is used to reject most pions, so its threshold must be high enough to reject pions and keep most electrons. Any charged particle pass through the S2m detector will generate scintillation signal, which not offer PID information, but it could offer good time information, and decide the trigger time. Once there is a coincidence between S2m and Cherenkov detector signal within a short time, the LHRS is triggered.

The LHRS also could be triggered by other trigger pattern, such as the coincidence of S0 and GC, the data of which is taken for the measurement of S2m detection efficiency. When the LHRS is triggered, a STOP command will be sent to the DVCS calorimeter DAQ.

3.5.3.2 Trigger in DVCS calorimeter

The first step of DVCS trigger decision will check if there is signal in calorimeter. Since a photon will deposit most of its energy in the central block and only a small part is deposited in the blocks adjacent it, to make the photon searching in calorimeter efficiently, DAQ will calculate the sum of ADC value for every 2×2 neighboring blocks combinations in 100 ns time window, and check if the sum above the threshold. This decision process takes about 340 ns, once one combination satisfies the trigger threshold, a VALID signal will be send to final trigger supervisor, and record this event with all the information in detectors including LHRS.

If there is no photon signal found in this method, a fast clear signal is generated to restore the status of all detectors and ready for next event, which lead to a 500 ns dead time. Otherwise, the data(waveform) in ARSs will be read out and recorded to disk. The digitization process of ARS signal is slow(128 μ s), which contributes main impact on the dead time of whole DAQ system.

3.5.3.3 Pre-scale in multiple trigger mode

The trigger supervisor could deal with multiple trigger modes simultaneously and record data in sequence with pre-scaled factor. It allows us to acquire other different trigger events that we interest besides the main trigger, such as the DIS(deep inclusive scattering) events, which only triggered by S2m and Cherenkov in LHRS and ignore whether photon is detected or not. Each mode will record the signal of all detectors, not just the detector triggered, even if no signal in it. The DIS event is also important in nuclear study and virtual to the inclusive π^0 cross section extraction. Each trigger mode is recorded with a different trigger pattern tag to distinguish. The trigger events could be selected by tag to perform different analysis purpose.

Since there is no need to record all the events of other trigger (except main trigger), which has much more event rate than main trigger, a pre-scale setting is applied. Trigger pre-scale is configured in trigger dominate board to record secondary triggers and suppress the event rate of these triggers. For each trigger mode, it has a fixed pre-scale value N, which means only one event is recorded when total N events of this mode are triggered (detected). The trigger decision process will not lead to the deadtime, and the deadtime is only existed in the signal digitization, data recording and also photon cluster searching in DVCS calorimeter. The pre-scale setting could highly decrease event rate and deadtime.

Each DVCS experiment kinematics have different pre-scale factors, based on the event trigger rate and background. The table 3-2 shows a typical trigger setting including all trigger mode with its pre-scale factor. The trigger S0 & GC and S0 & S2m are kept in trigger to monitor the detection efficiency of detector. These is also a special trigger generated by 104k Hz clock, which is totally random trigger event, used for checking if the detector works normally with time. Cosmic ray also could trigger the system, and is rejected by the two scintillator paddles placed above the spectrometer package.

Event trigger	Pre-scale value
S2m and GC and Calorimeter	1
S2m and GC	2
S0 and GC	128
S0 and S2m	128
Clock	16384
Cosmic ray	0

Table 3-2: All the trigger pattern in trigger domination plug-in for a typical run with pre-scale value. The Pre-scale value means only one event is recorded when total N events are detected.

Chapter 4

The strategy for extracting inclusive π^0 cross section from DVCS experiment data

The π^0 events could be detected in DVCS calorimeter, which is reconstructed by the detection of two photons. For the inclusive π^0 cross section measurement, it only related the searching of π^0 events, and must exclude the influence of the trigger electrons.

However, the main trigger of DVCS experiment is the coincidence of electron and photon, and this analysis must use other trigger data that photon is not necessary in trigger. Even so, the inclusive π^0 events still could be recognized and extracted from this data with some tricks, which is emphasized in Sect.4.3.

This chapter will describe how to extract inclusive π^0 cross section from the DVCS experiment data, the event selection on raw triggered events, and also the difficulty in the analysis with using the data.

4.1 Basic principle to extract inclusive π^0 cross section

To extract the inclusive π^0 cross section, we only need to care about the channel of $ep \rightarrow \pi^0 + X$, in which only π^0 is detected.

For ep fixed target scattering experiment, there are four main parameters related to

the cross section: the beam energy, the target length, the energy of π^0 and the scattered theta angle. The other parameters should not affect the value of the cross section, and will be uniformed in cross section calculation.

Because the experiment has fixed beam energy and target length, the differential cross section for π^0 with specific energy E and angle θ is expressed as the formula:

$$d\sigma(E, \theta) = \frac{N^{\pi^0}}{d\phi \times \mathcal{L} \times \eta_{exp}} = \frac{N_{detected}^{\pi^0}}{A_{cep}(E, \theta, \phi) \times d\phi \times \mathcal{L} \times \eta_{exp}} \quad (4-1)$$

where

- N^{π^0} and $N_{detected}^{\pi^0}$ is the number of π^0 generated and detected separately in the specific theta and energy range.
- \mathcal{L} is the integrated luminosity, the calculation of which will be described in the following.
- ϕ is the angle around beam, and $d\phi$ is a cut restricted by the detector geometry. Since the system around the beam is symmetrical, this cut will not influence the cross section value.
- η_{exp} is the detector detection efficiency.
- $A_{cep}(E, \theta)$ is the detector acceptance ratio for specific E, θ and ϕ , which is acquired from simulation.

And the luminosity \mathcal{L} is given by

$$\mathcal{L} = \int \frac{d\mathcal{L}}{dt} dt = N_{beam} \times N_{target} = \frac{Q}{e} \times \frac{N_A \rho l}{A_H} \quad (4-2)$$

Where constant $e = 1.6 \cdot 10^{-19}$ is the charge of single electron, $A_H = 1.0079g/mol$ is the atomic mass of H. For the fixed LH_2 target, the length is 15cm, and with the operation temperature of 19 Kelvin and pressure of 25 psi (0.17 Mpa), the density ρ would be $(0.07229)g/cm^3$. The Charge Q is the integrated charge of all the time that the events satisfy the cut.

Most π^0 s are generated at the vertex of electron interact with proton in target. 98.8%(PDG) of π^0 will decay to two photons instantly, and also possible decay to $e^+e^-\gamma$ with a rare ratio. The living time of π^0 is about $(8.4 \pm 0.5) \times 10^{-17}s$, for a 5GeV π^0 , the average flying length before decay is about $cr=100nm$, which could be ignored compared to the target size, so we regard the vertex of two photons that decay from π^0 have the same vertex as electron interact with proton, which is along the electron beam line.

To get the π^0 cross section, the main work is to get the number of π^0 events in Eq.4-1

with enough statistics, which are reconstructed by two photon signal.

4.2 The data analysis of DVCS experiment

As introduced in section 2.4.2, the electro-production of DVCS process in E12-06-114 experiment is

$$e + p \rightarrow e' + p' + \gamma \quad (4-3)$$

For the detection of DVCS exclusive process, all three particles in final state must be detected. In this experiment, only two particles electron and photon are detected, and this process is recognized by the missing mass analysis of the $ep \rightarrow e\gamma X$.

4.2.1 Exclusivity of the DVCS process by missing mass method

The squared missing mass M_X^2 could be described as:

$$M_X^2(ep \rightarrow e\gamma X) = (k + p - k' - q')^2 \quad (4-4)$$

In the equation, k is the 4-vectors of incident electron, of which the energy is equal to the beam energy, k' is the 4-vectors of scattered electron, p is the still proton in target, q' is the emitted photon.

For previous initial experiment setup, an additional detector that proton array (PA) is designed to detect recoil protons, however the constraints on the PA geometry was greatly affecting the proton acceptance. Since the detection resolution of electrons and photons are both good, it is well enough to use missing mass cut to select exclusive DVCS events. Previous 6 GeV experiment with PA detector shows good consistent result of triple coincidence events compared to missing mass method. Fig.4-1 shows the squared missing mass associated with the reaction $ep \rightarrow e\gamma X$ from 6 GeV data. This is made possible by the excellent momentum resolution of the Hall A HRS and the fair energy and position resolutions of our dedicated electromagnetic calorimeter. And the coincidence of only electron and photon make the trigger and data analysis more efficient.

One of other dominate process would be $e+p \rightarrow e + p + \pi^0$, as seen from Fig.4-1, which is also important in the DVCS cross section extraction to subtract the π^0 contamination. To minimum the influence from this process, the cut in missing mass will be less than $M_X^2 < (M_p + M_{\pi^0})^2 \approx 1.15 \text{ GeV}^2$.

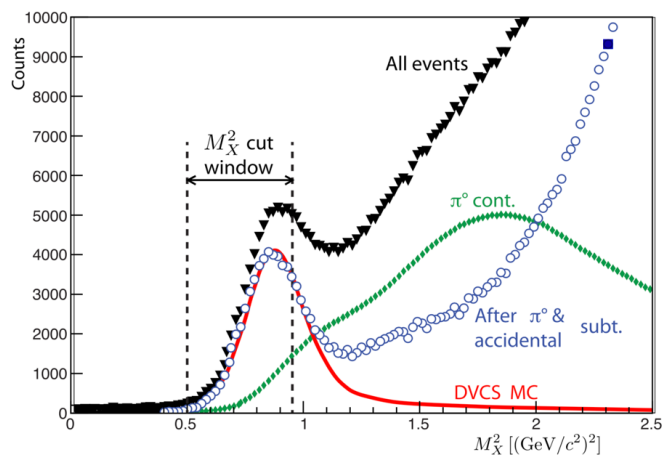


Figure 4-1: Squared missing mass associated with the reaction $ep \rightarrow e\gamma X$ for DVCS 2004-Kin2[56]. The black triangles represent the total events. The green diamonds are the π^0 contamination, and the blue open circles are the total events after p_i^0 and accidental events subtraction. The red solid line is the result from simulation, and match well with events after subtraction in M_X^2 cut window.

4.2.2 DVCS event selection

The purpose of good DVCS events selection, is to select both good electrons and photons. The electrons cut entail good tracking, timing and PID, and photon side entail a single photon signal with high energy, which lead to a very strict cut for DVCS events. And the analysis will use all possible data which related to the the total charge during the run period, except some runs with bad current.

A good DVCS event must satisfy the following cut (electron cut):

- Has a good single track.
- Pass the offline PR electron and GC electron cuts in LHRS.
- A Good vertex is reconstructed in target.
- Phase space and acceptance cut of spectrometer (magnet).

These are basic cuts for electron selection, however, for the inclusive π^0 searching, these cuts seems not necessary and will add a bias to the analysis. So we must take care about these cuts to select good events, more discussion will be described in section 4.5.

4.3 The inclusive π^0 events in DVCS experiment data

The trigger of DVCS experiment is the combination of electron and photon coincidence, and for inclusive π^0 events, what we need is only opening a random time window to search for the π^0 events appearing in it. It seems that the DVCS data is not able to extract inclusive π^0 events.

Luckily, the design of experiment reserves other background data that used for background subtraction, which make the inclusive π^0 analysis possible. The inclusive π^0 could be extracted from DVCS experiment data rely on **three necessary factors: DIS trigger, the long ARS time window and continuous beam structure.**

As introduced in section 3.5.3.2, the trigger mode include both main trigger and also the DIS trigger. For the main trigger, a photon that energy above threshold must be found in 100 ns time window, even if the photon may not coincident with the triggered electron, and this photon will lead to a bias for π^0 analysis. The DIS trigger means that once an electron is found in LHRS, the data will be recorded, no matter if a photon signal found in calorimeter.

Since all the events are triggered by electron, and we are extracting the cross section of $ep \rightarrow \pi^0 + X$, not $ep \rightarrow e' + \pi^0 + X$, the bias from electron trigger must avoid. Luckily, the DVCS calorimeter ARS has a long time window (128 ns) to record the full shape of waveform, which is not only contains the signal coincident with electron but also the so-called background that non-coincidence with electron. As shown in Fig.4-2, there is a signal peak appear in time window that coincident with electron trigger, and the coincident photon in DVCS process will appear at that time. Besides, **if the arriving time of photon is not in that range, that means the photon is not coincident with the electron, and it just comes from other beam bunch that not related to the triggered electron.** There are total nearly 32 beam bunches exist in 128 ns time window (4 ns each). For the non-coincidence time window, photon will appear real randomly. It just like open a random time window to see if photon exist in it, and this non-coincident time window will be used in π^0 events searching.

The electron beam has a continuous beam structure, which means the same beam bunch comes to the target every 4 ns, so all beam bunch appear in time window have same current. As shown in Fig.4-2, each peak represents a bunch. Thanks to the good time

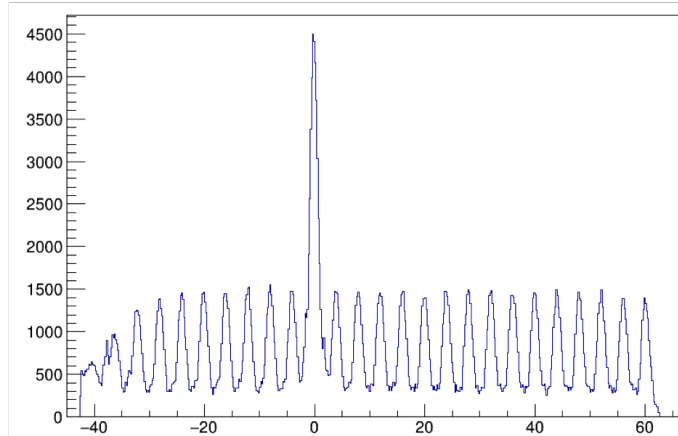


Figure 4-2: The photon distribution acquired from ARS, which shows the beam bunch structure(unit in x axis is ns). The high peak coincident signal with electron trigger is regarded as the time 0.

resolution of both LHRS and DVCS calorimeter, we could clearly separate the adjacent two bunches. So the two photon signal from π^0 could be found in each individual bunch.

4.4 Restriction and problems in using DVCS data

The DVCS experiment E12-06-114 is not a ideal experiment to perform the π^0 analysis, however it's the only and best chance to extract the first inclusive π^0 data after JLab 12 GeV upgrade. This section will show these restrictions, and the erro of which will be considered in systematic errors.

4.4.1 Low energy photon

For DVCS detection, they care about the single photon that energy above 2 GeV, and the detector is only calibrated by the high energy electron. Lack of the low energy calibration, there will be energy bias for low energy photon, because the signal response to energy may not linear. Other problem is low energy photons are not accurate as high energy ones to be reconstructed from the waveform, and because of the high background, there will be many more low energy photons occur.

4.4.2 Vertex of π^0

Since the inclusive π^0 is not related to the coincidence electron, we don't know the vertex of π^0 , and the π^0 could be generated from any vertex in target. Without vertex information, a vertex uncertainty error will be added to the final error, and especially influence the events detected in the edge of calorimeter.

4.4.3 Calorimeter geometry acceptance of π^0

To reconstruct the π^0 events, both two decayed photons are needed to be detected. The geometry restriction of detector only accept a narrow area of theta angle and π^0 energy, and a view of π^0 energy acceptance is shown in Fig.4-3. For low energy π^0 , the minimum angle between two decayed photons with photon energy cut on calorimeter is larger than high energy one. And if the minimum angle is larger than the detector acceptance, the π^0 with this low energy will never be detected.

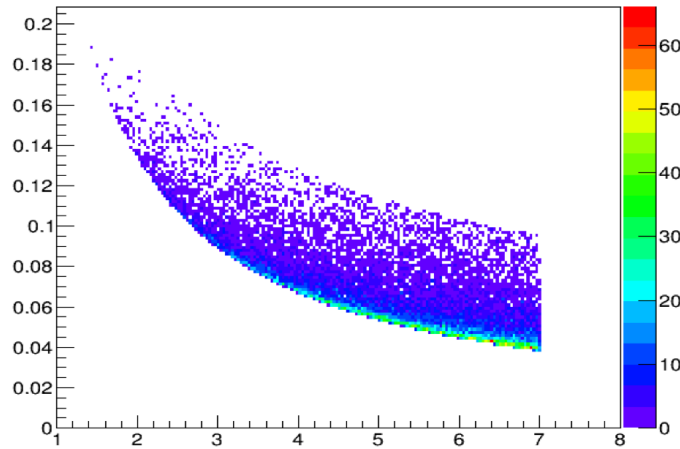


Figure 4-3: The calorimeter π^0 acceptance as a 2D function of π^0 energy and the angle between two decayed photons for kin48_3 configuration. The X axis is π^0 energy in GeV, and Y axis is the angle between two decayed photons in rad.

However for the purpose of background estimation, we focus more on the low energy background because the low energy π^0 is much more. And in the analysis, the low energy events contribute a high background, and for low energy π^0 events extraction, high background will be a challenge.

The other problem is small angle acceptance of detector, luckily the angle covers the most important coverage as SoLID detector acceptance.

4.4.4 Target window

For inclusive π^0 s, some are generated from target window, which contribute about 7% π^0 events generated in the whole target. Without vertex information, we can't distinguish whether π^0 comes from the the target window or from LH2 target. The most practical way to subtract the π^0 events from target window is using dummy target data. However, there are not enough events of dummy run in this experiment, which cause a large statistics error if using this method. On the other hand, the effect of target window could be evaluated and subtracted by simulation, and will be applied in this analysis.

4.5 Event selection cut for π^0 analysis

The event selection is focus on the electron trigger selection in LHRS, and photon signal is not involved in this section. The cut will make sure the selection of good electron trigger, and avoid any bias on π^0 in selection. After selection, these events will be used for the inclusive π^0 extraction, which just like opening a time window to search π^0 signal.

4.5.1 Trigger

The trigger is recognized by a trigger tag called TriggerPatternWord which is a value returned from Trigger Supervisor once events are triggered. The TriggerPatternWord value of DIS events is equal to 128. To make the data taking efficient, a part of DIS events is abandoned by pre-scale setting, Table 4-1 shows which part of the DIS events are recorded.

The trigger supervisor decides if the DIS trigger events are recorded following two steps. With a pre-scale factor 2, the DIS triggered events are randomly divided to two parts, upper row and lower row in Table 4-1, and the first part (lower row) is recorded directly ignore the searching of photon signal. Then the second part will check if photon signal exist. If photon is found in calorimeter, the event will be recorded, otherwise it will

If Calorimeter triggered		
Yes (DVCS main trigger)	No	
✓	✓	Events used in π^0 analysis
✓		

Table 4-1: The DIS events recorded in data. ✓ means the part recorded. The DIS events are divided to four parts, only three parts are recorded in final data.

be discarded. After these two steps, the DIS events are divided to four parts: three parts are recorded and one part is discarded.

4.5.2 Electron identification

The initial purpose of LHRS trigger is accepting all electrons with the specific momentum and angle, and reject π^- s, which have much more events than electron with same momentum. For the triggered event, most of events are triggered by electron, and also a small part is triggered by pion accidentally. Since we only care about the inclusive π^0 in calorimeter side, either electron or pion trigger should not affect the final cross section result. However, there are some differences between electron and pion trigger, such as different flying time from target to detector in LHRS, and the pion also could lead to a bad time resolution.

Most of pion is rejected by the online trigger, and the electron also could be recognized offline by the signal in both Cherenkov and pion rejector. Either detector has a very high rejection factor to pions.

For normal situation that momentum from 1GeV/c to 4GeV/c, pion itself will be rejected without emitting any Cherenkov light. However, to accept all the electrons, the threshold of Cherenkov in trigger is set very low (15mV), even a signal of single photon could pass this threshold. To suppress pion and noise offline, the threshold for offline electron selection is set to 200 ADC channels. The original gas Cherenkov channel distribution is shown in the left plot of Fig.4-4.

There are also δ rays produced from pion by interacting with matter between target and detector. The δ rays are electrons that take a part of energy from pion, and when its speed above the Cherenkov threshold, the behavior of δ rays is same as high energy electrons in Cherenkov. Then another detector pion rejector is applied to supply additional

rejection for pions and medium energy δ rays. The pion rejector is not included in trigger, because the pion rejection efficiency is not as high as Cherenkov detector. The two layers' design in longitude separation could improve pion rejection, based on the fact that electron deposit most of energy in the first layer, while pion only lost a small part of energy through ionization and no significant energy deposition difference in two layers. The right plot of Fig.4-4 shows the offline ADC cut in Pion Rejector to select electrons.

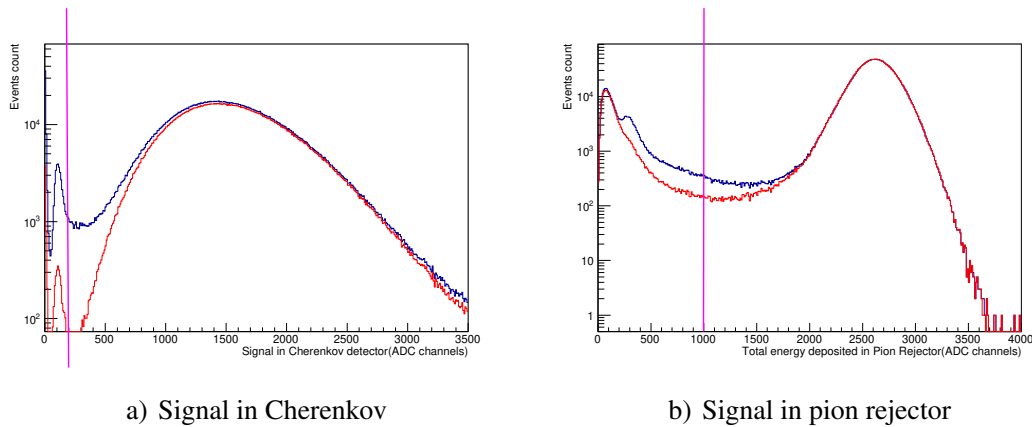


Figure 4-4: Left: the sum of 10 PMTs channel in Cherenkov detector. The small peak is the signal of single photon, may cause from accidental coincidence noise. A 200 ADC channel cut is applied to reject the low signal. Right: total energy deposit distribution in Pion Rejector with the function of ADC channel. A 1000 ADC channel cut is applied. In both plots, the blue lines are original events, and the red lines are the left events after the other detector's cut.

With both the Cherenkov and Pion Rejector detector cut, pure electrons are separated. To check the influence from electron and others particles, we consider this affect of PID through the photon yield normalized to beam charge, result shows in Table 4-2. The electron trigger that pass the offline cut have more photon yield than others particle, and to make sure the good event selection, only the events that satisfy offline electron cut is selected.

4.5.3 Tracking and S2m scintillator

The tracking is determined by the two layers of Vertical Drift Chamber(VDC). Each VDC layer will reconstruct a position information, and then through two points to recon-

Number of events Number of photons($E>0.5$ GeV) / Charge		Cherenkov detector cut	
		>200	<200
Pion rejector cut (preshower + shower)	>1000	2.7M (electron) 0.7348	0.0011M 0.6863
	<1000	0.2M 0.6819	0.022M 0.6818

Table 4-2: The number of photon cluster normalized to charge with PID cut. The value at the top of each block is the number of events pass the cut, the bottom value is the photon number normalized to the charge(in arbitrary unit).

struct the tracking. Since VDC system is not designed to handle multi-tracks, if several particles arrive at same time, many more tracks may be reconstructed. When these tracks are reconstructed, it's hard to recognize which tracking is real, to keep things simple, we abandon all multi-tracking events and only keep single tracking event. The accuracy of tracking will influence the vertex reconstruction and also the time resolution, because it cause the error of flying time from target to detector.

The S2m scintillator, as one of trigger detector, determines the trigger time, and is essential to time resolution. For multi-tracking and other possible events, at least two scintillator paddles have signal in some events. It's hard to determine which one is triggered firstly and if it satisfies the tracking, which lead to a bad time resolution. Time is virtual to beam bunch separation, and to achieve a better time resolution, the π^0 analysis use the events that only one S2m scintillator paddle is triggered.

4.5.4 Vertex

The vertex means the electron hit position in target along the beam direction, it's also the vertex of the coincidence photon. The vertex is reconstructed by the tracking according to a transport matrix of LHRS spectrometer system, the reconstructed vertex distribution is shown in the left plot of Fig.4-5. However for inclusive π^0 that is not coincident with the triggered electron, the vertex information is unknown. The target contains both 15-cm Liquid Hydrogen and two target windows, and for DVCS analysis purpose, the events near and beyond target window must be discarded. But for inclusive π^0 analysis, strict vertex cut is not necessary, and we check the photon cluster number

normalized to the charge at different vertex, shown in the right plot of Fig.4-5. Result shows the events with very bad reconstructed vertex have lower photon yield, so a very loose vertex cut $[-0.1\text{m } 0.1\text{m}]$ is applied, and this cut just discard a small part of events.

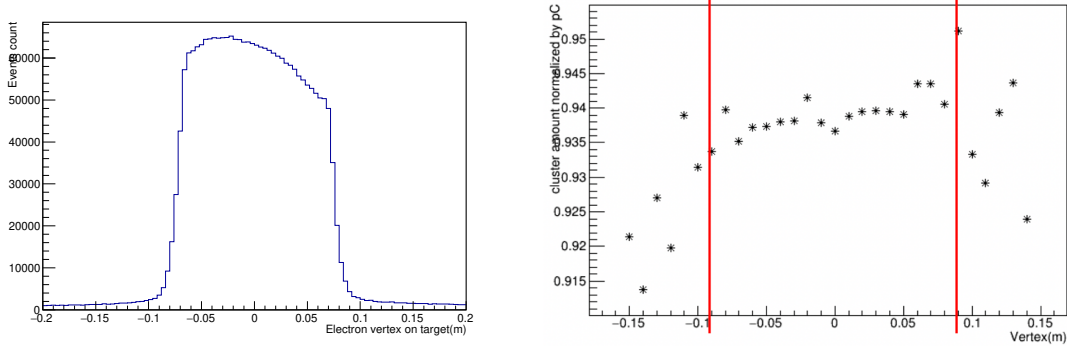


Figure 4-5: Left: The vertex of electron distribution. Right: The photon yield normalized to charge as the function of the vertex.

4.5.5 Beam current

The beam current (or Charge) is monitored by BCM, which is a different data taking system that is not synchronized with trigger in LHRS, and the BCM data is recored to disk every 10 seconds. So only the average current could acquired. Since the beam current is stable during the most time of normal run, it's OK to use average current in 10 seconds as the real current of each event. The current of normal run is $10\ \mu\text{A}$ or $15\ \mu\text{A}$, which is depend on the test configuration. To reject the unstable current events, events with bad current will be abandoned.

4.5.5.1 Beam current calculation

The downstream BCM with 10x amplification factor called D10 is suggested to be used in current calculation because of its good stability and appropriate range. The read-out of BCM related to current need to be calibrated with known current[57]. The average current between two events is calculated as:

$$I_{average} = \frac{(D10_2 - D10_1) \times Gain \times Clk_rate}{Clk_2 - Clk_1} + Offset \quad (4-5)$$

where D10 is the scaler count from D10, Gain is the parameter transferring the scaler count to current from 2016 Spring beam current calibration test result, it's $32.14 \times 10^6 \mu\text{A}$.

Clk is scaler count of Hall A time count scaler. Clk_rate is the clock frequency of Hall A time count scaler, which is equal to $1.037 \times 10^5 Hz$. Offset is $0.19\mu A$, acquired from same calibration of Gain.

4.5.5.2 Beam current cut

Since the current is the average current of 10s, for the events with unstable beam current, such as the beginning of beam delivery, the real current is differ with the average current. To select events with good current, a current cut is applied to abandon the events that current in which is not equal to the expected data taking current.

Fig.4-6 shows the photon yield normalized to the charge as a function of current. Results shows the events of current that not in normal data taking current range has a larger ratio. The reason is, the current could rapidly increase or decrease sometimes, for the unstable beam current events, especially the low average current events, the real current is larger than the average current, so it will lead to the ratio much higher than normal running condition.

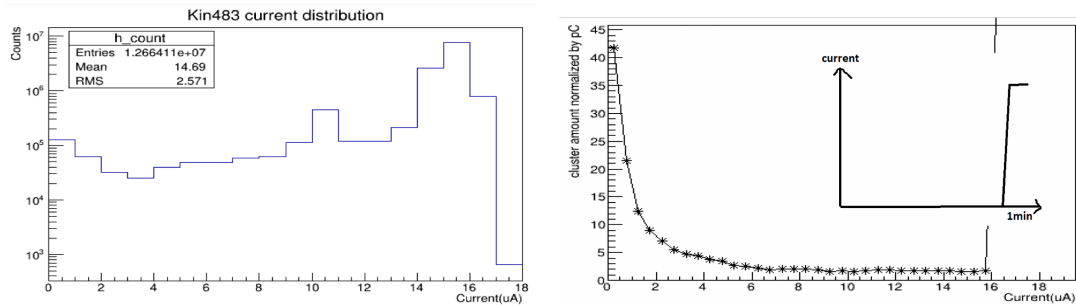


Figure 4-6: Left: the current of events distribution. Right: The photon yield normalized by the charge as the function of the current.

4.6 Summary

This chapter described the method to extract inclusive π^0 cross section from the existing DVCS experiment data. The inclusive π^0 s are recognized in this data based on three vital factors: DIS trigger, the long ARS time window and continuous beam structure. The inclusive π^0 could be found in the non-coincident time window, and event cut is

applied to make sure the quality and unbiasedness of time window. Since the DVCS data is not an ideal data for this analysis, it has some restrictions. These restrictions are considered and remedied in analysis, and also will be evaluated as an error in the following content.

Once the electron cut is applied and trigger events are selected, the next work will mostly focus on the photon signal analysis in calorimeter, which will be described in next chapter.

Chapter 5

DVCS Calorimeter analysis and calibration

DVCS calorimeter play a crucial role in π^0 analysis, and it's the detector that own all photon information. Since the quality of signal in calorimeter dominate the photon reconstruction, the signal must be extracted and calibrated precisely and carefully. However, since the high luminosity and the detector is placed quite close to the target, it leads to high background and pile-up photons. Also, the waveform recording time window is 128 ns, considering 4 ns beam bunch interval, total 32 bunches are recorded in a single waveform, and if the time resolution is not good enough, failing to separate "continuous" beam bunches makes the analysis much more difficult.

The calorimeter analysis starts from the raw data of each calorimeter block that is the points in waveform. The first step is recognizing pulse and extract the time and maximum amplitude of each pulse. To correct the time and acquire energy, then time correction and energy calibration is performed, and every kinematic has individual calibration parameter. Finally, after finishing the analysis of every block, gather blocks to form cluster and reconstruct photon. This sequence is not fixed, such as the energy calibration need cluster algorithm.

Here we briefly introduce the meaning of some important words related to the calorimeter analysis:

- Trigger event: A whole event including all signal information of calorimeter. If not specified, an event means a trigger event.

- Block: It's one of 208 calorimeter blocks and the minimum analysis unit in geometry.
- Pulse: Signal appears in a block, extracted from ARS waveform, and it's a part of cluster.
- Beam bunch: The time structure of electron beam, the time interval between bunches is 4 ns.
- Cluster: A cluster includes several pulses in adjacent blocks, contain energy, time and position information.
- Photon event: with vertex information, the 4-momentum of a photon could be reconstructed by a cluster.

5.1 Waveform analysis

The purpose of waveform analysis is extracting time and amplitude from raw ARS pulse points in single block. The extracted time is the raw pulse time ready for time correction, and with energy calibration correction, the amplitude multiplied by energy coefficient is equivalent to energy. The ARS electronics just like oscilloscope, could store 128 ns waveform, including full shape of pulse. In order to acquire more accurate time and amplitude information considering signal pile-up, a delicate offline waveform analysis is performed.

5.1.1 Baseline fitting

For most blocks in one event, there is no photon hit on these blocks, and only noise appear in waveform. Before performing waveform analysis, these blocks with no signal should be excluded firstly. For each block, the average amplitude b is calculated as:

$$b = \frac{1}{i_{max} - i_{min}} \sum_{i=i_{min}}^{i_{max}} x_i \quad (5-1)$$

where i_{max} and i_{min} are the time window in ns for waveform analysis, x_i is the amplitude of each 1ns ARS point in DAQ channel unit. To fully use the accidental events for inclusive π^0 analysis, the time window is set as wide as possible. To evaluate if a pulse exists, define

$$\chi^2 = \sum_{i=i_{min}}^{i_{max}} (x_i - b)^2 \quad (5-2)$$

If the χ^2 is smaller than a χ_0^2 threshold value, that means the amplitude of all points are similar, so no signal in this block. In this case, only a baseline fitting is good enough. If the χ^2 value is larger than χ_0^2 , we believe a pulse exists in this waveform, and further waveform analysis will be performed as described in next sections.

5.1.2 One-pulse fitting

Once the waveform pass the baseline fitting, at least one pulse could be found in it. We use an ideal reference shape to fit the pulse signal, and the waveform algorithm is based on the assumption that the shape of pulse is independent of energy and time. Actually, pulse shape is affected by signal pile-up and PMT photons collection. The ideal reference shape is the average shape of each block and obtained from elastic calibration runs that have no pile-up events.

For the case that the detected photons are coincident with electron, which means time =0, only amplitude is unknown. Amplitude a could be simply given by minimizing

$$\chi^2 = \sum_{i=i_{min}}^{i_{max}} (x_i - ah_i)^2 \quad (5-3)$$

where h_i is the amplitude of reference shape points, in which max amplitude is uniformed to 1. A sample of one-pulse fitting is shown in Fig.5-1.

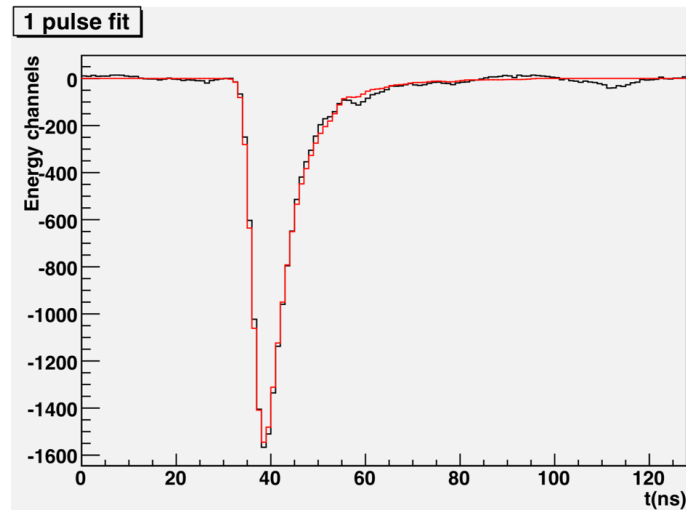


Figure 5-1: The one pulse fit of ARS waveform.

Usually, the pulse occurs at any time in ARS time window, the arrival time of pulse also need to be considered. To get best time fitting, we use every possible arrival time

from i_{min} to i_{max} with 1ns step, just like shifting the reference shape with time t . χ_t^2 is computed as:

$$\chi_t^2 = \sum_{i=i_{min}}^{i_{max}} \left(x_i - a(t)h_{i-t} - b(t) \right)^2 \quad (i_{min} < t < i_{max}) \quad (5-4)$$

There are two parameters: amplitude $a(t)$ and baseline $b(t)$ that is not same as base-line fitting showed above. For each time t , to minimize χ^2 , derive χ^2 respect to $a(t)$ and $b(t)$ separately:

$$\frac{\partial \chi_t^2}{\partial a(t)} = -2 \sum \left(x_i - a(t)h_{i-t} - b(t) \right) h_{i-t} = 0 \quad (5-5)$$

$$\frac{\partial \chi_t^2}{\partial b(t)} = -2 \sum \left(x_i - a(t)h_{i-t} - b(t) \right) = 0 \quad (5-6)$$

These two equations could be rewritten as:

$$\begin{pmatrix} \sum x_i h_{i-t} \\ \sum x_i \end{pmatrix} = \begin{pmatrix} \sum h_{i-t}^2 & \sum h_{i-t} \\ \sum h_{i-t} & \sum 1 \end{pmatrix} \begin{pmatrix} a(t) \\ b(t) \end{pmatrix} \quad (5-7)$$

After calculating all possible time t , we get the minimum χ_t^2 with specific t . Now from one pulse fitting, the arrival time t , amplitude a and the baseline b is extracted.

5.1.3 Two-pulse fitting

Sometimes the one pulse fit is not good enough, and the minimum χ^2 is still too large. It means the waveform may include two pulses. So the two pulse cut χ_1^2 is set to check if the two pulse fitting is necessary. To fit with two pulses, define amplitude of two pulses $a_1(t_1, t_2)$ and $a_2(t_1, t_2)$, time t_1 and t_2 , also the baseline $b(t_1, t_2)$. The $\chi^2(t_1, t_2)$ of two pluses fitting is:

$$\chi^2(t_1, t_2) = \sum_{i=i_{min}}^{i_{max}} \left(x_i - a_1(t_1, t_2)h_{i-t_1} - a_2(t_1, t_2)h_{i-t_2} - b(t_1, t_2) \right)^2 \quad (5-8)$$

The equation could be minimized as:

$$\begin{pmatrix} \sum x_i h_{i-t_1} \\ \sum x_i h_{i-t_2} \\ \sum x_i \end{pmatrix} = \begin{pmatrix} \sum h_{i-t_1}^2 & \sum h_{i-t_1} h_{i-t_2} & \sum h_{i-t_1} \\ \sum h_{i-t_1} h_{i-t_2} & \sum h_{i-t_2}^2 & \sum h_{i-t_2} \\ \sum h_{i-t_1} & \sum h_{i-t_2} & \sum 1 \end{pmatrix} \begin{pmatrix} a_1(t_1, t_2) \\ a_2(t_1, t_2) \\ b(t_1, t_2) \end{pmatrix} \quad (5-9)$$

The solution of this equation will try all t_1 and t_2 combinations, finally get the minimum $\chi^2(t_1, t_2)$.

We use two pulses fitting to extract pile-up events, however if the arrival time of

two pulses is very close, it is hard to separate these two pulses from fitting. If the time difference of these two pulses is less than the time resolution $\Delta\tau$ (4ns), we reject the two-pulse fitting, and use the one-pulse fitting result. Similarly it is possible to extract pulse using three-pulse fitting, but the efficiency is really slow, adding t_3 will consume more than 128 times time compared to two-pulse fitting. Considering the three-pulse event is rare and time resolution $\Delta\tau$ restriction, even if two-pulse fitting could reach a better than 5% energy resolution, two-pulse fitting is good enough for analysis.

5.1.4 Waveform analysis optimization

To contain as many as bunches for inclusive π^0 analysis, the time window $[i_{min}, i_{max}]$ should be set as wide as possible. However the time window at the edge is ignored. Because if a photon arrives at the edge of ARS time window, where the waveform is incomplete, there will be a large error in analysis. The other reason is there is a relative time difference between 208 blocks, which makes the time window of each block have a different start and end time. With optimization, the time window is set to [-36 ns, 80 ns] related to the coincidental time.

The time extracted from the pulse fitting is restricted by the 1 ns ARS time resolution. In order to improve time resolution, interpolating with a quadratic function is applied. Take three points $(t-1, \chi_{t-1}^2)$, (t, χ_{min}^2) , $(t+1, \chi_{t+1}^2)$ into a quadratic function, minimize the χ^2 to get the optimized $t_{optimized}$:

$$t_{optimized} = t(\chi_{min}^2) + \frac{\chi_{t-1}^2 - \chi_{t+1}^2}{2(\chi_{t+1}^2 + \chi_{t-1}^2 - 2\chi_{min}^2)} \quad (5-10)$$

where $t(\chi_{min}^2)$ is time t with minimum χ^2 from pulse fitting.

The threshold values of χ_0^2 and χ_1^2 determine if one or two-pulse fitting is applied. The values are optimized by studying:

1. The energy resolution of the calorimeter.

Bad threshold will miss or add low energy pulses, making the energy resolution worse.

2. The number of π^0 like events compared to total events.

π^0 like events are the events with two photons and the invariant mass passes the cut. The number of π^0 like events decreases obviously when χ_1 is set smaller because π^0 needs an extra photon to reconstruct, which is more liable to be ignored in 2-pulse

fitting.

3. The computation time.

CPU time increase significantly with lower χ_1 value.

Combine these factors, study shows the optimized value of the parameter χ_0 and χ_1 are 60 MeV and 200MeV separately[58]. It provides a balance between waveform quality and analysis time.

5.2 Calorimeter time calibration and optimization

One of important factor in any timing system is its resolution, and good time resolution tell us whether two particles are coincident or not. For an DVCS triggered event includes an electron and a photon,

$$T_{electron} = t_{generate} + t_{electron_propagation} \quad (5-11)$$

$$T_{photon} = t_{generate} + t_{photon_propagation} \quad (5-12)$$

where the $T_{electron}$ is the LHRS trigger time, and $t_{generate}$ is the time particles generated from vertex. So, the difference between electron and photon equal to:

$$T_{photon} - T_{electron} = t_{photon_propagation} - t_{electron_propagation} \quad (5-13)$$

We only care the deviation of time difference in this equation, which is essential to verify the coincidental relation of electron and photon.

If we know well the propagation time of electron and photon in each event, the deviation of time difference will be small. Actually, the time difference is affected by detector and DAQ system event by event, and time difference deviation is increased significantly. As seen in Fig.5-2, without time correction, the raw time in DVCS calorimeter blocks is really in a mess.

To separate photon pulse from continuous beam bunches, the time resolution of pulse must be significant less than the bunch interval. If the time resolution larger than 1 ns, some signals in one beam bunch will appear in other adjacent bunch, which will generate more accidental π^0 events. So a good time resolution is required, and it needs delicate care to each calibration steps.

The main purpose of time correction is to separate blocks signal in different bunch, and make sure the blocks in reconstructed photon clusters are really belong to that bunch.

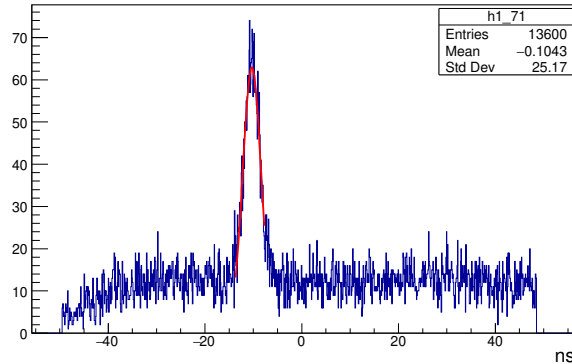


Figure 5-2: The raw pulse time distribution acquired from pulse analysis in one block.

The time correction process is based on the peak of photon time that coincident with electron and the peak could be seen in Fig.5-2. Once the coincident time is corrected, with fixed bunch interval time, the time of other beam bunch in same event will be corrected simultaneously. The time correction process include these important steps:

1. Jitter in trigger
2. 208 calorimeter blocks time offset
3. Sixteen S2m scintillator paddle offset
4. Propagation time in S2m scintillator
5. Electron path/momentum in LHRS
6. Time walk correction

There are cuts on event selection, which is similar with DVCS experiment general cut. Since we have enough events, the cut is strict and described as:

- Good electron cut
- Target Vertex cut
- Tracking cut
- Only one hit on all S2m scintillator paddles
- Each pulse energy > 250 MeV

Each DVCS kinematic have a different LHRS and DVCS calorimeter configuration, so independent calibration is performed for each kinematic and different calibration coefficient is used in each kinematic.

5.2.1 ARS stop trigger jitter

There is a time jitter between S2m time and ARS stop time. When the S2m is triggered, the electronic will check calorimeter ADC signal and decide if the data is recorded. This time difference is not a constant, and each event has a different jitter. Before any other correction, jitter correction must be performed firstly. The ARS stop trigger jitter correction is given by

$$t_{correct} = t_{raw} - (t_{S2m} - t_{ARS\ stop}) \quad (unit : ns) \quad (5-14)$$

where $t_{correct}$ is the time after correction, t_{raw} is the raw time of pulse from waveform analysis, t_{S2m} is the S2m TDC value, $t_{ARS\ stop}$ is the time ARS stop refreshing and freeze. The LSB of trigger TDC is 100 ps, which is 1/10 compared to ARS 1 ns LSB time.

5.2.2 Calorimeter block time offset

Photons arrive at calorimeter before the final trigger is decided. When the calorimeter is waiting the trigger's decision to record the calorimeter data, the single of each block is stored in a long cable. The energy of a photon is deposited in several adjacent blocks, and each block have a different propagation time. To reconstruct this photon event, time of all blocks must be aligned. This is the only time correction for calorimeter, and it contains several aspects of time difference between blocks, such as:

- Different distance from target to calorimeter detector block
- PbF_2 crystal response time
- PMT transmit time difference
- Propagation time in long cable

All these time difference could be combined to the $t_{photon_propagation}$ for each block. The calibration is simply described as:

$$t_{correct} = t_{corrected} - \Delta t_i \quad (i = 0, 1, \dots, 207) \quad (5-15)$$

where $t_{corrected}$ is the corrected time after all previous correction, Δt_i is relative average time difference for block i , acquired from the fitting of each block's coincidental peak.

5.2.3 S2m scintillator paddle offset

The trigger time is determined by sixteen S2m scintillator paddles with the OR logic. The signal of right side PMT coupled to scintillator is delayed by cable to make sure it always arrives later than all other detectors in trigger DAQ. Each paddle could form the trigger independently, and each paddle is different offset time, which is calibrated as:

$$t_{correct} = t_{corrected} - \Delta t_k \quad (k = 0, 1, \dots, 15) \quad (5-16)$$

where Δt_k is the relative average time difference for scintillator paddle k.

5.2.4 Propagation time in scintillator

The hit position on scintillator also influence the relative time between electron and photon. The size of scintillator paddle is 43 cm in length, 14 cm in width and 5 cm in thickness[59]. Considering the index of refraction of scintillator 1.5, the photon propagation time in scintillator is at most 2 ns before collected by PMT, which is really a large deviation.

From tracking information, hit position on scintillator could be acquired. To correct propagation time in scintillator, the function between calorimeter pulse arrival time and hit position along the long side scintillator paddle is studied. Fig.5-3 shows the relation between hit position and arrival time, fitted with a quadratic function and shows good fitting consistency. The time corrected by hit position x in paddle k is given as:

$$t_{correct} = t_{corrected} - \Delta t_k(x) \quad (k = 0, 1, \dots, 15) \quad (5-17)$$

5.2.5 Electron path/momentum in LHRS

The LHRS magnetic field accept momentum of electron in a narrow range, and different momentum has different track, which conclude a different track length in LHRS. Even if the momentum difference is little, considering the long tracking from target to S2m scintillator, time difference is still significant, which is shown in Fig.5-4. This momentum difference Δp of each electron is constructed by tracking, and the real momentum of each electron is:

$$p_{electron} = \Delta p + p_{LHRS} \quad (5-18)$$

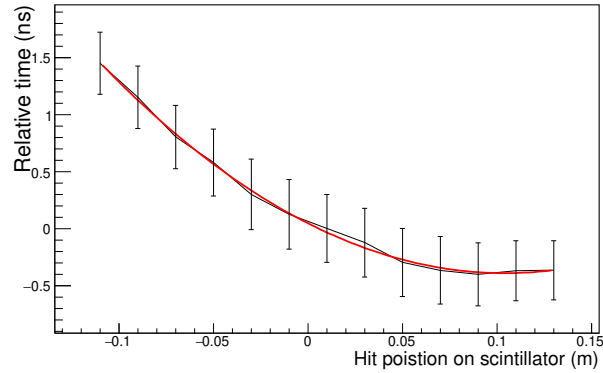


Figure 5-3: The time difference as a function of hit position on a S2m scintillator. The error bar shows the sigma of each energy bin's fitting. The PMT is coupled at the right side of plot (positive x).

where p_{LHRS} is the central momentum setting of LHRS magnet. A linear relation was observed and the time correction was applied for the momentum difference Δp in a similar fashion:

$$t_{correct} = t_{corrected} - \Delta t_k(\Delta p) \quad (k = 0, 1, \dots, 15) \quad (5-19)$$

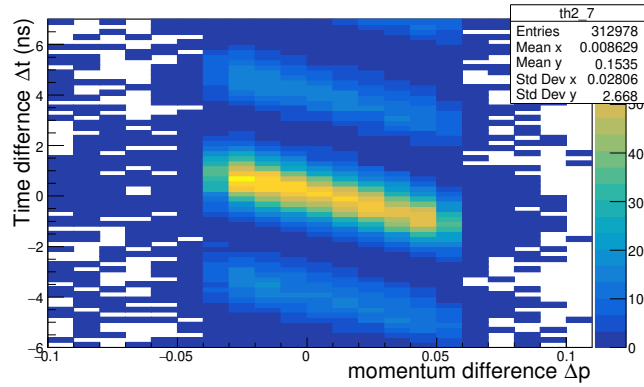


Figure 5-4: The time difference between pulse time and trigger time as a function of momentum difference in one of S2m scintillators. Plot shows a significant linear relation.

5.2.6 Time walk correction

The influence of trigger scintillator amplitude on the time resolution is called time walk. Particle deposit energy in scintillator through ionization process following Landau distribution, so the energy deposit in S2m is different event by event. Time is determined by discriminator when the signal larger than a fixed threshold. However, as shown in Fig.5-5, the difference in amplitude of signal will lead to a different trigger time. Practically, the time walk could be corrected as a root square function of charge Q (area) from S2m:

$$t_{correct} = t_{corrected} - \Delta t_k(\sqrt{Q}) \quad (k = 0, 1, \dots, 15) \quad (5-20)$$

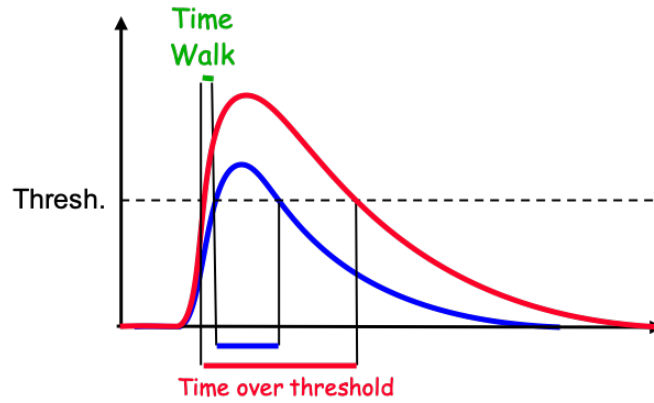


Figure 5-5: Illustration of time walk affect. Two pulses have same peak time, but the pulse with higher amplitude(red) pass threshold earlier than lower amplitude pulse(blue).

5.2.7 Conclusions

Combine all the corrections shown above, the final equation of time correction is

$$t_{correct} = t_{raw} - (t_{S2m} - t_{ARS\ stop}) - \Delta t_i - \Delta t_k - \Delta t_k(x) - \Delta t_k(\Delta p) - \Delta t_k(\sqrt{Q}) \quad (5-21)$$

After all the time correction shown in above, starting from standard deviation about 2 ns, and finally reduce to an average 0.6-0.7 ns time resolution with 250 MeV pulse energy cut, which is shown in Fig.5-6. This time resolution result satisfy the requirement to separate photon in adjacent beam bunches.

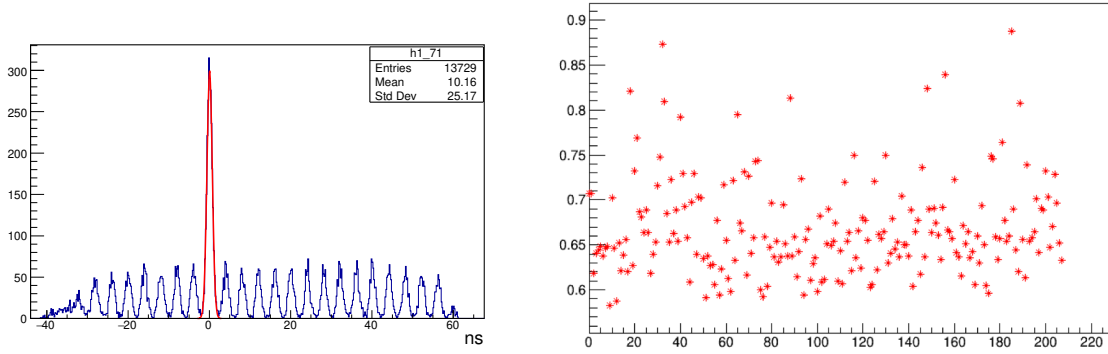


Figure 5-6: Left: The time distribution of pulse in the same block shown in Fig.5-2 after all time correction. Right: The time resolution of each calorimeter block with a 250 MeV energy cut. The x axis is the block number.

5.3 Calorimeter Energy Calibration

The purpose of calorimeter coefficient is to match the amplitude of signal with its real energy deposit in calorimeter. The calibration process include the cosmic rays calibration, elastic scattering energy calibration, also radiation damage calibration and low energy photon calibration based on the invariant mass of π^0 .

5.3.1 Cosmic rays uniformity calibration

Cosmic ray runs are performed with a special calorimeter trigger that triggered by calorimeter itself when there is no beam. It's the first calibration through adjusting the HV of each PMT to align the gain of PMTs. The purpose of this calibration is to uniform the signal output of all the blocks.

Monte Carlo Simulation shows cosmic ray deposit about 35 MeV energy per block, corresponding to 35 Cherenkov photons on average when pass through vertically. In order to make sure each tracking length of cosmic ray is same, only vertical cosmic ray is selected to analyze offline. Since the cosmic ray rate is low, pulse fitting is not necessary in analysis, just integrating the ARS channels is sufficient. The gain of PMT is based on the HV supply, and each PMT has a different coefficient, given by:

$$G = \alpha V^\beta \quad (5-22)$$

where the G is absolute gain of PMT, V is HV, β value is around 7 for all PMTs. With adapting the HV of each PMT, the signal output of all blocks are uniformed, and ready for the calibration to acquire calibration coefficient.

5.3.2 Elastic calibration

The elastic calibration is performed at the beginning and middle of each run period. To calibrate the absolute signal-energy response, beam test with known energy of electron is performed. The elastic scattering reaction ($e+p \rightarrow e'+p'$) is used to perform the calibration, in which proton is detected in LHRS and elastic scattered electron deposit its known energy in calorimeter.

For each event n , the energy of scattered electron E_n is calculated as:

$$E_n = E_b + M_p - E_{p,n} \quad (5-23)$$

where E_b is beam energy, since the initial state of proton is still, M_p is mass of proton which the energy of still proton, and $E_{p,n}$ is energy of recoiled proton detected in LHRS. The E_n is calculated energy deposit in calorimeter, and used for calibration.

The energy of electron deposit like a shower in calorimeter, and leave signal in several adjacent blocks. The total reconstructed energy is the energy sum over these blocks, described as:

$$E_{n,re} = \sum_{i=0}^{207} (C_i A_{i,n}) \quad (5-24)$$

where $E_{n,re}$ is reconstructed energy, $A_{i,n}$ is the amplitude of block i in event n given from waveform analysis, C_i is the calibration coefficient of block i , which is ready to calculate.

To get the coefficients, define χ^2 :

$$\chi^2 = \sum_{n=1}^{N_{events}} (E_n - \sum_{i=0}^{207} (C_i A_{i,n}))^2 \quad (5-25)$$

Minimize χ^2 by deriving χ^2 respect to all the C_k separately,

$$\frac{\partial \chi^2}{\partial C_k} = -2C_k \sum_{n=1}^{events} (E_n - \sum_{i=0}^{207} C_i A_{i,n}) A_{k,n} = 0, \quad \forall k = 0, 1, 2, \dots, 207 \quad (5-26)$$

Equal to:

$$\sum_{i=0}^{207} C_i (\sum_{n=1}^{events} A_{i,n} A_{k,n}) = \sum_{n=1}^{events} E_n A_{k,n}, \quad \forall k = 0, 1, 2, \dots, 207. \quad (5-27)$$

Because $\sum_{n=1}^{events} A_{i,n} A_{k,n}$ and $\sum_{n=1}^{events} E_n A_{k,n}$ could be calculated as constants, we get

208 equations with the 208 variables C_i . Solving the equations will extract the energy coefficient C_i in each block.

The calorimeter energy resolution and angular resolution shows the calibration accuracy and also the intrinsic property of calorimeter. However this work is low efficiency and only care about high energy electron, and resolution of low energy electron is worse.

The energy resolution is defined as:

$$\text{Energy resolution} = \frac{\sigma_E(E_{HRS} - E_{calo})}{\langle E_{calo} \rangle} \quad (5-28)$$

where E_{calo} is the reconstructed electron energy with achieved coefficient C_i , and $\langle E_{calo} \rangle$ is average energy of reconstructed electron. The energy resolution result is shown in Table 5-1, and this energy resolution result is worse compared to other type calorimeters.

The angular resolution includes two angles: the horizontal plane (θ) and the vertical plane (ϕ). Similar as energy calibration, the angular resolution is given by:

$$\Delta\theta = \theta_{HRS}^e - \theta_{calo}^e, \quad \Delta\phi = \phi_{HRS}^e - \phi_{calo}^e \quad (5-29)$$

where θ_{HRS}^e and ϕ_{HRS}^e reconstructed from recoiled proton, θ_{calo}^e and ϕ_{calo}^e reconstructed by calorimeter itself.

Calibration test	E_{beam} (GeV)	$E_{electron}$ (GeV)	$\sigma(\Delta E)$ (GeV)	Resolution (%)	$\Delta\phi$ (mrad)	$\Delta\theta$ (mrad)
February 2016	4.4	3.1	0.144	4.65	2.10	1.67
April 2016	4.4	3.1	0.153	4.94	2.03	1.71
October 2016	6.45	4.2	0.133	3.17	1.72	1.41
December 2016	6.45	4.2	0.154	3.67	1.64	1.36

Table 5-1: The energy and angle resolution result of elastic scattering calibration in 2016.

5.3.3 Radiation damage calibration by π^0 event

With high beam luminosity, the crystal transparency of calorimeter under radiation will get worse significantly over time, which lead to a loss of collected photons in PMT. Fig.5-7 shows the reconstructed invariant mass of π^0 as experiment goes on, and this significant continuous loss of energy must be corrected. The action of elastic calibration is low efficient, and can't be performed often. One possible calibration is based on the radiation dose between two elastic calibrations, but it only works with the ideal assuming

that the change of coefficient is linear to radiation dose. A more accurate method with invariant mass of π^0 is described in the following.

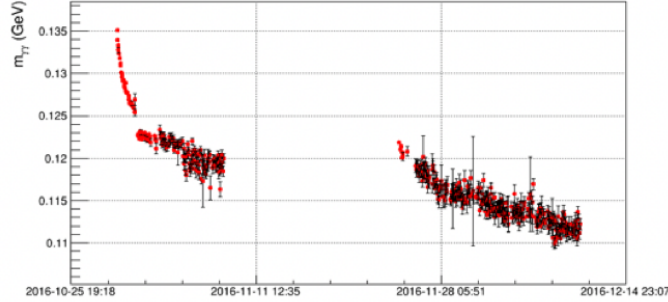


Figure 5-7: The reconstructed invariant mass of π^0 as a function of time in Fall 2016 run period. This calculation use same energy correction coefficient from original elastic calibration.

5.3.3.1 π^0 calibration algorithm

The calibration is based on the reconstruction of π^0 's invariant mass in process $ep \rightarrow e'p'\pi^0$. The algorithm described in [60] is applied.

For the two photons from π^0 decay, their energy are p_{n1} and p_{n2} , and angle between them is θ_n . The invariant mass m_n of π^0 in event n is:

$$m_n^2 = 2p_{n1}p_{n2}(1 - \cos(\theta_n)) \quad (5-30)$$

and p_{nj} is equal to the energy sum of blocks:

$$p_{nj} = \sum_{i \in \text{cluster}} E_{nj}^{(i)} \quad (5-31)$$

where $E_{nj}^{(i)}$ is the measured energy of photon j in block i for event number n. j has the value 1 and 2.

Assuming the energy correction factor ϵ_i , energy is corrected as:

$$E_{nj}^{\prime(i)} = (1 + \epsilon_i)E_{nj}^{(i)} \quad (5-32)$$

To get ϵ_i , define the quantity F:

$$F = \sum_{n=1}^{\text{events}} (m_n^2 - m_0^2)^2 + 2\lambda \sum_{n=1}^{\text{events}} (m_n^2 - m_0^2) \quad (5-33)$$

where $m_0 = 0.1349 \text{ GeV}$ is the π^0 expected mass in theory, and λ is a Lagrange multiplier. The first term in the right equation relevant to reconstructed π^0 invariant mass's energy

resolution, while the second term use Lagrange multiplier λ to embody the constraint $\langle m_n^2 \rangle = m_0^2$.

Minimizing F directly by the correction factor ϵ_i is difficult since the nonlinear dependence of m_n^2 . Since ϵ_i is small, and the variation in angle θ_n is negligible, we get approximation:

$$\frac{\partial m_n^2}{\partial \epsilon_i} \approx m_n^2 \frac{E_{nj}^{(i)}}{\sum_i E_{nj}^{(i)}} \quad (5-34)$$

Minimize F by deriving with respect to ϵ_i :

$$\frac{\partial F}{\partial \epsilon_i} = 2 \sum_{n=1}^{events} (m_n^2 - m_0^2) \frac{\partial m_n^2}{\partial \epsilon_i} + 2\lambda \sum_{n=1}^{events} \frac{\partial m_n^2}{\partial \epsilon_i} = 0, \quad \forall i = 0, 1, \dots, 207 \quad (5-35)$$

Solving the equation 5-34 and 5-35 will extract the correction ϵ_i . We have assumption that ϵ_i is small, however it not always in this case. To correct for the large ϵ_i , several iterations of repeating process is applied until $\epsilon_i \rightarrow 0$. With l times iteration, the final correction coefficient $C_i^{\pi^0}$ is

$$C_i^{\pi^0} = \prod_{l=1}^{l_{max}} (1 + \epsilon_{i,l}) \quad (5-36)$$

$$E_{nj}^{(i)} \rightarrow C_i^{\pi^0} E_{nj}^{(i)} \quad (5-37)$$

5.3.3.2 Calibration optimization and result

One challenge of π^0 calibration is the statistics, which makes the calibration be performed not so often. Each calibration need about $10^5 \pi^0$ events at least, one day's data is required to satisfy the statistics. This calibration method works for most runs during the experiment. However for some other run periods, the gain loss is fast in one day. Without enough π^0 events, the correction can't be performed several times in one day, which lead to bad precision. To deal with this issue, instead, the calibration coefficient is just achieved by the ratio of expected π^0 invariant mass m_0 compared to the constructed value from elastic calibration:

$$C_i^{\pi^0} \rightarrow C_i^{\pi^0} \frac{m_0}{m_{reconstruct}}, \quad \forall i = 1, \dots, 208 \quad (5-38)$$

5.3.4 Low energy photon correction

The energy calibration described above only care about high energy photons. As seen in the left plot of Fig.5-8, the invariant mass ratio has a good consistency for high energy π^0 invariant mass, but there is a large deviation for the low energy π^0 , which means the energy calibration coefficient is not strictly linear. So additional low energy correction need to be considered.

The ideal coefficient should be a function of both block and energy. To simplify, the energy correction is corrected by the invariant mass of π^0 with quadratic function, described as $C_i(E)$. The invariant mass of π^0 after this correction is shown in Fig.5-8.

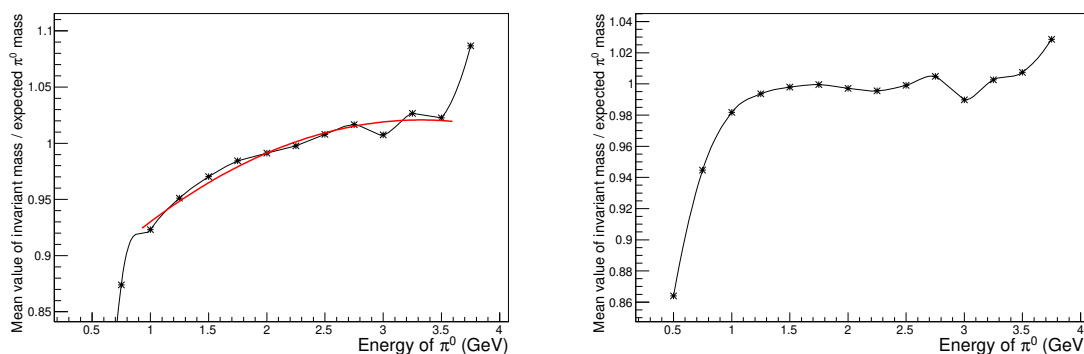


Figure 5-8: Left: the ratio that the mean value of candidate π^0 's invariant mass compared to the expected π^0 mass (0.135 GeV) as a function of π^0 energy. Each point is acquired from the fitting of two clusters' invariant mass. Right: the same ratio after low energy correction.

5.3.5 Summary

After these four energy calibrations steps, the energy could reconstructed from amplitude a of a pulse by:

$$E_i = a \cdot C_i(kin) \cdot C_i^{\pi^0}(run) \cdot C(kin, E) \quad (5-39)$$

where $C_i(kin)$ is acquired from elastic calibration, depend on kinematics setting, $C_i^{\pi^0}$ is the radiation correction coefficient, depend on runs, and $C(kin, E)$ is coefficient acquired from low energy calibration.

5.4 Cluster algorithm

The final purpose of DVCS calorimeter analysis is reconstructing photon's energy, time and position information. The analysis and calibration showed in above is focus on pulse analysis, which is just the waveform of one block. The cluster is defined as a photon event that include signal in several blocks. The energy of a photon mostly deposit in one central calorimeter block, and the rest deposit in several adjacent blocks. For the time information, photons may occur at any time in 128 time window, and need to make sure which beam bunch each photon belongs to. The difficulty of cluster analysis is that if many clusters exist in one event, it's hard to separate clusters, and especially for the two cluster events in the same beam bunch in π^0 analysis.

5.4.1 Pulse selection in bunch

To perform cluster analysis, the first step is sorting all the pulses signals in blocks to the beam bunch that it belongs to.

For π^0 event reconstruction, the candidate two photon clusters must exist in the same beam bunch which is a 4 ns time window. For the total 128 ns time window, there are about 30 bunches are chosen in analysis. Each triggered event may include several clusters in different bunches. To separate adjacent beam bunches, the time resolution must be good. As showed in Section 5.2.7, the time resolution of pulse is 0.7 ns, which could clearly separate the bunches.

To contain all possible pulses in one bunch, the time window of selecting pulses is set a little larger than 4 ns bunch time. With optimization, the final time window for analysis is [-2.1 ns, +2.1 ns] related the center time of each bunch, which is about three times of time resolution. Although this larger time window include pulses from adjacent bunches, the final cross section analysis with background subtraction could minimize its influence. So the first step of cluster reconstruction is choosing a specific bunch and collect all pulses whose corrected time in this bunch's time window [-2.1 ns, +2.1 ns].

5.4.2 Build cluster with cellular automaton algorithm

The cluster building is focus on all the pulses exist in a specific beam bunch, and use these pulsed to reconstruct different clusters. This algorithm includes two steps: choose candidate blocks satisfy energy cut, and form clusters with these blocks.

After sorting pulse into different bunches based on time, then we focus on energy cut. A cluster must satisfy the energy threshold to reject small energy cluster, which may only the noise. To contain as many as possible low energy clusters, the cluster threshold is set to 0.3 GeV, which is much less than the DVCS cluster trigger threshold 3 GeV. To include blocks with low energy, it's wise to apply this energy cut in a group of blocks. So we check every possible combination of 2×2 adjacent blocks, if the sum of these 4 blocks' energy above energy threshold, all these 4 blocks will be tagged and chosen to next step. A block selection sample is shown in Fig.5-9.

0	0.01	0.02	0.01	0	0
0	0.05	0.05	0.1	0.4	0.1
0.02	0.2	0.5	0.3	1.9	0.1
0	0.3	3.0	0.3	0.3	0
0	0.2	0.2	0.1	0.03	0

0	0.01	0.02	0.01	0	0
0	0.05	0.05	0.1	0.4	0.1
0.02	0.2	0.5	0.3	1.9	0.1
0	0.3	3.0	0.3	0.3	0
0	0.2	0.2	0.1	0.03	0

↓

0	0.01	0.02	0.01	0	0
0	0.05	0.05	0.1	0.4	0.1
0.02	0.2	0.5	0.3	1.9	0.1
0	0.3	3.0	0.3	0.3	0
0	0.2	0.2	0.1	0.03	0

Figure 5-9: An example of checking all blocks in a 2×2 group. If the energy sum above threshold (0.3 GeV), all four blocks except no signal will be tagged. The number written in each block is energy in GeV.

After time and energy cut, most events have no satisfied blocks, but if there are blocks selected after the first step, it means at least one cluster exists. If only one photon hit the calorimeter, all selected blocks belong to this photon cluster. However the case is not always like this, photons will hit the calorimeter simultaneously, especially for the two photons from π^0 decay.

To gather and separate blocks for clusters, a general cluster algorithm called cellular automaton[61] is applied. This algorithm concern the energy maximum block in area,

which mean the energy of other 8 neighboring blocks around it must less than the energy of it, and if there is the energy of another block larger than it, it will never be a maximum block. Each maximum will form a cluster, and expand like virus to contaminate the adjacent blocks round it. As shown in Fig.5-9, the contamination starts from largest energy of all maxima, then takes the value of its highest-value neighbor at each step, until all blocks selected in first step are contaminated. Finally, each contaminated area will be regarded as a cluster.

			0.01		
	0.05	0.05	0.1	0.4	0.1
0.02	0.2	0.5	0.3	1.9	0.1
	0.3	3.0	0.3	0.3	
	0.2	0.2	0.1	0.03	
			0.01		
	0.05	0.05	1.9	1.9	1.9
0.02	3.0	3.0	3.0	1.9	1.9
	3.0	3.0	3.0	1.9	
	3.0	3.0	3.0	0.03	
			1.9		
	3.0	3.0	1.9	1.9	1.9
3.0	3.0	3.0	3.0	1.9	1.9
	3.0	3.0	3.0	1.9	
	3.0	3.0	3.0	3.0	

Figure 5-10: The illustration of cellular automaton algorithm. Top: start from local maximum energy. Middle: the blocks are contaminated by their highest neighbor. Bottom: All blocks are contaminated, and they are classified to two clusters(green and orange).

In some events, two clusters are very close, it's hard to decide which cluster the blocks between two clusters are belong to. Luckily, simulation shows with low energy photon cut, two photons decayed from same π^0 are never too close. If the two clusters satisfied energy cut appears close, one of clusters may come from accidental coincidence.

5.4.3 Cluster reconstruction

Once the blocks and pulses in a cluster are confirmed, the energy, time and hit position of this cluster could be reconstructed by these blocks. The energy of cluster E is just the sum of all blocks belong to it:

$$E = \sum_i E_i = \sum_i C_i A_i \quad (5-40)$$

where E_i is the energy of block i, A_i is the amplitude of pulse from waveform analysis, and C_i the energy coefficient from energy calibration.

The arrival time of cluster is the sum of blocks with energy weight, and block with larger energy influence more the time. The time of cluster is described as:

$$t_{cluster} = \frac{\sum_i E_i t_{correct}}{\sum_i E_i} \quad (5-41)$$

For the hit position reconstruction, since the side length of block is 3cm, a good position algorithm is necessary to improve position resolution. The energy deposit of a cluster is not linear, and most energy is deposited in central area, which shows a logarithmic distribution. With optimization, the hit position in x and y is calculated as:

$$x = \frac{\sum_i w_i x_i}{\sum_i w_i}, \quad w_i = \max\left\{0, W_0 + \ln \frac{E_i}{E}\right\} \quad (5-42)$$

$$y = \frac{\sum_i w_i y_i}{\sum_i w_i}, \quad w_i = \max\left\{0, W_0 + \ln \frac{E_i}{E}\right\} \quad (5-43)$$

where x_i and y_i is the central geometry of block i in x and y direction separately, and W_0 is the weight used to adjust the influence of energy. W_0 offer an energy cut for low energy block, and if the energy of one block less than e^{-W_0} compared to total energy of cluster, this block will be ignored in position reconstruction. On the other hand, W_0 could tune the weight of energy in position reconstruction, and the value should be optimized. If W_0 is very high, each low and high energy block has similar impact on position reconstruction, and if W_0 is small, the impact of high energy block will dominate.

The calculation showed above has the assumption that all energy deposit at the surface of calorimeter. Actually, only a small fraction of energy deposit at the surface, energy is deposited like a shower, and the depth of energy deposited maxima always larger than 5cm. With the correction of depth a , the corrected hit position x_{corr} and y_{corr} would be:

$$x_{corr} = x \left(1 - \frac{a}{\sqrt{L^2+x^2}} \right), \quad (5-44)$$

$$y_{corr} = y \left(1 - \frac{a}{\sqrt{L^2+y^2}} \right), \quad (5-45)$$

where L is the vertical distance from vertex in target to the surface of calorimeter.

The parameter W_0 and a is optimized by Monte-Carlo simulation, W_0 is chosen as $W_0 = 4.3$ in analysis. The value a is related to the energy of cluster, described as a function of E :

$$a = 0.30 \times E^{0.28} + 4.862, \quad (5-46)$$

where the unit of E is in MeV and a in cm.

5.5 Summary

This chapter explains the full process of DVCS calorimeter analysis and calibration. With delicate care of each step, we get a good time correction and energy calibration result, which satisfy the requirement of inclusive π^0 analysis. Photon events are reconstructed with time, energy and position by pulse signal in blocks. These photon events are ready for the π^0 extraction in next step.

Chapter 6

Inclusive π^0 cross section extraction

After the photon events are reconstructed from the calorimeter analysis, now we focus on the π^0 reconstructed by two photons and acquire its final cross section result. Total three kinematic settings are analyzed: two 4-pass (8.5 GeV) and one 5-pass (11 GeV). There is overlap range of two 4-pass setting that have different calorimeter location, and the result of which could be compared to check the result accuracy.

The cross section calculation need the total number of generated π^0 . Because the restriction of detector acceptance, the detector will not detect all the generated π^0 s. These undetected π^0 s can be compensated through simulation. So we get the detected π^0 yield of data firstly, then the cross section could be acquired by comparing this π^0 yield with simulation result.

In this chapter, we will detailedly introduce the photon cut, the simulation, data analysis, the result and also the error in this analysis.

6.1 Data used in analysis

Two configurations of 4-pass (8.5 GeV) data kin48_2 and kin48_3, and one 5-pass (11 GeV) kin48_4 are used in the measurement. For π^0 analysis here, we call them K8_1, K8_2 and K11 separately. The K8_1 dummy target data that has very limited events is also used. These are all the DVCS kinematic settings could be used for the inclusive π^0 cross section extraction purpose between 6 GeV and 11 GeV, and the others kin60 settings, listed in Table 2-3, are abandoned because the time interval of beam bunch is set

to 2 ns, which is impossible to separate adjacent bunches with 0.7 ns time resolution.

The calorimeter position information of these setting is shown in Table 6-1, and illustrated in Fig.6-1 where shows the definition of angle θ and ϕ . The θ is the angle between a particle and beam direction, as described in Eq.4-1, it is related to the cross section calculation. The ϕ is defined as the angle around the beam direction, because the system is axisymmetric, the cross section is not related to it.

DVCS kinematic setting	E_{beam} (GeV)	Calorimeter central angle (degree)	Calorimeter distance (m)
K8_1(kin48_2)	8.520	15.184	2.00
K8_1(kin48_3)	8.520	11.728	2.50
K11(kin48_4)	10.587	10.069	2.50

Table 6-1: The beam energy and DVCS calorimeter setting in the kinematics used in π^0 analysis. The beam energy here is the measured energy.

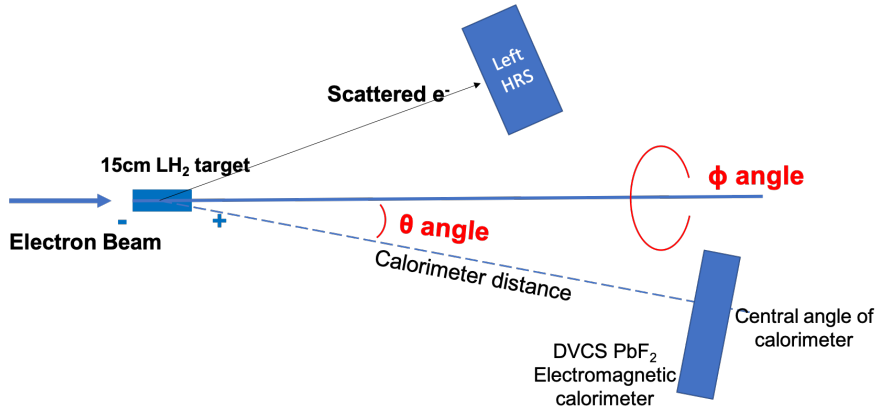


Figure 6-1: The illustration of detectors setting. θ is the angle between a particle and beam direction, ϕ is the angle around the beam. Calorimeter distance is the distance from the target center to the surface of calorimeter.

The number of events in these Kinematic settings are shown in Table 6-2. All the valid events that after event cut will be used for the π^0 s extraction.

6.2 Calorimeter cut

The purpose of calorimeter detector cut is selecting good clusters or photons for further analysis after the raw events cut and photon reconstruction. The calorimeter analysis

Kinematic setting	Total events triggered	Valid events after cut
K8_1	54.0M	14.7M
K8_2	38.9M	11.6M
K11	71.0M	11.9M
K8_1(dummy)	220k	73k

Table 6-2: The events in each setting that could be used for π^0 analysis.

described in last chapter keeps as many candidate photon clusters as possible without any bias in reconstruction. To make sure the quality of photons from reconstruction, calorimeter cuts must be applied. These cuts mainly focus on three points: energy, geometry and the time.

The calorimeter reconstructs photons accurately in its well-known acceptance. Photons with worse reconstruction must be discarded, which is based on the calorimeter cut. The impact of some cuts could be evaluated and compensated by simulation, and some can't. Also, any cuts performance will decrease the statistics and may lead to artificial bias, which need to be taken care more patiently, and the error of these cuts are also studied in the error evaluation section.

6.2.1 Photon energy cut

The photon energy cut is applied to ignore the low energy clusters. In order to reconstruct the π^0 s as many as possible, especially for the low energy ones, the single photon energy cut should be low. However,

- Since there is no hardware cut on calorimeter, all signal will be recorded. There are much more low energy photons, and the accidental coincidence of those two photons contribute to a high background in analysis.
- Since the energy resolution restriction, the energy calibration and photon cluster reconstruction of low photons is not as good as high energy ones.
- The geometry restriction of calorimeter detector makes that π^0 s whose energy above 1 GeV could be detected, which described in Sect.4.4.3.

With these considerations, the energy cut of single photon is set to 0.5 GeV, which is higher than the 0.3 GeV threshold in cluster reconstruction and much lower than the 2 GeV energy cut in DVCS analysis. The energy cut could be compensated by simulation,

and will not influence the final result ideally.

6.2.2 Calorimeter Geometry cut

If a photon hit the edge of calorimeter, a part of its energy will leak, which cause a missing energy in photon reconstruction, even if the *Möller* radius of photon cluster in PbF_2 is small (2.2 cm). To avoid this error in photon energy reconstruction, photon clusters whose hit position on the edge of calorimeter must be cut off. For convenience, clusters that the distance to the calorimeter edge less than 3 cm is discarded, the value of which is equal to the size of a crystal block.

6.2.3 Beam bunch selection

The beam structure is consist of "continuous" bunches, which is separated with 4 ns interval. Each bunch is a very short electron cluster, and only the two photons exist in same bunch will be selected as a candidate π^0 . Good time resolution is needed to separate photons from adjacent bunches, and for achieved 0.7 ns time resolution, the runs with 4 ns interval are separated successfully.

The total time window of the ARS electronics is 128 ns, which means at most contain 32 bunches. The bunch selection is based on the time window $[i_{min}, i_{max}]$ selection in pulse fitting, which ignores the bunches at the edge of ARS time window. Fig.6-2 shows the number of π^0 's distribution in different beam bunch, where the bunches at the edge have significant less π^0 's and bunches in accidental time window have uniform π^0 number.

We also discard the two bunches adjacent to the coincident bunch, which have more π^0 events. The reason is that the clusters in coincident bunch are possible to be reconstructed in these two bunches. So we have 6 bunches before coincident time, 18 bunches after that, and 24 bunches in total. This bunch selection means for each triggered event, a total $24 \times 4 = 96$ ns time window is opened to search for the π^0 's.

6.2.4 Time difference between two photons

The time difference of two photons that decayed from a π^0 must be very short, and should be less than the two accidental coincidence photons averagely, the time of which

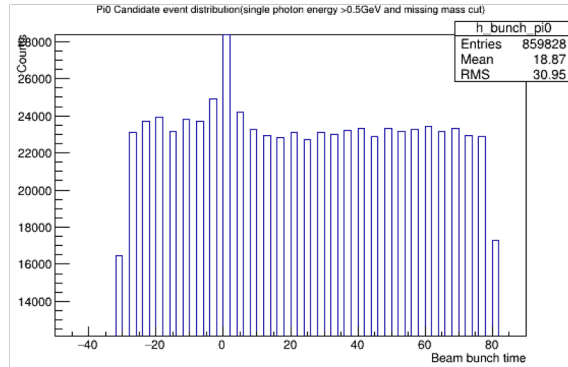


Figure 6-2: The distribution of π^0 number in different beam bunch, in which the coincident peak is out of the plot range. Each histogram bar is a bunch, and the time here is bunch's central time.

arrives randomly. If we find the time difference of two photon event is larger than some level, we have more confidence that the two photons arrive in accidental coincidence.

As seen in the left of Fig.6-3, the time distribution of single photon follows Gauss distribution, and right of Fig.6-3 shows the absolute time difference between two photons events with invariant mass cut. Only a few candidate π^0 's' time difference is larger than 2 ns, which is acceptable in consideration of 0.7 ns time resolution of calorimeter. And this cut will discard real π^0 s, which can't be compensated by simulation. Since this cut will loss some real π^0 s, and the coincidence photons, regarded as background, could be subtracted by fitting, this time difference cut is NOT applied in analysis.

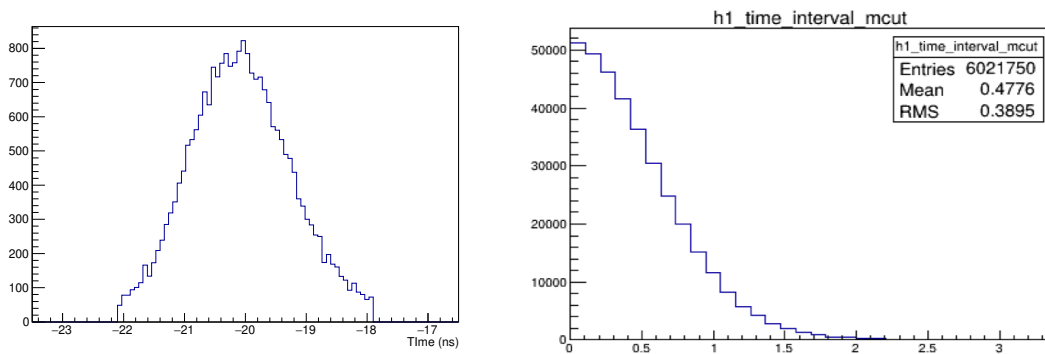


Figure 6-3: Left: the photon time distribution in a single bunch. Right: absolute time difference distribution between two photons. (unit in x axis is ns)

6.2.5 ϕ angle cut on π^0

The ϕ angle is defined as the angle around the beam line, the cut is influenced by the geometry restriction. The cut on ϕ angle discards the events on the detector edge, which should not affect the cross section result, and could be evaluated and compensated by simulation. Fig.6-4 shows the π^0 acceptance as a function of θ and ϕ angle. For the θ angle in the central of θ , the ϕ cut is set to ± 15 degree, and for the theta angle on edge, the cut is set to ± 10 degree.

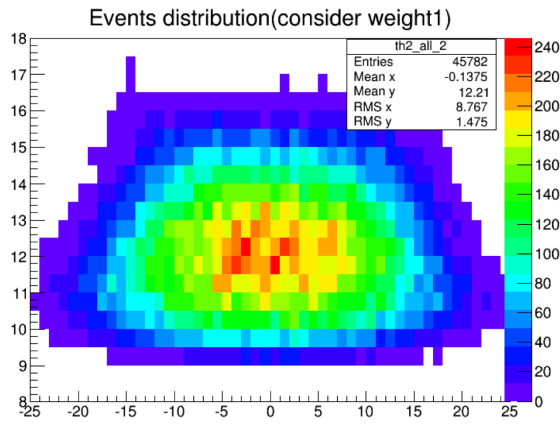


Figure 6-4: A brief detector acceptance view as 2D function of θ and ϕ .

6.2.6 π^0 cut

The kinematic range of π^0 is restricted by the geometry of calorimeter detector. Each DVCS setting has a different kinematic coverage, Table 6-3 shows the coverage for all three settings. The actual kinematic coverage of detector is a little larger than the range in table, because the statistics of π^0 s on the edge of the coverage is rare, and make it hard to get a good fitting and extract signal from background. With enough statistics in the central kinematic range, we set a fine kinematic bin that $0.5 \text{ GeV} * 0.5 \text{ degree}$ to evaluate the cross section trend as the function of energy and θ angle.

Configuration	Variable	Start value	Interval	End value	N bins
K8_1	Energy(GeV)	1.5	0.5	6.5	10
	θ (degree)	11.5	0.5	21.5	20
K8_2	Energy(GeV)	2	0.5	7	10
	θ (degree)	9	0.5	16.5	15
K11	Energy(GeV)	2	0.5	9	14
	θ (degree)	7	0.5	15	16

Table 6-3: The π^0 kinematic coverage of the settings.

6.3 Charge calculation

The integrated charge is an important factor in cross section calculation, and the error of which influences the result directly. The calculation of average current in each event is described in Sect.4.5.5.1. For the stable beam current event, each bunch has same current that equal to the average current. Since the current of each event is known, the integrated charge Q could be calculated as the current multiply the time window of each event:

$$Q = \sum^{N_{events}} (I_{event} \times 24 \times 4ns) \quad (6-1)$$

where I_{events} is the current of each event, 24 is the number of bunches after bunch selection. The integrated charge for all three normal run settings and one dummy run setting are shown in Table 6-4.

kinematic setting	Expected beam current	Total valid events	Total charge(10^{-5} pC)
K8_1	10 or 15 μ A	14.7M	1.90
K8_2	10 or 15 μ A	11.6M	1.69
K11	15 μ A	11.9M	1.71
K8_1(dummy)	15 μ A	73k	0.0104

Table 6-4: The total charge for configurations used in analysis. The expected current in normal run is 10 or 15 μ A, and the real current may differ a bit.

6.4 Simulation

As we described in generator section, the modified Hall D generator is probably not correct, and one of our purpose is to correct it. In simulation, this π^0 cross section acquired from generator is only used as a reference cross section value, and the simulation will get the π^0 yield from this reference value. Once the the π^0 yield in data is extracted, comparing it to the simulation yield, the ratio of these two values is equal to the cross section ratio. So this wrong cross section result will not influence the final cross section result, and we focus more on how the generator works in simulation.

Since the generator only could simulate one target type at a time, the target is divided to three parts in simulation process: upstream Aluminum window, liquid hydrogen target and the downstream Aluminum window

6.4.1 Generator description

The modified Hall D generator is used to create the raw π^0 events from ep scattering, and the generator itself only works for proton target. The generator mainly focus on the generation of electron, photon, proton, neutron, and other main mesons, and contains both mother particles from secondary reacting and the final state particles. The output of generator includes the 4-momentum of all particles it generated and also the vertex in target, which follows a vertex distribution.

To run the generator, the beam energy, current, target information are needed to be specified. Since the electron is regarded to generate radiated photon firstly in generator, and then react with target, to cut off the low energy radiated photon, the energy cut of radiated photon is set to 0.2 GeV, which is much lower than the minimum energy of π^0 that could be detected in calorimeter. For the simulation of LH_2 target part, to contain the radiation influence of upstream window, a radiator is added before electron pass through the simulating target. The radiator embody the radiation effect of all the matter in front of the target, which not create other particles but only the radiation photons that could interact with the target in simulation. The radiator is added in the simulation of LH_2 target and downstream window.

Then the generated particle could be applied directly to the detector simulation. We select all the generated π^0 s, and take them as input into the detector simulation.

6.4.2 Vertex distribution along target (Z dependence)

For a long target system, vertex information of particle is necessary and important. Since we don't know the vertex of inclusive π^0 that is not related to the trigger electron, we need the assistance of simulation to evaluate the vertex distribution of π^0 , and help us reconstruct the photon and π^0 .

The vertex distribution is not uniform along the target direction, actually because of the photons from radiation, the downstream target will generate more particles. The electron beam hit the target will lose a tiny fraction (0.02%, from simulation), which could be ignored, meanwhile, more photon stream are created and then react with the target, generated more other secondary particles at downstream.

As described in generator section 2.2.3, the particles generated from ep interaction in generator are originated from two parts, the main part is the interaction through virtual photon with the nucleon, the second part is from real bremsstrahlung photon interacts with nucleons, in which the bremsstrahlung photon flux is dependent on the radiator thickness the beam has passed through. The loss of electron in beam could be ignored, The vertex distribution of first part is uniform, and the second part will be a linear function related to the radiator thickness.

Fig.6-5 shows the vertex distribution of π^0 in 15 cm LH_2 target acquired from generator. This trend is fitted by a linear function:

$$f(z) = 1.375 + 0.05z \quad (-7.5 \text{ cm} < z < 7.5 \text{ cm}) \quad (6-2)$$

where z is the vertex in target, and the function here is not normalized as probability density distribution function. Transfer the unit cm to the relative radiation length X , which is equal to $\rho d/X_0$, it will be:

$$f(X) = 1.375 + 44.4X \quad (6-3)$$

Since this distribution is acquired based on the generator model that we need to confirm, to adjust the distribution trend, we introduce a slope parameter Par to tune the influence of bremsstrahlung part:

$$f(X) = 1.375 + 44.4X \cdot Par \quad (6-4)$$

where for the generator result $Par=1$.

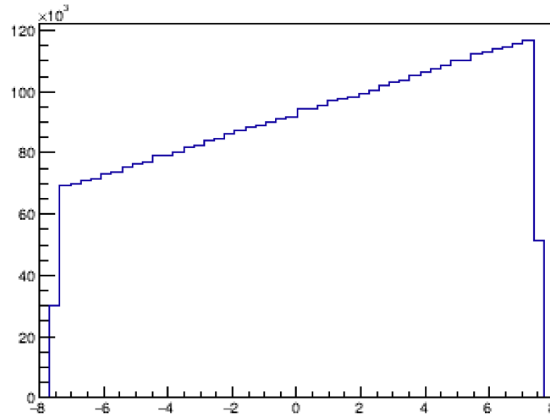


Figure 6-5: The vertex distribution of π^0 in 15 cm LH_2 target from generator, unit in X axis is cm.

6.4.3 Target window simulation

The π^0 s that generated from aluminum target window is simulated separately, and then add to the total π^0 s events count with the hydrogen target events. The generator is adapted from proton target to the Aluminum target with neutron based on the isospin assumption theory, which lead to another error in simulation.

Since the thickness of dummy target is very thin compared the the total target length, the dummy target is regard just as two layers along Z direction. Even so, it still follow the vertex distribution. Although the thickness of target window is very thin, as shown in Table 6-5, the density the Aluminum is 40 times larger than the liquid hydrogen and the influence would be still significant.

The weight calculation for different target type is shown in Table 6-5. The weight is separated to two parts: EPA and Bremsstrahlung part. The EPA part is calculated through $d \cdot \rho$, which is uniform distribution along the beam direction, and we set the π^0 yield of EPA in LH_2 target is equal to 1. The Bremsstrahlung part is related to the average radiation length. The average Brem photon is equal to $44.4 \cdot X$, and π^0 yield of Bremsstrahlung is equal to the photon yield multiply the nucleon number ($d \cdot \rho$) in target. The sum of these two weight is the total target weight. The ratio r_{window} of target window weight to the total target weight is:

$$r_{window} = \frac{0.073 + 0.0354 * par}{1.073 + 0.4784 * Par} \quad (6-5)$$

The ratio is about 0.07, even for a varying Par value, which shows a significant

influence of target window on the total target.

Target type	Upstream window	LH_2 target	Downstream window
Material	Aluminum	Liquid Hydrogen	Aluminum
Thickness d(cm)	0.0127	15	0.01524
Density $\rho(g/cm^3)$	2.81	0.071	2.81
Radiation length $X_0(g/cm^2)$	24.01	63.05	24.01
Relative $d*\rho$ (set $LH_2=1$)(EPA part)	0.033	1	0.040
Radiation length coverage	0~0.00148	0.00148~0.01848	0.01848~0.02026
Average radiation length	0.00074	0.00998	0.01937
Average Brem photon pass through (relative value)	0.032	0.443	0.86
π^0 yield from Brem photon beam	0.001	0.443	0.0344
Both two(EPA +Brem)	$0.033+0.001*Par$	$1+0.443*Par$	$0.40+0.0344*Par$

Table 6-5: Target weight description.

We also simulated the dummy target to compare with the data of dummy target run. For the dummy target simulation, the upstream window itself is regarded similarly as the downstream window in the real target showed in above. Since there is no liquid hydrogen in target, the radiator before downstream is only the upstream window.

6.4.4 Detector simulation process

The detector simulation will get the detected π^0 yield on calorimeter base on the all π^0 s generated in generator.

In the simulation process, π^0 decays into two photons instantly at its vertex in target. In the π^0 center of mass frame system, the decay is symmetric, and the two photons from decay have equal energy ($m_{\pi^0}/2$), and emitted back to back. Since the decay is symmetric, the distribution of angle θ_{dec} that between initial π^0 motion direction and the photon decay direction is uniform, which is set randomly in simulation. Then a Lorentz boost is applied to transfer the momentum of two photons to the laboratory frame. When the two photons are boosted to the laboratory frame, they will carry different energy and move to different direction. Fig.6-6 shows two different situations, and for the asymmetric decay, the low energy photon will not be detected.

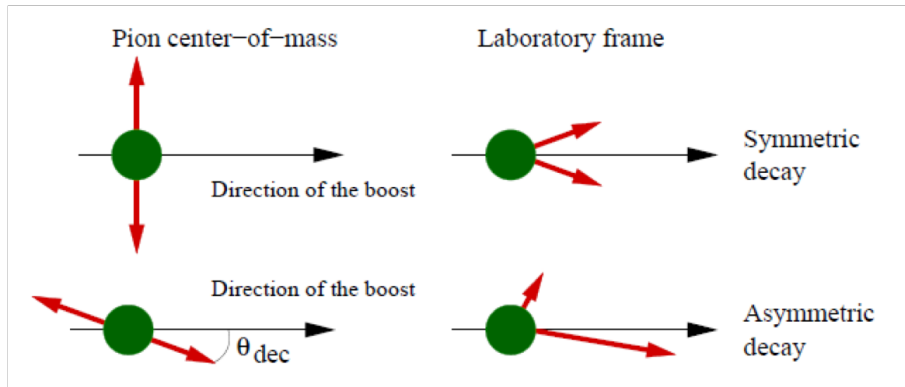


Figure 6-6: The decay of π^0 to two photons in two main situations. Top: a symmetric decay, two photons have similar energy and the energy of each photon in the laboratory frame is above the threshold. Bottom: an asymmetric decay, in which a dominant photon own most energy and the other one with low energy not pass the setting energy threshold (0.5 GeV).

The two photons are traced and checked if each one could hits on the calorimeter. A π^0 event is detected in simulation require both two photons detected in calorimeter. All the cuts performed in detector simulation is same as the cut in final data analysis. Only a small part of π^0 s could be detected, most will be detected by:

- The detector acceptance coverage of π^0 kinematic range is narrow.
- One of photon not reach the detector.
- One of photon not satisfy the energy cut.
- Not satisfy the other cut, such as hitting the edge of calorimeter.

The π^0 s that satisfy the these cuts will be kept and the event number is counted as initial π^0 yield from simulation.

6.4.5 π^0 yield from simulation

The simulation generated more π^0 particles than the events in the run data to minimum the statistic error of simulation, so the final π^0 yield result need to be normalized with charge.

To make the generator run efficiently, the generator only sample the interacted ep scattering events and ignore the null events, so all the generated events are comparable to the ep interaction rate. The interaction rate means how many electrons interact with proton in a second, and the value is returned from the generator calculation, shown in

Table 6-6.

Interaction rate	8.5 GeV(4 pass)	11 GeV(5 pass)	4 pass dummy target
Up_window	55124 kHz	58681 kHz	442378 kHz
LH_2	2141200 kHz	2268649 kHz	-
Down_window	106620 kHz	112625 kHz	442378(574180) kHz

Table 6-6: The reference interaction rate from generator calculation. The value in bracket of downstream dummy target window is taken the bremsstrahlung photon from upstream window into consideration.

The final π^0 events yield from simulation $N_{simu}^{\pi^0}$ that normalized to the charge will be:

$$N_{simu}^{\pi^0} = N_{simu_detected}^{\pi^0} \times \frac{rate}{N_{events_simulated}} \times time \quad (6-6)$$

where $N_{simu_detected}^{\pi^0}$ is the original yield, rate is the reference interaction rate from generator calculation, $N_{events_simulated}$ is all the simulated events from generator, shown in Table 6-7. The time is relative time that the integrated compared to the $15 \mu A$ current electron beam, as shown in table 6-8, and $15 \mu A$ is the value of input current in generator.

Simulated events	8.5 GeV(4 pass)	11 GeV(5 pass)	4 pass dummy target
Up_window	5 B	5 B	1 B
LH_2	22 B	20 B	-
Down_window	5 B	10 B	1 B

Table 6-7: The number of events simulated. B is short for billion.

Configuration	Relative time(s)
K8_1	1.193
K8_2	0.967
K11	1.144
K8_1(dummy)	0.00695

Table 6-8: The relative time that the integrated charge compared to the $15 \mu A$ electron beam current.

The target is divided to three parts, and each part is simulated separately, the total π^0 s generated from adapted Hall D generator is the sum:

$$N_{simulation} = N_{up_window} + N_{LH_2} + N_{down_window} \quad (6-7)$$

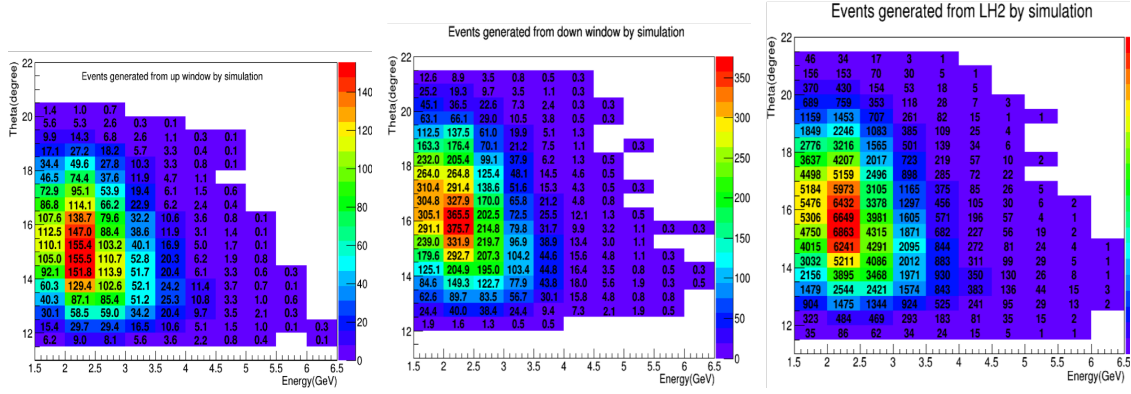


Figure 6-7: The number of π^0 from three separate target parts simulation of setting K8_1. Plots from left to right are: upstream window, downstream window and LH_2 .

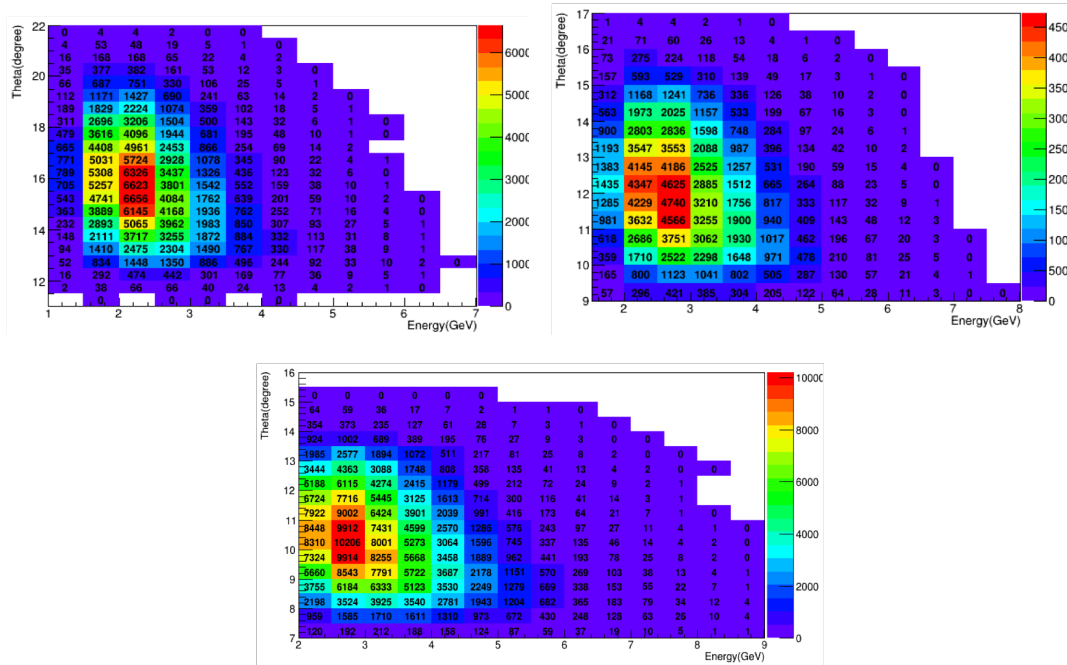


Figure 6-8: The normalized π^0 yield from simulation, which is the sum of three separate target parts. Top: K8_1 and K8_2. Bottom: K11.

6.5 Data analysis

The main purpose of data analysis is to extract π^0 number from different kinematic ranges firstly, and then compared these number yield to the simulation result. The π^0 events could be recognized by the invariant mass of two photons, in which the accidental

coincident background is included, and the events number could be extracted from the fitting.

Since we don't know the vertex of inclusive π^0 , the vertex assumption following vertex distribution is applied in the data analysis. And also the potential π^0 events in three-cluster is considered in the analysis.

6.5.1 Vertex assumption

π^0 s could be generated from any position in target along beam direction, including the target windows. Since the vertex of inclusive π^0 could not be reconstructed in any detector, just simply taking the target center as π^0 vertex will contribute a large error. To minimize the influence of the vertex uncertainty, we assume the π^0 particle is generated from any position in target and the probability following the vertex distribution shown in vertex distribution. The sum of each position with a weight contribute to the total vertex influence. The average invariant mass with vertex weight is described as:

$$m_{\pi^0} = \int_{-7.5cm}^{7.5cm} f(z)m_{\pi^0_{re}}(z)dz + W_{up}m_{\pi^0_{re}}(-7.5cm) + W_{down}m_{\pi^0_{re}}(7.5cm) \quad (6-8)$$

in which, $m_{\pi^0_{re}}(z)$ is the reconstructed invariant mass of vertex z , $f(z)$ is the vertex distribution of LH_2 target, W_{up} and W_{down} is the weight of up and down stream target window separately at vertex position $\mp 7.5cm$. The sum of $\int_{-7.5cm}^{7.5cm} f(z)dz$, W_{up} and W_{down} should be normalized to 1, and the normalized weight ratio is 0.0275, 0.9248, and 0.0477 separately with $\text{Par}=1$.

For the convenience of π^0 reconstruction and calculation, the target is divided into 17 parts, including 15 parts of LH_2 target, and 2 parts of target window. For each part, photons are reconstructed from cluster with vertex, and then the 4-momentum of π^0 is reconstructed by two photon events. So for each event, we reconstruct 17 π^0 s and each one has its weight.

6.5.2 Vertex weight

The $f(z)$ only describe the possibility that the π^0 generated from the vertex z following vertex distribution, besides, the vertex weight also need to include the influence of detector acceptance. In other words, the π^0 generated from the vertex that near the detector is detected more possibly than the far end. The acceptance $A(E, \theta, \phi, z)$ shows the

possibility that a π^0 could be detected in detector with the consideration of two photons decay process, defined as:

$$A(E, \theta, \phi, z) = \frac{N_{detected}^{\pi^0}}{N_{generated}^{\pi^0}} \quad (0 \leq A \leq 1) \quad (6-9)$$

The acceptance is related to the energy E , angle θ and ϕ , and vertex z of a π^0 . Its value is acquired from π^0 decay simulation as a function of specific E, θ, ϕ, z .

The acceptance correction factor $A(E, \theta, \phi, z)$ is added to achieve more accurate vertex weight. From the correction of the Eq.6-8, based on conditional probability calculation, we get average invariant mass with new vertex weight:

$$m_{\pi^0} = \frac{\int_{-7.5cm}^{7.5cm} f(z)m_{\pi^0_re}(z)A(E, \theta, \phi, z)dz + W_{up}m_{\pi^0_re}(-7.5cm)A(E, \theta, \phi, -7.5cm) + W_{down}m_{\pi^0_re}(7.5cm)A(E, \theta, \phi, 7.5cm)}{\int_{-7.5cm}^{7.5cm} f(z)A(E, \theta, \phi, z)dz + W_{up}A(E, \theta, \phi, -7.5cm) + W_{down}A(E, \theta, \phi, 7.5cm)} \quad (6-10)$$

in which, the denominator in equation is the sum of two weights product, and used to normalize the total weight equal to 1.

6.5.3 Extract π^0 events yield from fitting

The fitting method of invariant mass influence the π^0 yield directly, especially for the kinematic bins a high background level, and some bad fitting function even fail the fitting. The signal is fitted by Gauss function and the background is fitted by the ARGUS background shape distribution. The ARGUS distribution, named after the particle physics experiment ARGUS[62] is the probability distribution of the reconstructed invariant mass of a decayed particle candidate in continuum background. This fitting is performed by the fitting function RooArgusBG in RooFit[63][64], which is a RooAbsPdf implementation describing the ARGUS background shape. The general distribution of ARGUS function is:

$$Argus(m, m_0, c, p) = \mathcal{N} \cdot m \cdot \left[1 - \left(\frac{m}{m_0} \right)^2 \right]^p \cdot \exp \left[c \cdot \left(1 - \left(\frac{m}{m_0} \right)^2 \right) \right] \quad (6-11)$$

where m is the invariant mass for fitting, m_0 is the cut-off value, should be larger than m and the parameter c means the curvature.

The invariant mass is fitted well with the combination of Gauss and Argus function, especially for the high energy π^0 s, which has a better signal-background ratio. Fig.6-9 shows the fitting result of different energy range. However for the bins with very low energy π^0 that a little higher than detector acceptance, the accidental coincidence of two photons dominate the distribution, and the fitting is failed even the fitting parameter is

adjusted manually. Since these low energy bins are at the edge of π^0 kinematic coverage range and low statistics, these low energy bins are discarded in analysis, and the π^0 kinematic coverage is shown previously in Table 6-3.

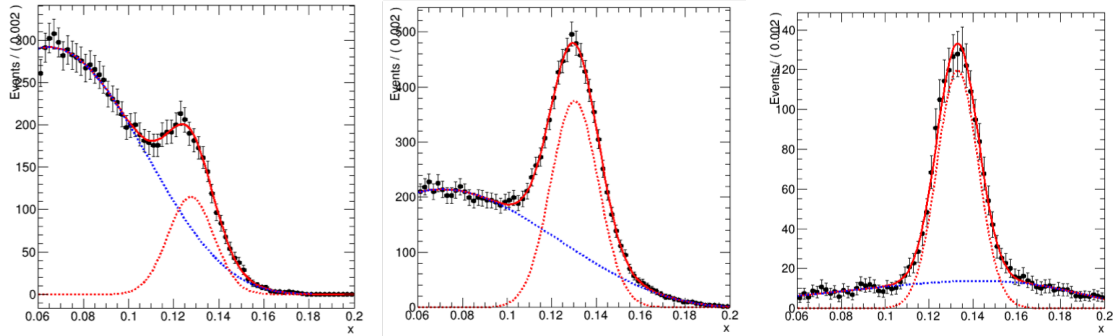


Figure 6-9: The fitting result sample of two clusters invariant mass (unit in GeV). Left: π^0 energy 1.5~2 GeV, accidental coincidence clusters dominate. Middle: 2~2.5 GeV. Right: 3~4 GeV, shows better signal-background ratio.

The statistics is necessary for a good fitting, and the fitting of each bin is performed only when the histogram contain more than 50 events including signal and background. The count of π^0 signal yield is acquired by the area of gauss fitting.

6.5.4 Extract π^0 s from three clusters events

Thanks to the clusters reconstruction algorithm, an event could reconstruct several clusters at the same time. Fig.6-10 shows the cluster number distribution in an event. Most π^0 s are extracted from two clusters distribution fitting, but there are also π^0 s existing in three cluster events, which means a π^0 add an accidental photon are detected at the same time. It's hard to distinguish the accidental photon form these three clusters, and it's also likely that all three photons appear accidentally. From Fig.6-10, the three clusters events only take up 6.5% events compared to two clusters events, because it has an additional cluster, the actual number of π^0 s exists in three clusters will be higher than this ratio, in which care need to be taken.

Any two clusters combination in three clusters event will be a candidate to reconstruct a π^0 , so every combination need to be considered. There are 3 two-clusters combination of three clusters, and apparently only one π^0 exists at most. We regard any

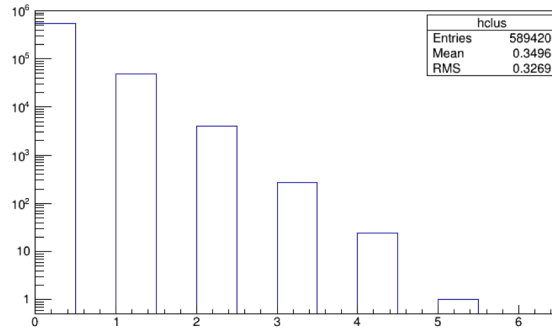


Figure 6-10: The clusters distribution in a bunch. As the number of clusters increased, the quantity of events decreased rapidly.

combination as a two cluster event similarly. Without bias, each combination has a $1/3$ weight treated as a π^0 for the analysis in the analysis.

Two methods are used to extract π^0 s from three clusters events. The first method mixes every combinations with the raw two cluster events, regard them as two cluster event and fill into invariant mass histogram with a $1/3$ weight. The final π^0 number is extracted from the whole fitting. The second method analyze the three cluster event separately in an additional step, to avoid the contamination of three clusters to the two cluster fitting. The invariant mass of two clusters event distribution is fitted firstly, extract the signal/all (signal + background) ratio $R(E, \theta, m)$ in each bin of invariant mass distribution histogram. Then the weight that the each combination considered as a π^0 will be $R(E, \theta, m) * 1/3$, and the sum of weight is counted as the additional π^0 number from three clusters events.

These two methods get very similar result, we prefer to use the first method because it could get the statistical error of both two and three clusters from fitting directly. The second method could evaluate the influence of three clusters events, compared to the two clusters event, an additional 10% number of π^0 is added from three clusters events, which significantly impact the final result.

There are also four and even five clusters events exist, as shown in Fig.6-10. We have no confidence for the reconstruction of too many clusters, which may cause from noise. The number of four clusters event is only take up 5% compared to three clusters, let alone to the five clusters. In consideration of an acceptable error, the events that have more than three clusters are ignored in the analysis, which lead to a less than 1% error to the final result.

6.5.5 $\pi^0 s$ yield in data

The number of $\pi^0 s$ extracted from data analysis is the sum from both two and three clusters events. Fig.6-11 shows the result of all three kinematic settings.

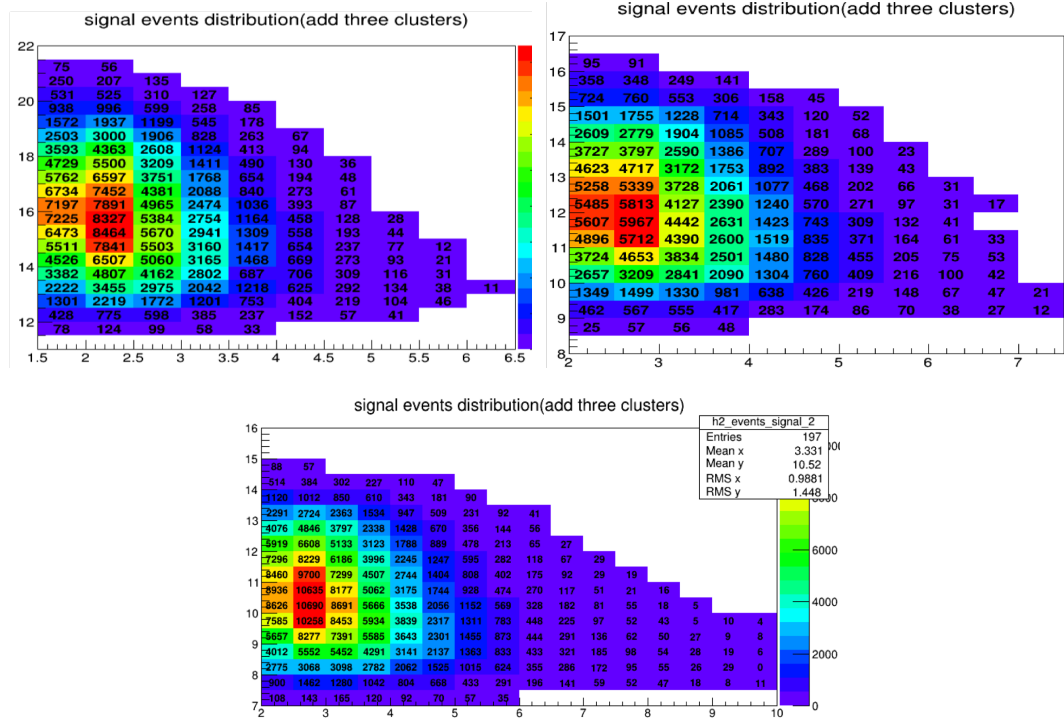


Figure 6-11: The π^0 yield result extracted from the data analysis. Top: K8_1 and K8_2. Bottom: K11.

6.5.6 Dummy target data

The dummy target data is also taken and the initial purpose is using it to remove the effect of target window through subtracting the dummy target run result directly. The dummy target that shown in Fig.3-5, has only the target window at the same position as real target window, and to increase the data taking rate, the thickness of single dummy target is about 7 times of the real target window.

There are several dummy target runs, and the total events in these runs are very limited when comparing to the hundreds of hours normal runs. For the kinematic setting of DVCS experiment applied for the π^0 analysis, only one dummy target run is taken, and

227k raw events are taken in this run, the number of which is not enough to evaluate the target window influence and subtracted directly. We do the same analysis as the normal run to extract the π^0 s number, and just get several hundreds π^0 s, and put them into a few bins. The rare π^0 number lead to a large statistics error. The π^0 number distribution can be seen in Fig.6-12.

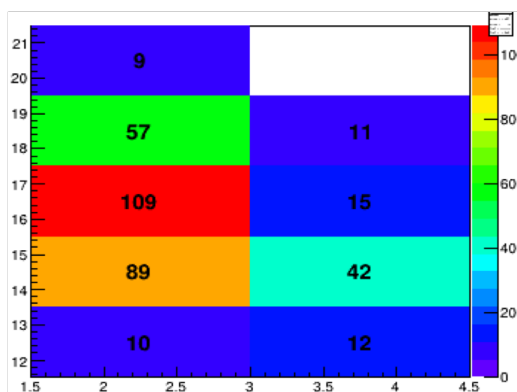


Figure 6-12: The number of π^0 extracted from the data of dummy target run.

The low statistics problem will lead to a large error, and the analysis of each bin need a delicate care. We compared this light yield to the dummy target simulation yield, and the result shows a similar trend as the ratio of data/simulation ratio of the LH_2 target data. For convenience, we assume the real dummy target cross section has the same ratio as LH_2 target compared to the generator cross section. So the dummy target data is not really used in analysis, and the influence of target window is evaluated from simulation.

6.6 Result

There are three kinematic configurations are used in the analysis, two configurations of 4-pass and one 5-pass configuration. The result from two 4-pass data must be consistent with each other, and could be used as cross check.

We get π^0 the event distribution from the data analysis. The cross section is the function of beam energy, energy and scattered angle of π^0 .

The other purpose is to check the inconsistency with the generator, especially the Hall D generator used at present, which is more reliable.

6.6.1 π^0 cross section result

The cross section of data is acquired by comparing data to the simulation result, this method is illustrated in Fig.6-13. Comparing the yield of data and simulation, we could get the π^0 yield ratio. Base on the good understanding of detector simulation and π^0 reconstruction in data, the arrows in simulation and data plot should have same response. So the the π^0 yield ratio is equivalent to the cross section ratio, and cross section of data is calculated through the cross section in generator. The final cross section result xS_{data} is calculated as:

$$xS_{data} = \frac{\pi^0 \text{ yield in data}}{\pi^0 \text{ yield in simulation}} \times xS_{generator} \quad (6-12)$$

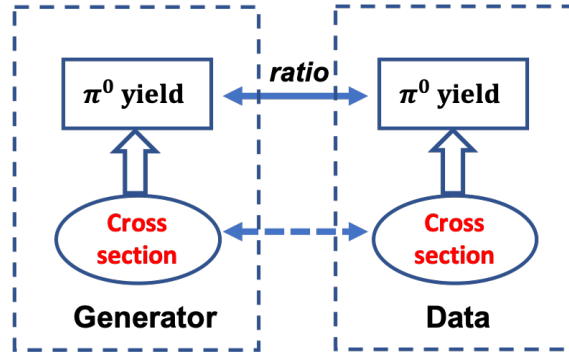


Figure 6-13: The illustration shows how to extract π^0 cross section from simulation.

Fig.6-14 shows the result of inclusive π^0 cross section and also compared with generator cross section. The result of most bins that shown in plots is larger than the cross section in generator. Fig.6-15 shows the same result as Fig.6-14, but in a 2D histogram.

The ratio that π^0 cross section of data compared to generator shows the deviation of the generator, and also could be used to correct the generator.

6.6.2 Comparison of two 4-pass results

There is an overlap kinematic range of the two 4-pass configurations. This overlap range could be used to compare these two individual analysis results, and acquire a general view of the result accuracy. These two results should match well with each other in ideal condition. As we can see from Fig.6-17, most bins match well that below 5% difference except some bins at the edge, which may be caused by the low statistics of one configuration or other issues.

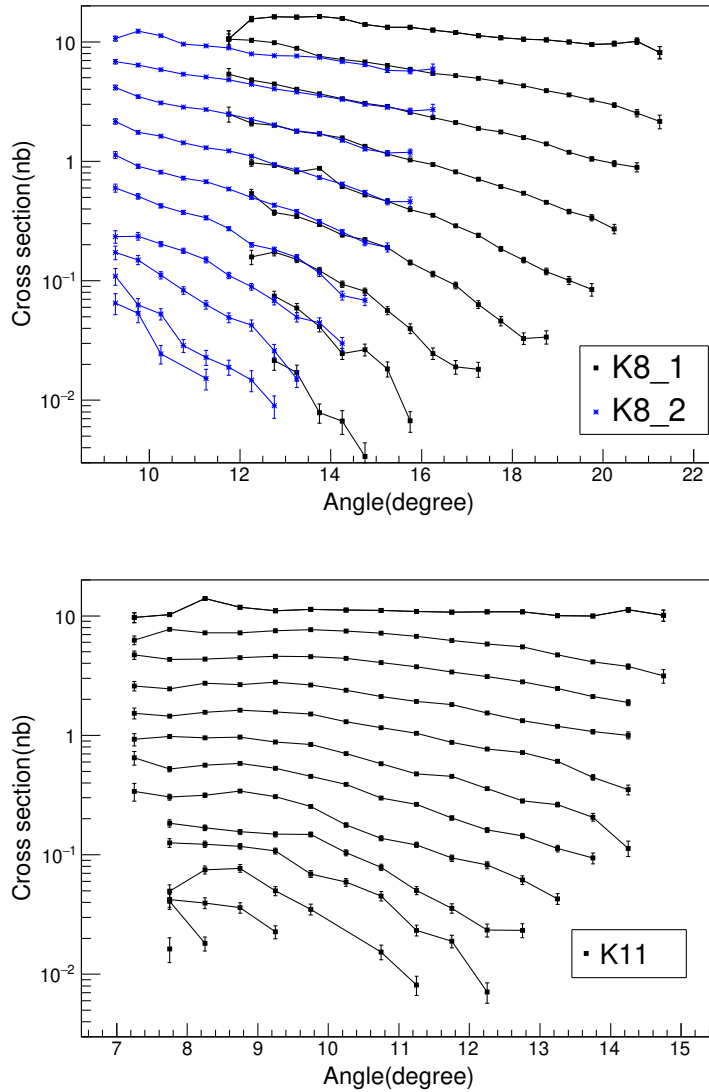
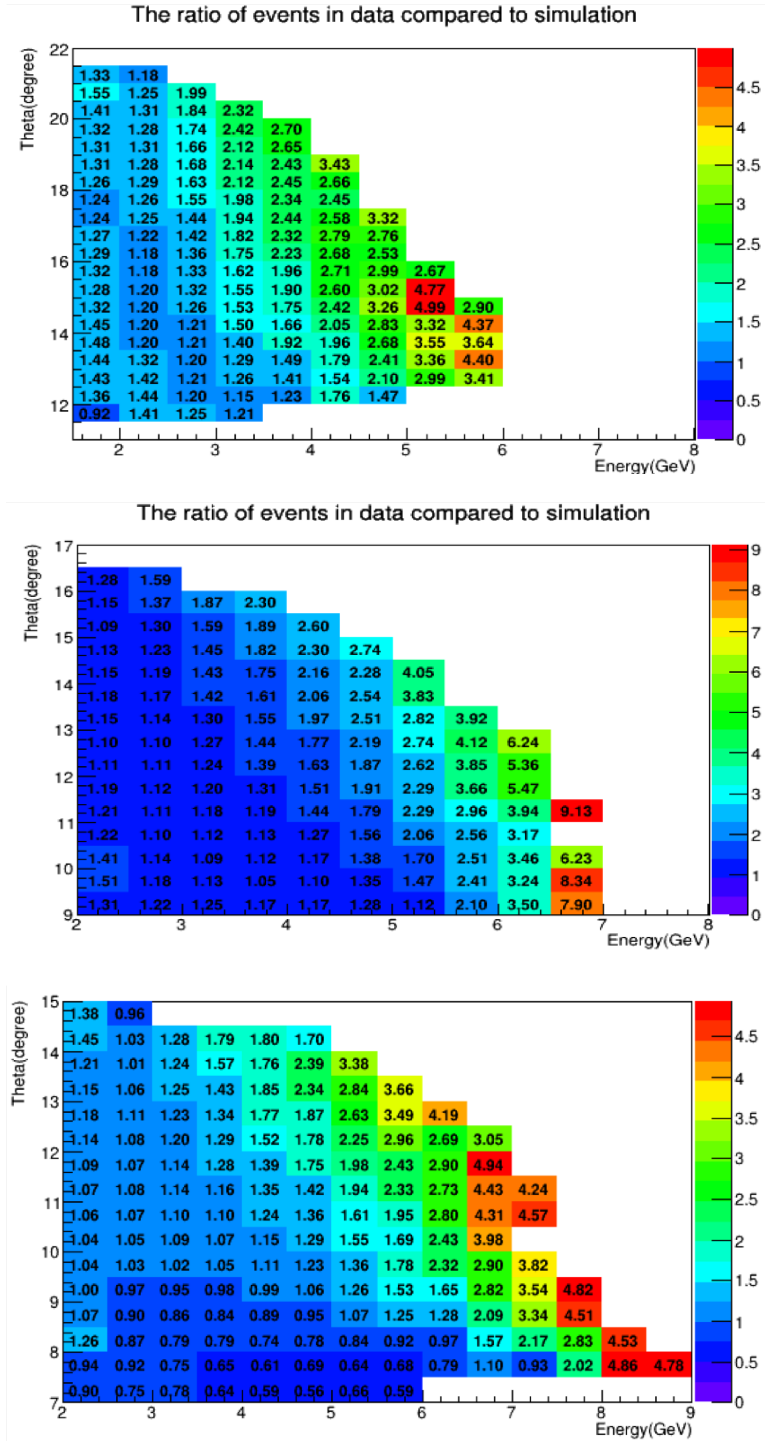


Figure 6-14: The final π^0 cross section result. Each line has the same π^0 energy, the lines from top to bottom present the increasing energy. Top: 4-pass(8.5 GeV) electron beam, include the result of both the two configurations. Bottom: 5-pass(11 GeV) electron beam result.

6.7 Error estimation

The error comes from two parts: statistical error and systematic uncertainty error. The error estimation result shows in this section with using the K8_1 result as a sample.



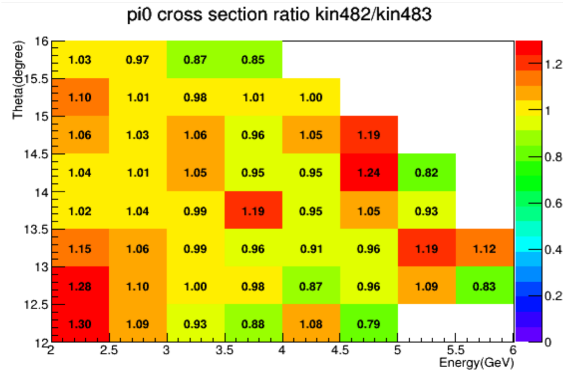


Figure 6-17: The comparison of the two 4-pass configurations in overlap kinematic range. The number in plot is the ratio of K8_1 cross section compared to K8_2.

6.7.1 Statistical error

A statistical error is the difference between the measured value and the true value, based on the number of events in measurement and all other background in fitting. For a Gauss distribution measurement without background, the statistical error is:

$$\sigma = \frac{1}{\sqrt{N}} \quad (6-13)$$

in which, N is the number of measured events. the background or the fitting will also influence the statistics of signal, and lead to an additional statistical error. So the final statistical error is always larger than σ . The statistical error is acquired from fitting, the statistical error of K11 is shown in Fig.6-18.

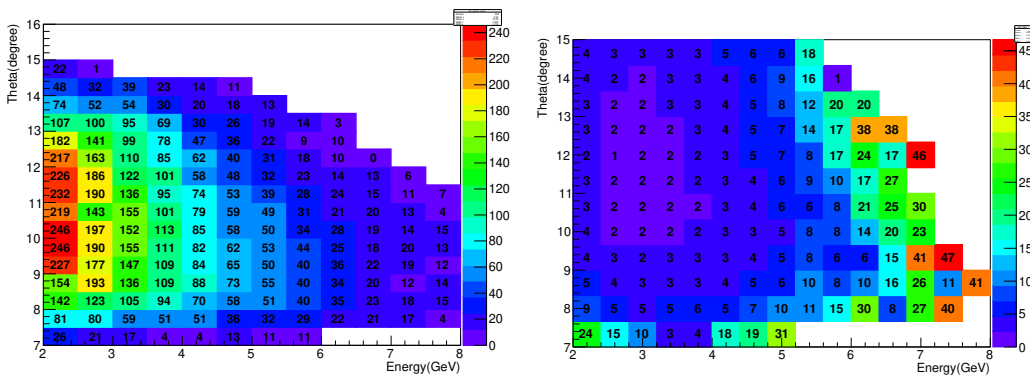


Figure 6-18: Left: the absolute statistical error from fitting. Right: the relative statistical error, the ratio($\times 100$) that the absolute statistical error shown in the left divided to the total π^0 events in data.

The π^0 s, of which the kinematic could hit the central area of calorimeter detector, have better statistics, instead the π^0 s with the kinematic in edge is hardly detected. Since we want get as more kinematic range as possible, for the less events bins on edge, if the fitting works well, we still keep the bins.

6.7.2 Systematic uncertainty error

The systematic error comes from four main dependent parts: beam, target, electron trigger in LHRS and π^0 detection in calorimeter.

The beam has two main property: charge and energy. Since the energy is a fixed value, so only charge is cared. The error in target focus on the target window influence and vertex distribution. The electron trigger cut is applied to select good trigger event, which should not influence the π^0 signal. After these event selection cuts, each error from electron trigger is less than 1%. The π^0 detection in calorimeter contribute to main error, which is emphasized in the following context.

6.7.2.1 Single photon energy cut

The single photon energy cut used for the analysis is 0.5 GeV, which is a balance between π^0 statistics and some low energy issues. If the energy calibration result is perfect, the cross section result should not related to this energy cut.

The energy cut is adjusted in both data analysis and simulation to check the influence to final result. As shown in Fig.6-19, result show a linear trend as a function of energy cut. As we mentioned before, the energy make a high contribution to the error, this bias may cause from some failure in energy calibration and the bad energy resolution.

6.7.2.2 Target vertex distribution error

The vertex distribution is acquired from simulation, which is mostly based on the theory model. The vertex distribution is a linear function of the thickness that particle passed through, and the linear coefficient Par may differ depend on different models, which is described in Eq.6-4. So it's necessary to consider the vertex distribution uncertainty, and take it into the error estimation.

The linear coefficient Par is adjusted to evaluate the error. We simulated two extreme situations: $Par=0$ and $Par=2$. $Par=0$ means the vertex distribution is uniform, and $Par=2$

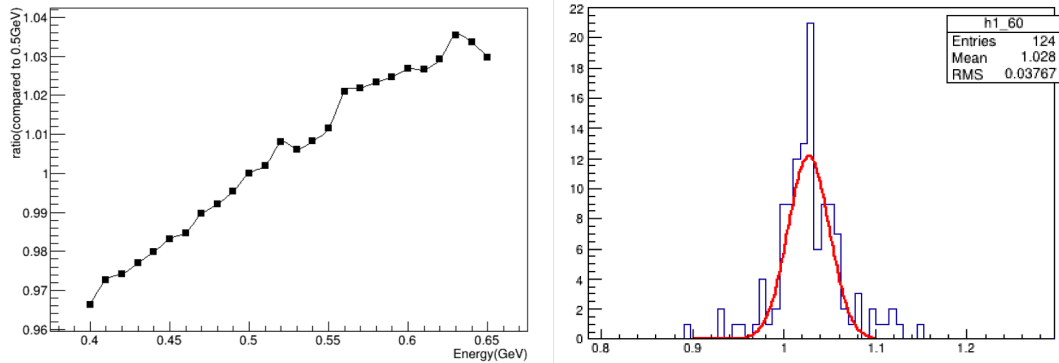


Figure 6-19: left: the relative cross section as a function of single photon energy cut. The ratio means each energy cut point is compared to the 0.5 GeV result as a reference. Each point is the mean value fitted by the ratio distribution of all kinematic bins that shown in right. Right: for 0.6 GeV photon energy cut, the cross section ratio distribution of every bin compared to the 0.5 GeV reference cross section.

means more π^0 is generated from the downstream. These two limit values are taken into both run data and simulation analysis, then compared with the normal result. We get the ratio of K8_1 configuration shown in Fig.6-20.

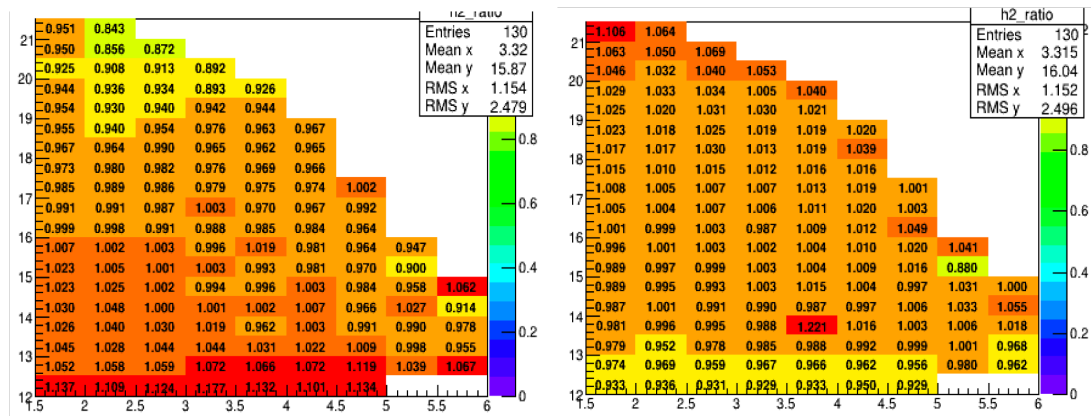


Figure 6-20: left: Assume the vertex distribution is uniform, the number is the cross section ratio compared to the Par=1 result. Results shows more π^0 particles are generated from small angle rather than the large angle. Right: cross section ratio for Par=2, and more π^0 particles are generated from large angle.

6.7.2.3 ϕ angle Cut

The normal ϕ angle cut is set to ± 15 degree to reject the pion of which the photons detected at the edge of detector. Most reconstructed π^0 has small ϕ angle, and the cut only abandon a small part of π^0 events. The effect of cut could be compensated by simulation, and should not influence the final cross section result.

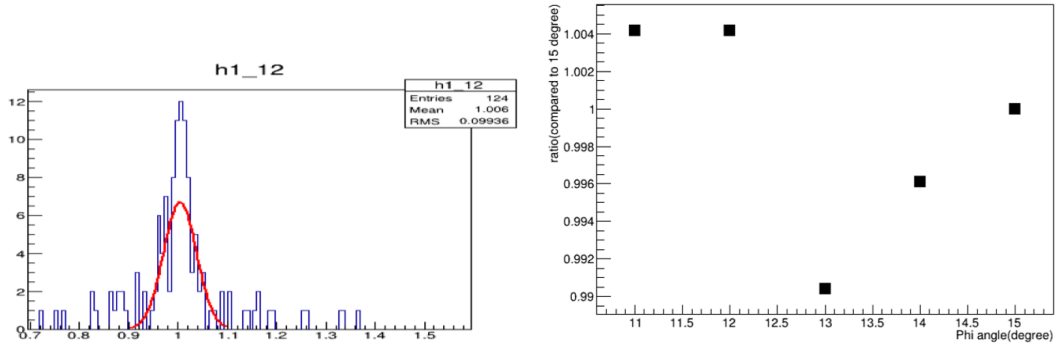


Figure 6-21: Left: the ratio distribution of 12 degree ϕ cut compared to the 15 degree cut. Bottom: the relative ratio of the cross section as a function of ϕ cut.

6.7.2.4 Calorimeter detector area cut

The error of calorimeter detector area cut reflects the position reconstruction resolution. We changed the calorimeter detector area cut From $x(-21, 12)$, $y(-21, 21)$ to $x(-18, 9)$, $y(-18, 18)$, which is reduced to the 70% of default area in analysis. Result shows in Fig.6-22.

6.7.2.5 Error of π^0 number in three clusters events

The number of candidate π^0 in three clusters events contribute to 10% of total π^0 events. As described in Sect.6.5.4, two methods are applied, and get similar result. The error is evaluated by the comparison of these two methods.

6.7.2.6 The summary of error

Form the error estimation shown in above, the largest error comes from the bad energy resolution and vertex uncertainty, which is reflected through energy cut and the vertex distribution assumption. The energy error is about 4%, and the vertex distribution

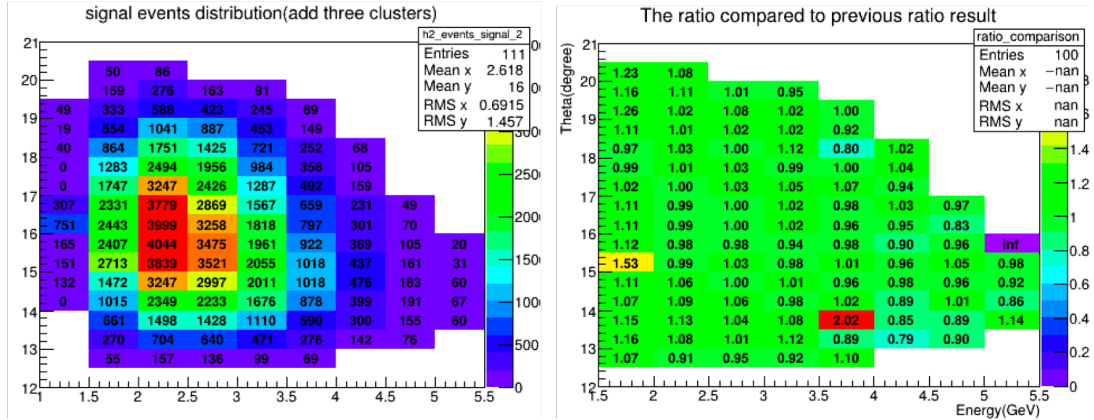


Figure 6-22: Left: the number of π^0 s with a narrower calorimeter area cut. Right: the cross section ratio of the narrower area cut compared to the original area cut.

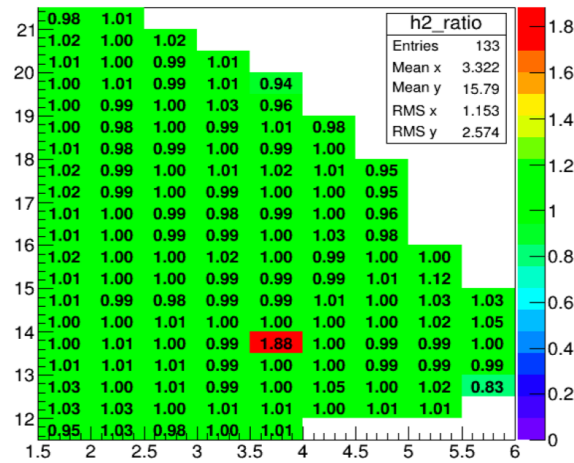


Figure 6-23: The cross section comparison ratio of two methods that extracting π^0 events from three-cluster events.

error is dependent on the θ angle, which we give a global 2% error. The preliminary general systematic error is listed in Table 6-9.

The 5.5% global error is good enough for the inclusive π^0 analysis purpose, and the kinematic bins that at the center of detector acceptance is much better than this result. However the kinematic bins on the detector acceptance edge have worse error, and the error need to present in each bins.

Systematic uncertainty	Value(%)
Charge[65]	<1
Photon energy *	4
Vertex distribution *	2
Calorimeter geometry * (related to position resolution)	2
Beam bunch uniformity	1~1.5
Target window impact	1
Phi cut	<1
Fitting error	<1
Three clusters	<1
Total	5.5

Table 6-9: Summary of systematic uncertainty. These are the global systematic value, the items with mark * will be carefully evaluated in each kinematic bins.

6.8 Summary and discussion

With all the effort described in above of this thesis, we successfully extract the inclusive π^0 cross section from the experiment E12-06-114 data with 8.5 GeV and 11 GeV beam energy. The success of this analysis based on these essential work: the method to find inclusive π^0 events, the good time correction and energy calibration, and the dedicate π^0 events reconstruction.

Even if the data have some restrictions, we still get a global 5.5% systematic error, which is acceptable for the analysis purpose, and more detailed error estimation will be performed later. The consistency of two 4-pass comparison result also verifies the measurement accuracy.

Comparing the cross section result to the cross section in modified Hall D generator, the ratio is about 1~1.5 for low energy π^0 , and for high energy and large θ , the ratio is get larger, which shows a significant increasing trend in comparison. Considering the cross section of low energy π^0 is several orders of magnitude larger than the high energy, this large high energy ratio will not significant influence the previous trigger rate result, so the trigger rate influence should focus more on the cross section change of the low energy

π^0 s.

The result shows the whole target's cross section, for the cross section of LH_2 target itself, it needs another work to subtract the effect of dummy target through simulation, which is not included in this thesis work now.

Chapter 7

The SoLID spectrometer and Electromagnetic Calorimeter

As described Chapter 2, the SoLID project will build a device in JLab Hall A to fully exploit the capabilities of the 12 GeV upgrade, and to handle very high luminosity in a large acceptance. The hardware work of SoLID project not only includes the design and construction of detectors, but also includes all other equipments used in experiment, such as target, magnet, and DAQ system. It's a general detector package that will be used for several already approved experiments in JLab, and also new experiments that have the potential possibility to join the project in the future.

To makes the data taking efficiently, the spectrometer has a full 2π acceptance, and runs under very high luminosity, both will lead to a very high trigger rate. In consideration of this high rate, the performance of detectors that work under normal conditions tend to perform worse, such as position resolution and particle rejection efficiency. The process of improving detector design is mostly focus on the high rate challenge.

7.1 General description of SoLID detectors

There are two configurations: Semi-Inclusive Deep Inelastic Scattering (SIDIS) configuration or Parity-Violating Deep Inelastic Scattering (PVDIS) configuration. Each configuration is designed for its physics purpose and most detectors are reused in both con-

figurations. The main difference is SIDIS configuration need to detect both electron and leading pion, and PVDIS only detect electron but works under very high luminosity. More detail about the two configurations will be described in the following.

7.1.1 SIDIS configuration

The semi-inclusive deep-inelastic scattering(SIDIS) experiments, such as the E12-10-006[23] experiment that measures the single/double spin asymmetry with the channel ($e, e'\pi^\pm$), will detect the scattered electron and an leading pion. As seen in Fig.7-1, the layout of configuration has two parts: the forward-angle(FA) detectors and the large-angle(LA) detectors.

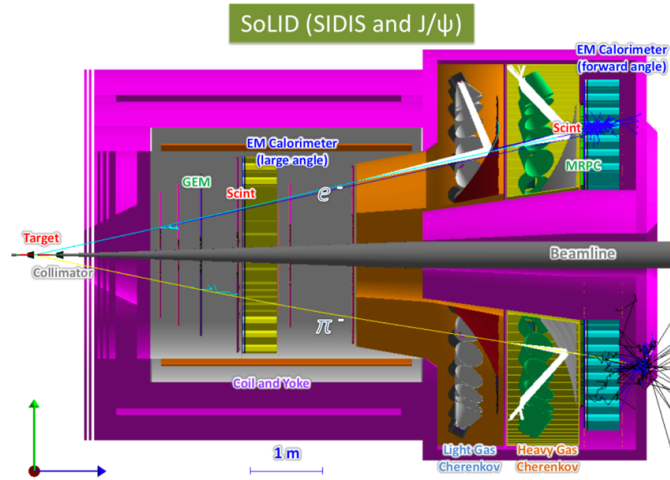


Figure 7-1: The layout of detectors in SIDIS configuration. The left part in picture works in the magnetic field of a solenoidal magnet, and yoke is applied to restrict the magnetic field in forward angle location. Electron beam hit the target from left side, then scattered electron could be discriminated and detected by both large-angle and forward-angle detectors based on the experiment purpose. Pions are only detected and distinguished in forward-angle detectors.

The forward angle detectors, with the polar angular coverage from 8° to 14.8° , could detect both charged pions and electrons. As seen in the Fig.7-1, 5 layers of GEM detector inside the magnetic field offer the tracking and momentum information of charged particle, and 3 of which are also used for the particle in large angle detectors. Light gas Cherenkov detector filled with CO_2 could separate electrons from pions. The heavy

gas Cherenkov located after the light gas Cherenkov can distinguish kaons and protons from pions. A Shashlik style forward-angle Electromagnetic Calorimeter(FAEC) is designed for electron and pion separation. A layer of forward-angle scintillator pad detector(FASPD) is placed before FAEC to reject low energy photon and reduce trigger rate. One layer of Multi-Gap Resistive Plate Chamber (MRPC) that has very good time resolution is placed near SPD to supply time information and additional particle identification.

For the large angle detectors, which covers the polar angle from 15.7° to 24° , is used to detect the large scattered angle electrons. Besides the GEM used as tracking, only other two detectors are included: large-angle scintillator pad detector(LASPD) and large-angle Electromagnetic Calorimeter(LAEC). The LASPD is thicker than FASPD, placed before the LAEC, provides time information and also used for the photon rejection. The calorimeter used in LAEC is same as the FAEC.

The experiments need very clear particle identification, all of detectors work together to achieve this purpose. For large angle spectrometer, we care mostly on the electron/photon separation, which could be separated from the co-work of tracking and LASPD. For the forward angle particle identification (PID), situation would be a little more complex. Small angle means more background and more kinds of particles: electron, photon, pion, kaon and proton. As the PID requirement, electrons and pions must be separated from others with a very high level ratio. To finish this task, it needs the co-work of all detectors, which means although one detector has low separation level, the combination of others will achieve the high separation level goal.

7.1.2 PVDIS configuration

The Parity-Violating Deep Inelastic Scattering(PVDIS) experiments, such as the experiment E12-10-007[26] measures the parity violating asymmetries(A_{PV}) with the channel $p(\vec{e}, e')X$, only detects the scattered electron. The layout of detector is shown in Fig.7-2.

This configuration only have the "forward-angle" part compared to SIDIS configuration. As seen in the Fig.7-2, a new device called "baffle" is added to reject background especially the photons, the other detectors are same as the SIDIS configuration and are reused. The polar angle coverage is from 22° to 35° . Electrons pass through two groups of GEM that offer tracking, and the PID is offered by the light gas Cherenkov and Elec-

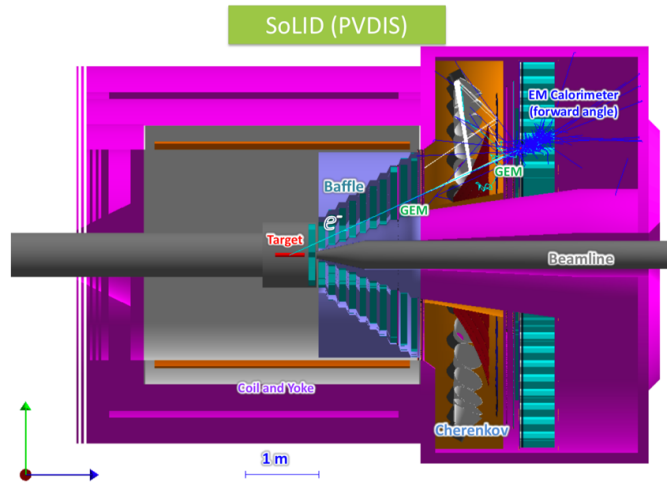


Figure 7-2: The layout of PVDIS configuration, only electron is detected. The target is placed at the center of coil. An electron that passed through baffle would be detected and recognized by GEM, light gas Cherenkov and EM Calorimeter.

tromagnetic Calorimeter(EMCal).

Although the structure of spectrometer is simple, the difficulty is much higher than it seems. The main challenge of this configuration is to deal with very high luminosity that is larger than $5 \times 10^{38} \text{ Ncm}^{-2}\text{s}^{-1}$ to reach a low relative statistical uncertainty, and this high luminosity requires a good radiation hardness. A special designed baffle that made of lead is used to suppress the mistaken photon trigger. The baffle system has 11 layers, each layer is staggered a few angle, and the whole system is divided into 30 independent sectors in the azimuthal angle, the beam direction view of baffle is shown in Fig.7-3. The photons are blocked by the baffle, only the electrons with bending specific angle in magnetic field could pass through. However, it also discards a part of electrons.

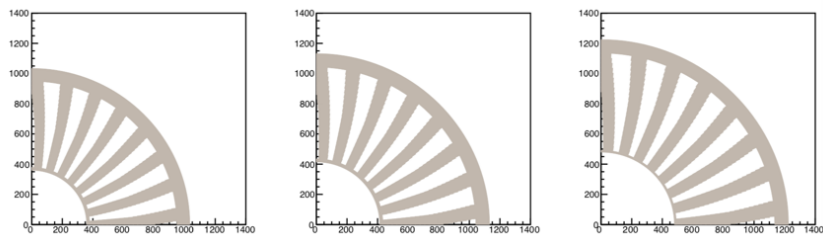


Figure 7-3: Three layers of baffles viewed along the beam line direction, only one quarter of each layer shows in the figure. Each layer rotate a bit angle, and electron could pass through the gaps. The unit of x and y axis in plot is mm.

7.1.3 SoLID spectrometer function and requirement

Here is the brief summary of detector/equipment requirement for the SoLID project. The high design requirement of SoLID experiment is satisfied by the cooperation of all these detectors/equipments.

- Magnet. The original magnet is 3 meter in outer diameter and 3 meter in length, it equips with additional coil and yoke. Max magnetic field strength is 1.5 tesla.
Function: Curve the trajectory of charged particle, distinguish charged particle from the particle without charge, help to offer the momentum of charged particle form tracking in GEM.
- GEM tracking Chambers. Good tracking efficiency(>90%) and position resolution(0.1mm), works especially efficiently in high rate environment compared to other tracking detectors.
Function: used for tracking, and acquire accurate momentum information by tracking.
- EM Calorimeter. Shashlik style sampling calorimeter. Include two longitudinally separated parts: pre-shower and shower detector. Require good energy resolution and radiation hardness. Since most content of this thesis focus on it, more detailed information will be described in the next sector.
Function: offer particle identification and decide trigger.
- Light Gas Cherenkov. Filled with CO₂, larger than 10 photo-electrons per electron from ionization. Electron efficiency larger than 90%, and better than 500:1 electron/pion separation(3.2 GeV ~ 4 GeV).
Function: Most efficient detector for electron/pion separation; decide the trigger.
- Heavy Gas Cherenkov. 1 meter long 1.5-atm C₄F₈O/C₄F₁₀ gas. Better than 90% pion detection efficiency, and kaon suppression greater than 10:1(2.5 ~ 7 GeV).
Function: most efficient detector for pion/kaon separation.
- Scintillator Pad Detector(SPD). The SPD is a layer of scintillator detector, includes Large-angle(LA) SPD and Forward angle(FA) SPD.
Function: low energy photon rejection and get time information.
- Baffles. Lead blocks have eleven layers and 30 sectors in each layer.
Function: To block low energy particle, photon and hadron background to an acceptable trigger rate.

- MRPC. It's an enhanced requirement for additional PID. The baseline time resolution requirement of MRPC is 100 ps, which could achieve pion identification from TOF information. More enhanced challenge is 30 ps time resolution, which could achieve kaon identification base on TOF information.

Function: offer accurate time information to achieve good TOF time resolution, used for pion/kaon identification.

7.2 SoLID ECal

The ECal detector is one of main detectors in SoLID, will be used in both configurations. The main function of ECal in SoLID project is measuring the deposited energy of particle, offering PID and deciding the final electron trigger. The challenge of detector design not only includes the performance requirement but also the assembly and signal readout. The cost of the Ecal takes up a large proportion to the total budget, to save the cost, the design must be studied carefully. The ECal coverage of both configurations is shown in table7-1.

	PVDIS FAEC	SIDIS FAEC	SIDIS LAEC
z(cm)	(320, 380)	(415, 475)	(-65, -5)
Polar angle(degrees)	(22, 35)	(7.5, 14.85)	(16.3, 24)
Azimuthal angle	Full coverage		
Radius(cm)	(110, 265)	(98, 230)	(83, 140)
Coverage area (m^2)	18.3	13.6	4.0

Table 7-1: Geometrical coverage for the SoLID electromagnetic calorimeters. The z direction is along the electron beam and the origin is at the solenoid center.

7.2.1 Desired performance and challenge

The ECal has its basic requirements similar as the other calorimeter, and it also has some special requirements that make the construction more challenging, which is shown in Table 7-2.

Here is the detailed description of the basic performance requirement:

Specification	Desired performance
Energy resolution	$< 10\% / \sqrt{E}(\text{GeV})$
π^-	50-100:1 for above Cherenkov threshold
e^- efficiency	$>95\%$
Position resolution	<1 cm
Radiation resistance	>400 kRad

Table 7-2: SoLID EC desired performance

- Energy resolution.** The energy resolution is the most important feature of calorimeter, and it decides how good the energy measurement is. For PID purpose, we need a less than $10\% / \sqrt{E}(\text{GeV})$ energy resolution, the value of which is much worse than the calorimeter used in other experiments. In fact, for the ECal used in SoLID, the main function is not measuring the energy, but to separate electron from pion, which means the requirement of energy resolution is not so strict. The energy of charge particle is measured by the radius of the bending tracking that is more accurate than ECal for low momentum particle. The other reason is that the radiation hardness requirement and budget restrict the choice of calorimeter material. The developing shashlik style sampling calorimeter that shows around $6\% / \sqrt{E}(\text{GeV})$ energy resolution, which satisfies the requirement.
- π^- rejection.** This is the most important feature for the SoLID ECal, which depends on the energy resolution. The electrons almost lose all its energy in calorimeter through electromagnetic cascade shower, and pions only lose a small part of energy through ionization. For the electron and pion with same energy, it could be distinguished from the deposit energy in calorimeter. An 100:1 rejection ratio need to be achieved for the calorimeter itself, and cooperating with other detectors will get a much more clean rejection.
- Electron efficiency.** The electron detection efficiency on ECal is $\sim 100\%$, this efficiency is the percentage that electron pass the pions rejection cut divided by all electrons, with the consideration of high background.
- Position resolution.** The calorimeter also could be used to reconstruct the hit position. When electron deposit energy on the calorimeter, it will form a shower that signal exists in several adjacent blocks. The hit position could be reconstructed by the position of each block with the signal amplitude weight. Apparently, the

smaller size of each block means the better position resolution. However smaller block size means more blocks, which will significantly increase the expenditure.

- Trigger decision. ECal decides the electron trigger combining with other detectors, which requires fast response time and background suppression.

There are also some special requirements for SoLID project:

- Radiation resistance. The PVDIS experiment runs at very high luminosity, the ECal must have good radiation resistance hardness, which is larger than 400 kRad. For normal crystal calorimeter, it can't resist so high radiation, and the property will become worse, such as the transparency, which lead to a worse light yield and energy resolution. The shashlik sampling calorimeter satisfy this requirement, and will be described later.
- Magnetic field. The ECal is exposed to the magnetic field, especially the large-angle ECal in SIDIS configuration, the maximum value of which reach 1.5 T. The ordinary PMT tube not works in this high magnetic field and other choice of SiPM is abandoned because additional cooling is needed to overcome the radiation damage. Our choice is using fiber to guide the light to the PMT outside the magnetic field.
- Rearrange convenience of two configurations. Since the two configurations share some same detectors, it's necessary to make it easy to re-arrange from one configuration to the other.

These special requirements make the design used in previous experiments not works in this situation, and we must develop the previous calorimeter design, figure out a new design to satisfy our requirement of ECal.

7.2.2 Shashlik ECal design

A shashlik style sampling calorimeter is designed and could satisfy the requirement of both configurations, in which lead is used as energy absorber, and plastic scintillator as the sensitive material to generate photon signal. As shown in Fig.7-4, the ECal is segmented longitudinally into two parts: preshower and shower detectors. The total radiation length of Ecal is $20 X_0$, including $2 X_0$ in preshower and $18 X_0$ in shower, which could achieve a less than 2% energy leakage of electron.

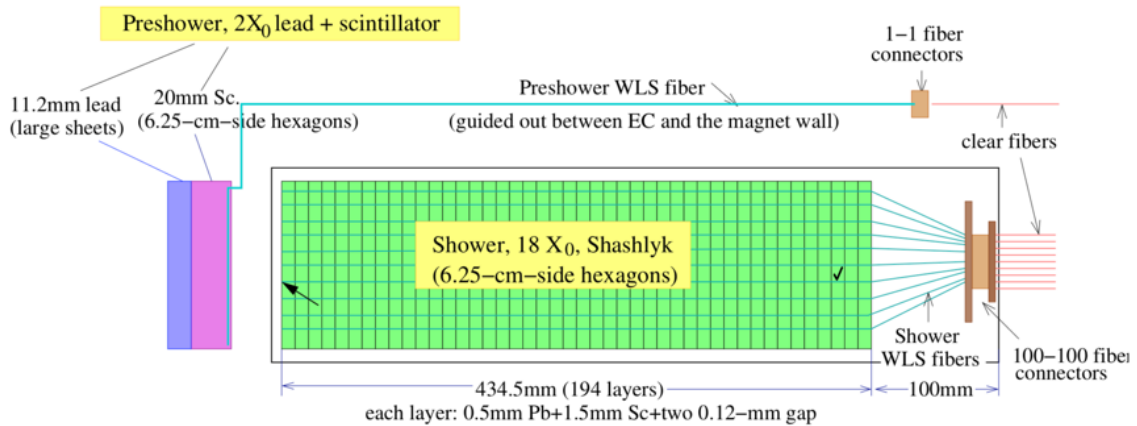


Figure 7-4: The sketch of Shashlik EC detector design. It is segmented to preshower and shower detectors longitudinally to enhance particle identification. The length of shower detector is about 44cm, contains 194 layers of alternating lead/scintillator plate and reflectors between lead and scintillator. Photons are collected through WLS fibers in both detectors, and are read out by PMT.

7.2.2.1 ECal longitudinal design

The preshower is a separate thicker layer of shashlik style detector, placed in front of shower detector to enhance the pion rejection, which can be seen in Fig. 7-4. It consists of a layer of lead with $2X_0$ and a 2 cm scintillator. The thickness selection is a balance between pion rejection and energy resolution, because the thicker lead decrease the energy resolution significantly.

The shower detector consists 194 layers, and each layer includes 0.5 mm thickness lead, 1.5 mm scintillator and two layers of reflectors(paper or others). 96 1mm diameter Wave-Length Shifting(WLS) fiber penetrate these plates through the holes, to guide the photon signal to the PMT for readout.

7.2.2.2 ECal transversal design

All the modules will be arranged as a ring, as shown in the Fig.7-5 a). The hexagon shape make the modules flexible to move and arrange. The area of each module is 100 cm^2 , and a total 1800 modules will be built to cover the large detector area. This choice of block size is optimized by simulation, which is a good balance between cost, position resolution and background suppression.

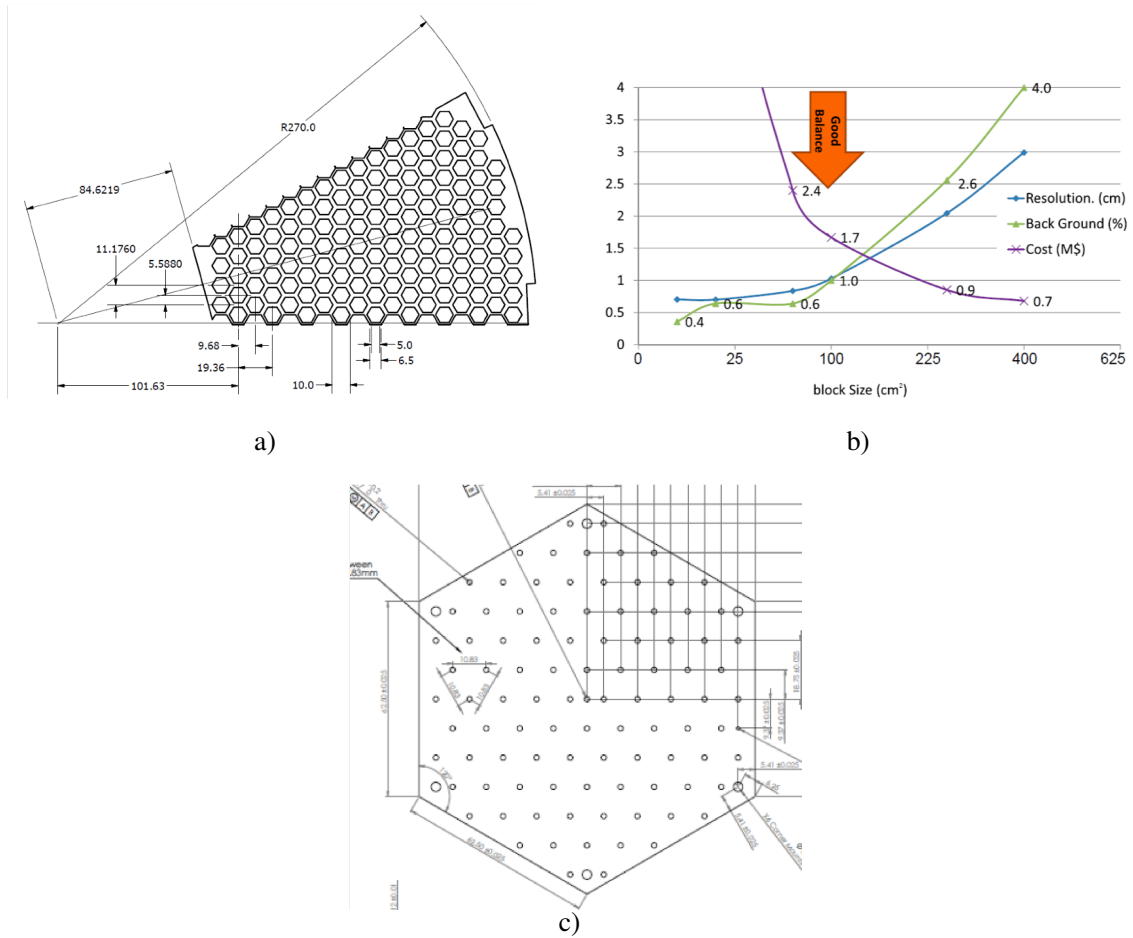


Figure 7-5: a) PVDIS FAEC(portion) viewing along the beam direction. b) Simulation result of position resolution, background and cost as the function of block size. Result shows a good balance at 100 cm^2 block size. c) Transversal sketch of a single module. 96 small holes for fibers penetrating and 6 large holes at corners for fixing rod.

7.2.2.3 Light guide out

As seen in Fig.7-4, the preshower detector has its own separated readout beside the shower detector. The picture of preshower is shown in Fig. 7-6, two WLS fibers(Y11) are embedded in the circular groove with several turns, and the whole preshower scintillator is wrapped by the Tyvek paper to enhance light yield. The photon collected in WLS fiber will be transferred to the long clear fiber by an end-to-end connector. Finally, the four fiber ends are coupled to one window of 16 anodes Multi-anode(MA) PMT for photon signal readout.

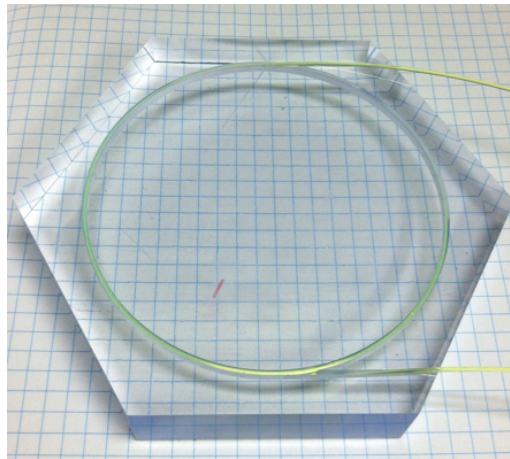


Figure 7-6: The picture of pre-shower detector with WLS fibers embedded in groove.

The photon signal of shower detector is collected by 96 the WLS fibers. Only one end of each fiber is guided for readout, and to improve the photon yield, the fiber reflector is applied at the other end. The handling of readout end is similar as the pre-shower, each end is connected to clear fiber through a connector device, then glue all the other end of clear fibers to a bundle, and finally coupled this fiber bundle to the cathode window of a 1.5 inch PMT.

7.2.3 Scintillator Pad Detector (SPD)

The work of our Ecal group also includes the SPD test. The SPD only exists in SIDIS, including Large-angle SPD (LASPD) and Forward-angle SPD (FASPD). The main purpose of SPD is to reduce the calorimeter-based trigger rates of high-energy charged particle by rejecting photons, which is based on the simple idea that low interaction cross section of high energy photon in scintillator. The SPD is segmented to 60 parts with a fan shape design perpendicular to the beam direction to reduce the trigger rate of each SPD, the sketch of which could be seen in Fig.7-7.

The function of LASPD is not only to reject the photon trigger but also to offer time information of charged particle hitting in Large-angle detector. The 150 ps time resolution goal is required to provide time-of-flight for particle identification, and one challenge of this goal is that the signal is only read out by PMT at one side. To achieve high photo-electron statistics, the use of WLS fiber is impossible, we have to couple the PMT to the scintillator directly. Considering the high magnetic field, fine-mesh PMT would be a good

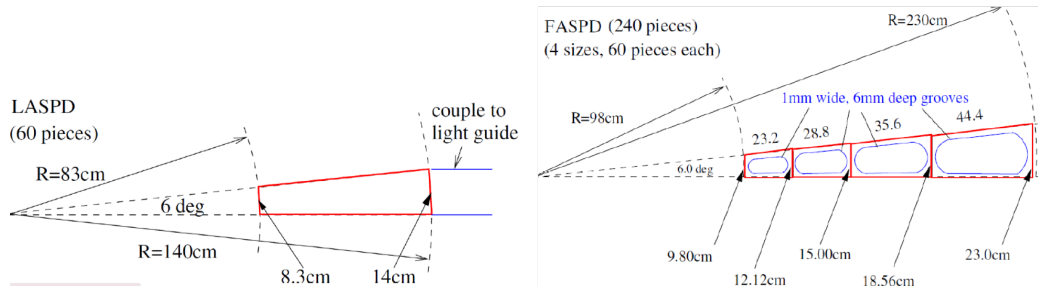


Figure 7-7: Left: The sketch of one LASPD sector. The length of SPD is 56cm. Right: The sketch of one FASPD sector. Readout is similar as preshower, WLS fibers embedded in grooves.

choice.

The original thickness of LASPD design is 2 cm, which is a balance between light yield and photon rejection. The thicker scintillator will improve the time resolution significantly, but it also makes the photon rejection low efficient because photon in thicker scintillator has more possibility to create the electron/positron pair. However, the 150 ps time resolution is the baseline, we must satisfy it firstly, then consider the photo rejection. The time resolution test of LASPD will show in section A..

For FASPD, it only needs to reject photon. We plan to use 5 mm thickness scintillators based on a balance between the light yield and the radiation. The readout of FASPD is similar as preshower through WLS fibers. To further suppress the rate, each azimuthal sector is segmented to 4 parts in the radial direction.

The SPD is new detector that used for photon rejection, and it needs efforts to verify its performance. The challenge of SPD design is mostly focus on the light yield vs. performance. More work on simulation and test will be performed in the future.

Chapter 8

Electromagnetic calorimeter principle

The design and performance of ECal detector based on the property of each component and how it works. The developing of detector is also an important topic in particle physics, and it's a combination of other related technique. Some technique developed by experience from experiment, and some from the theory calculation. Here is just a brief description of detector physics including what we care mostly in our design, and the discussion to improve the energy resolution by increasing the light yield.

Understanding detector is the first step to improve it. This Chapter will describe the physics of several important components used in ECal, the reason why we choose them, and what we did to improve the performance of them.

8.1 The Electro-magnetic Calorimeter

The Electro-magnetic calorimeter (ECal) is used to deposit the whole energy of photon and electron. When the high energy electron or photon enters the ECal, electron loses its energy mainly through bremsstrahlung and creates a high energy photon, photon will create an electron and a positron through pair production process. The combination of these two processes is called electron-photon showers. It continues until the energy of the pair-produced electron and photon drops below critical energy. A very important parameter of ECal is radiation length X_0 , that is equal to the mean distance over which a high-energy electron loses all but 1/e of its energy by bremsstrahlung[66]. The total radiation length used in SoLID Ecal is $20 X_0$, result in an only 2% energy leakage of electron

in simulation.

The photon and e^+/e^- with same energy have same signal in calorimeter, and we can't distinguish them from the ECal itself. But it could be used to distinguish the hadron, such as pion. The pion only lose a small part of its energy through ionization, and could be distinguished from electron/photon by the magnitude of signal. For the PID purpose, a good energy resolution is required.

The most important character of calorimeter is energy measurement, and the measurement error could be evaluated by the energy resolution, described as σ_E/E . For the energy resolution calculation and simulation, the expression is written as [67]:

$$\frac{\sigma_E}{E} = \frac{p_0}{\sqrt{E}} \oplus p_1 \oplus \frac{p_2}{E} \quad (E \text{ in GeV}) \quad (8-1)$$

where p_0 is statistical fluctuation of signal(photon) detection, which mostly influents the energy resolution; p_1 represent the influence from calibration and energy leakage; p_2 is a constant that not related to the energy, including the electronics noise; the mark \oplus is the quadratic sum, which means these three items have independent impact to the overall energy resolution. The simulation result of SoLID ECal energy resolution is shown in Fig.8-1, and fitted by this function[68].

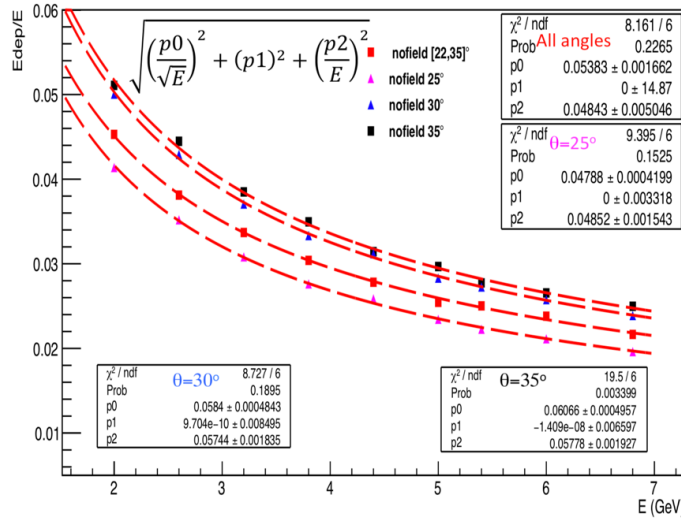


Figure 8-1: The simulation result of ECal energy resolution using electron beam with specific energy. The different angle means the different hit position in the ringlike ECal. Results shows smaller angle has better energy resolution. The result is fitted by the energy resolution function, and shows a good fitting. A $7.2\%/\sqrt{E}$ energy resolution is achieved for the total angle fitting.

There are two types of calorimeter: homogeneous calorimeter and sampling calorimeter. The homogeneous calorimeter has only one material that have both absorbing and sensitive property. The sampling calorimeter has at least two material in which the material that produces the particle shower as absorber is distinct from the material that measures the deposited energy. The absorber generally used is lead, and the sensitive material is scintillator. Since the homogeneous calorimeter will measure all the energy deposited in calorimeter, which means a lower p_0 value in calculation, so it has a better resolution than sampling calorimeter. However, there are some experiments that energy resolution is not the key index, the sampling calorimeter will be a better choice for its low price and good radiation hardness. The sampling calorimeter has been developing for decades, and has achieved a $4\%/\sqrt{E}(GeV)$ energy resolution[69] and will be widely used in more and more experiments.

8.1.1 The light yield of SoLID Ecal

The SoLID ECal is a combination of several components and each component will contribution a linear effect the total light yield. The final light yield will be influenced by these factors:

1. Total Energy deposit in scintillator.
2. Scintillation photons number generated per MeV.
3. Light collection efficiency from scintillator to fiber.
4. WLS efficiency from blue light to green light.
5. Trapping efficiency in WLS fiber.
6. Attenuation length in WLS fiber.
7. Light loss from WLS fiber to clear fiber.
8. Attenuation length in clear fiber.
9. Quantum efficiency of PMT.

Each factor is important and must be considered to improve the light yield. For the ECal prototype study, we will involve these factors to achieve a better light yield.

8.2 Scintillator

The scintillator detector is the most commonly used particle detection device in nuclear and particle physics. Some scintillators are also regarded as calorimeter, such as the inorganic scintillator NaI. The scintillator that we're talking about here in particular refer to the plastic scintillator, which is widely used in almost every experiment. The plastic scintillator could be built in any shape and size, have good light yield and fast time response.

Any charged particles passing through it will leave a scintillating light. The plastic scintillator consists of basic material, scintillating material and wavelength shifter solvent. The charged particles excite the electron of atoms and molecules making up the scintillator through ionization, and de-excite to create the low energy photon. However, the emitted light is in the ultraviolet range and is not sensitive to PMT. To obtain light output in the maximum-sensitivity wavelength range of the photomultiplier (typically 400nm), several fluorescent agents are added to the basic material acting as wavelength shifters[70].

The scintillator has a very fast Time Response. Scintillation detectors are fast instruments in the sense that their response and recovery times are short relative to other types of detectors. This faster response allows timing information, i.e., the time difference between two events, to be obtained with greater precision. Its fast recovery time also allow scintillation detectors to accept higher count rates since the dead time, i.e., the time that is lost while waiting for the scintillator to recover, is reduced[71].

The scintillator is also used in LASPD to get the time information, which requires a better than (150ps) time resolution. A good time resolution need high light yield of scintillator to avoid fluctuation of photons arriving time. For the long distance scintillator, attenuation length is also an important factor, and the far end has a relative worse time resolution.

Here is the list of requirement for scintillator detector:

- High conversion efficiency from energy to fluorescent radiation.
- Good electron collection efficiency.
- Emission spectrum sensitive to PMT response spectrum.
- Fast rise time and response time, to achieve a good time resolution.
- Long attenuation length.

- Good radiation hardness.

The table 8-1 shows the property of scintillator HND-S2 used in SoLID ECal, made by Gaoneng Kedi Co., China. The property of this scintillator type satisfies our basic requirement, and used in the prototype construction.

Base material	polystyrene
Density	1.05 g/cm ³
Refractive index	1.59
Light output(% Anthracene)	50-60
Attenuation length	>200 cm
rise time	0.7 ns
Attenuation time	2.8 ns
Wavelength of maximum emission	423

Table 8-1: The parameters of plastic scintillator HND-S2 used in ECal SoLID.

8.3 Wave length shifting(WLS) fiber

The Wave Length Shifting(WLS) fiber is a kind of fiber contain fluorescent material in the core. The size of WLS fiber is tiny and could be bent to any shape and placed in any position. It help export the light generated in detector to the readout device.

The WLS fiber could shift the incident photon to a lower energy photon, and the incident angle changed in this process. If the angle satisfy the condition of total reflection between the core and cladding, the photon will be always trapped in the fiber, and sent to fiber end for readout. If replacing by an ordinary clear fiber, for an incident photon, since the path of light is reversible, it will not be trapped, and exits the fiber with same angle. The Fig.9-2 shows how the fiber works. The critical angle α of total reflection could be calculated as:

$$\sin\alpha = \frac{n_2}{n_1} = \frac{1.49}{1.59} = 0.937 \quad (8-2)$$

where we could get the angle α is 69.6°, any photon that the angle is larger than that value will be trapped. The trapping efficiency is defined as the ratio of solid angle, described as:

$$t = \frac{2\pi(1 - \sin\alpha)}{4\pi} \times 100\% = 3.15\% \quad (8-3)$$

The value t means that only 3.15% of photons that after shifting could be trapped in fiber, and the real situation will be much worse, because this value needs to multiply the fiber shifting efficiency of fluorescent material. To trap more light in fiber, a multi-cladding fiber is designed with the other cladding layer. The refractive index of the second cladding is 1.42, and enhanced the trap efficiency to 5.35%.

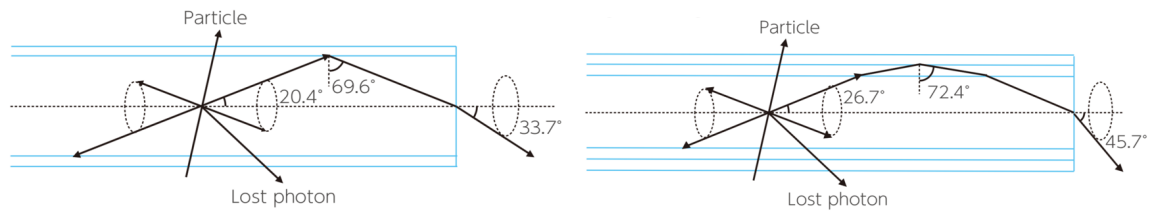


Figure 8-2: Left: single cladding transmission principle. Right: multi-cladding transmission principle.

Actually, the incident light could be considered into two kinds: after shifting and without shifting. The light unshifted still could transmit in fiber, but will lose a portion through refraction when hitting the cladding, especially for very long light transmission. All the photons in fiber have the possibility to shift, including the photons have shifted but not satisfy the angle of total reflection, and this process dominates the number of shifting photon. Similarly, even the shifted photon could be re-shifted or absorbed by atom in fiber, which lead to an attenuation, evaluated by attenuation length(1 m -3 m). The above content is how the WLS fiber works.

An air gap must exist between fiber and scintillator to make the photon reflect as total reflection, so the fiber is placed loosely in the holes or grooves in ECal. Other connections are between WLS fiber to clear fiber and clear fiber to PMT. Since the incident angle at the fiber end is small, the total reflection could not happen, so the air gap between them is OK.

The sensitive absorption spectrum of PMT (peak 420 nm) matches well with the scintillator emission spectrum, but the light guide-out through WLS fiber changes this good match. The WLS fiber transforms the light from blue to green, and the green light is not as sensitive as blue light for PMT. We didn't find any PMT tubes are sensitive to green light, and the other choice is the orange light (600 nm) sensitive PMT[72], and it

works worse than blue sensitive PMT for green light collection. So the light mismatching of using WLS fiber is inevitable now.

The PMT is placed outside the detector package, and long fibers are required to transmit the photon created in ECal to PMT. Since the WLS fiber has short attenuation length, the clear fiber with longer attenuation length is applied to convey the photons signal.

8.4 PMT

The Photo-Multiplication Tube(PMT) is a sensor to transform the photon yield to charge signal. It's a very sensitive photon sensor, which could reach 10^7 multiplication factor, even a single photon could be detected. It also has a fast response time, and some kinds of PMT could reach a very high time resolution. The Fig.8-3 shows the structure of PMT and how it works[73].

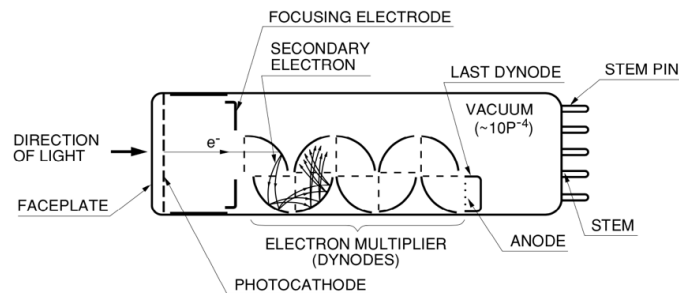


Figure 8-3: The structure of an ordinary PMT. The structure of PMT from left to right: faceplate window, photo-cathode, focusing electrode, dynodes and anode.

A high voltage must be supplied to the PMT, and is distributed between dynodes by the HV divider base. A photon hitting the faceplate window, will kick out an electron via the photoelectric effect. Then the electron is accelerated and fly to the focusing electrode because of the electric field. When it hits the firs dynode, it transfers some of its energy to the electrons in the dynode and causes several secondary electrons to be emitted. These electron will be accelerated towards the second dynode and create more electrons. If a PMT has K dynodes, and after multiplication process, N^K electrons will be collected, in which the number N is the average electron number that an electron hit out and influenced by the voltage between dynodes. Finally the multiplying electrons are collected in anode.

There are four types of PMT used in ECal and SPD, each type has its special property:

- Ordinary head-on PMT. This is the most common PMT with a wide faceplate window, has good stability and high multiplication coefficient. Used in the readout of shower detector, fiber bundle is coupled to its larger cathode window. It's the cheapest PMT of these four types PMT, and the model Hamamatsu R11102[74] will be selected.
- High time resolution PMT. The basic structure is same as the ordinary head-on PMT, to improve the time resolution, the structure is optimized to minimum the time fluctuation. The improvement including a focusing lens to decrease transition time deviation and a more compacted dynode structure. This PMT is only used in the time resolution test of LASPD.
- Multi-anode PMT(MaPMT). The MaPMT has multi-anode at the faceplate window, the dynode has metal channel structure. One problem of this dynode structure is it has cross talk effect, which means the multiplied electron may leak to the channel near it. Test result shows about a 1% level leakage for other channels that around the central channel with light input. Because the average price of each channel is cheaper than other PMT type, and also considering its small faceplate window of each channel, this type of PMT will be used in preshower and FASPD that read out by several fibers.
- Fine-mesh(FM) PMT. The main advantage of this type PMT is it has a very short distance between dynodes and dynode to the photocathode, which make it could work in the presence of a high magnetic field. It also has a large effective area, high gain, and small timing jitter, which is suitable for LASPD readout.

The design of HV divider also influences the property of PMT. To acquire a high gain with same HV, following the gain calculation, if the voltage between dynodes is equal, the PMT will get the highest gain. The circuit diagram of average voltage-divider is shown in Fig.8-4, which is used now as voltage-divider in cosmic ray test. It works well if the number of photo-electrons below 1000, if the number increases, the linearity of this design will get worse because the electron accumulation between later dynodes will form a reversed electric field and weaken the electric field. To achieve good linearity, the voltage-divider circuit is designed to tapered configurations at both the earlier and latter

dynode stages. This better linearity divider will be designed and tested in future. There is also a design for better time resolution, an additional voltage is added between cathode and focusing electrode to accelerate the electron to decrease transmission time deviation.

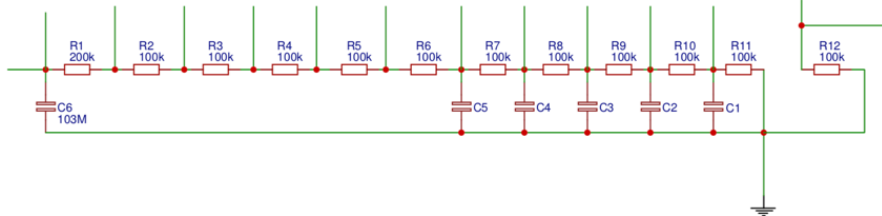


Figure 8-4: The average type design of voltage-divider circuit.

8.5 Summary

The purpose of detector study is trying to measure the signal and make this measurement precise. The detector design is based on our our understanding. Once the design is decided, the next work will be the optimization of detector, and test if these detectors satisfy the design requirement.

The ECal or scintillator detector is a combination of several components. The requirement of good energy resolution in ECal and time resolution in SPD seems similar: a good light yield. The main factor influence the light yield in the whole detector package would be:

1. The light yield efficiency of scintillator.
2. Photon collection efficiency from scintillator to PMT.
3. Photon to electron transformation efficiency of cathode of PMT.

Chapter 9

Material Selection of ECal Prototype and assembly

Once the design of detector is decided, we must build a module to bring out the design. To ensure the quality of ECal and reach the desired performance, the material must be selected carefully. This chapter will describe the material selection that used in Ecal module, including the comparison and test. The machining process of these material and assembly process are also included.

As described in previous chapter, the light yield of detector show a main character of ECal performance. The light yield could be counted as Number of Photon-Electrons(NPE) in PMT. The photon statistics is an importance source contributing to the calorimeter resolution. The final light yield read out by PMT is not only dependent on the scintillator efficiency that generates the photons, but also the collection efficiency of the whole detector.

The light yield of preshower is much lower the shower detector, to collect enough photon to satisfy statistical need, more careful care is taken to preshower, including better material.

9.1 Scintillator

The light yield of scintillator is vital to the final photon readout. We compared two batches of scintillator from China National Control System Engineering Co.(CNCS) and Gaoneng Kedi Co.. The test is performed by cosmic ray test of preshower scintillator. Comparison result show the Gaoneng Kedi Co. has a slight 5% more light yield, and the light yield consistency of CNCS batch is worse, so the scintillator of Gaoneng Kedi Co. is selected. This scintillator is also applied for the selection of SPD and scintillator in shower detector.

All the scintillators used in ECal are made by Beijing Gaoneng Kedi Co. with the model HND-S2[75], it has better cost performance and is the best made-in-China choice. Two batches of scintillators are received in our Lab. Based on our suggestion, the second batch with enhance formula that adding more scintillating medium get an improved light yield. Test shows the enhanced scintillator has more 26% light yield.

9.2 Reflective layer

A reflective layer must be added between lead and scintillator to improve light collection. The lead will absorb the low energy photon that pass through, and the adding reflector will reflect the photon back to scintillator. Because the scintillator layer is very thin(1.5mm), photons will be reflected many times before reemitted by scintillator or collected by fiber.

Besides the requirement of high reflectivity, there are also two other important considerations of reflector: thickness and friction coefficient. Since there are nearly 400 pieces reflector in a signal module, even if a little increase in thickness will enlarge the thickness significantly and the total length in design is restrained. For the friction coefficient, since the module is only hold by six rods at the corner after installed in detector frame, the fraction between layers must large enough to keep the whole module stable.

Several materials with high reflectivity were considered, although all of them have very good reflectivity(above 90%), light will decrease rapidly between thin scintillator layers after several reflections. The cosmic ray test[76] is performed, the setup is shown in Fig.9-1, more detailed test setup information will be described Chap.10. The test result

is shown in Table9-1. Both diffuse and specular reflection material are tested, and no obvious difference is observed between these two reflection ways.

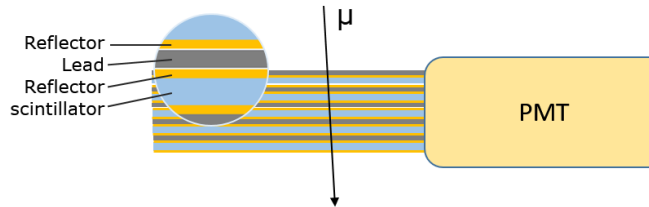


Figure 9-1: Five layers of reflector-scintillator-reflector-lead structure test setup. No fiber is used in this setup, and the scintillator is coupled to the cathode window of PMT for readout. The muon in cosmic ray will pass through all five layers.

These material in selection all have good nominal reflectivity and thin thickness. The printing paper is the ordinary white paper, cheap and good fiction efficient than all the other material. The other three kinds of material that Tyvek paper, powder painting and ESR, which is shown in Fig.9-2, are addressed and compared here.

9.2.1 Tyvek paper

The Tyvek paper is a synthetic polyethylene fibers material, a brand of Dupont company. It's waterproof and hard to tear, often used in packing and wrapping. It is commonly used to wrap the scintillator to enhance the light yield[77], and will be used to wrap the preshower and SPD. There are several thickness choice, and a thicker thickness always means a higher reflectivity. The thickness of tyvek paper is $100 \mu m$, which is same thickness as printing paper. Tyvek paper is our initial reflector choice, and is tested and applied

material	relative light yield
No reflector	0.85
Printing paper	1
Aluminum foil	0.97
Tyvek paper($100 \mu m$)	1.61
Powder coating	1.72
$3M^{TM}$ Enhanced Specular Reflector(ESR)	2.59

Table 9-1: 11

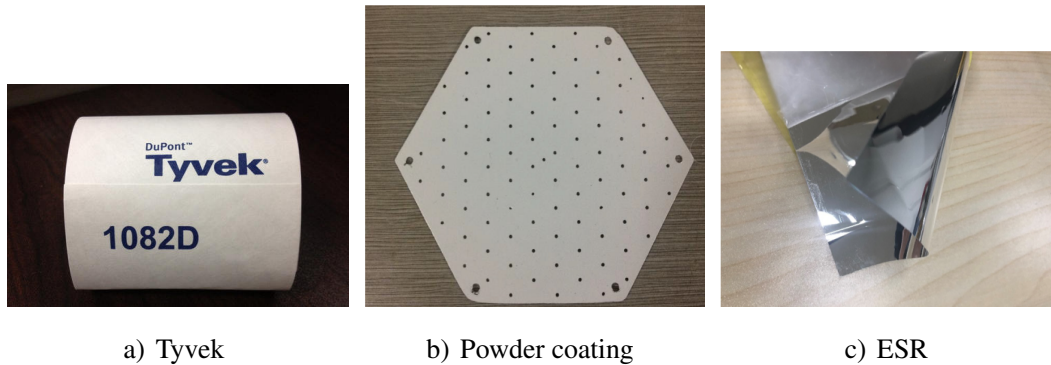


Figure 9-2: The choice of reflector layer.

in the construction of few initial modules.

9.2.2 Powder coating

Powder coating(or powder painting) is a type of coating that is applied electrostatically[78]. With the action of the electric field, the charged coating material is sprayed onto the surface of the workpiece, and the powder will be evenly adhered on the surface, forming a powdery coating. The main composition of powder coating is TiO_2 (titanium dioxide), fixed with bonding glue. The TiO_2 is the whitest and brightest of known pigments; it can also scatter UV rays[79]. The coating is painted directly to the surface of lead, as seen in Fig.(.), the finished piece shows a good appearance.

The powder coating reflector is already applied to the module construction, it has some advantages:

- Thin thickness. The thickness could reach as thin as $50\ \mu m$ of each layer. However, too thin thickness is not necessary for our purpose, to ensure the coating quality, the thickness in practical use is about $70\ \mu m$. And even with this thinner thickness, the light yield is higher than tyvek.
- High reflectivity. As seen in table 9-1, result shows $70\ \mu m$ powder painting has 18% higher light yield than $100\ \mu m$ Tyvek.
- Good quality in appearance. Good appearance shows on even surface and holes quality, and the coating on surface is very stable.
- Easy to assemble modules. No reflector is used in assembly, so it will save half of time in assembly.

- Lead protection. Lead is soft and flexible, the coating make the plate hard to be bent. The other reason is lead is harmful to health, and easily be adhered to the skin. This coating could avoid touching the lead directly.

The powder coating even has no significant disadvantage, the only con is light yield is not as good as ESR. With all the considerations described above, the powder coating will be the best choice and will be applied to the module construction.

9.2.3 3MTM Enhanced Specular Reflector(ESR)

The 3MTM Enhanced Specular Reflector(ESR) is a non-metallic mirror, which reflect more than 98% light across the visible spectrum, is widely applied in the backlight of an LCD display. The thickness is only 65 μm , and has perfect specular reflectivity. It seems like an ordinary plastic wrapping paper, and easy to punch holes. Result shows it has 50% more light yield than powder coating form the 5-layer test, and we are trying to figure out the reason. However the cost of ESR material is high, the price of only raw material is about 1000 CNY/module, which is higher than our expected. And the light yield could be compensated by the improvement of other issues. So it is not selected as reflector. And ESR is used as fiber end reflector, which will be shown in sector 9.3.2. We are also study the performance to wrap the scintillator.

9.3 Fiber

Two kinds of fibers will be used: WLS fiber and clear fiber. WLS fiber could trap the photons, and clear fiber transmit photons to PMT without significant attenuation. As seen in Fig.9-3, a one-to-one connector kit is used to transfer the light from WLS fiber to clear fiber. Since each fiber is readed out by one end, a fiber end reflector is adhered tightly at the other end. To ensure the reflection and transfer efficiency, the fiber end must be polished very carefully.

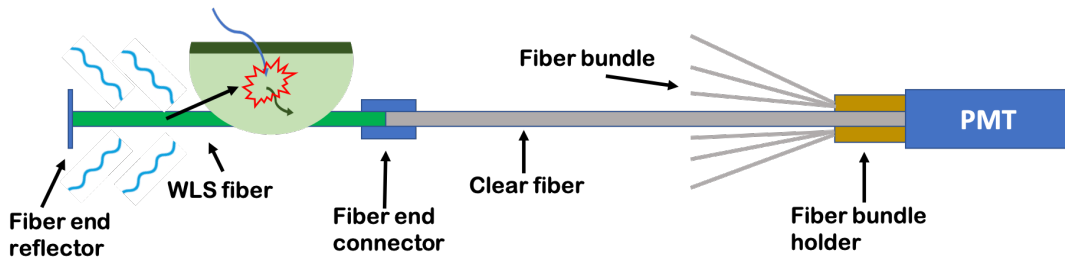


Figure 9-3: The sketch of photon collection process through fiber in shower detector. Photons are collected in WLS fibers, transport to clear fiber, and read out by PMT.

9.3.1 Fibers selection

Two types of 1mm diameter WLS fiber are considered: Y11 form Kuraray Co. and BCF91A from Saint Gobain Co., both are widely used in particle experiments for decades. The type of clear fiber in use is BCF98, made by Saint Gobain Co.. The clear fiber is similar as ordinary fiber, which is transparent, and has same structure and material, but no scintillating ingredient in core. The fiber information and comparison are shown in table 9-2.

Fiber type	WLS fiber		Clear fiber
	Y11(200) Kuraray	BCF91A Saint Gobain	BCF98 Saint Gobain
Wavelength shift	430 476nm	420 494nm	
Attenuation length(1/e)	>3.5 m		>8m from brochure (test shows worse result)
Radiation hardness	13% loss at 100k rad 20% loss at 700k rad	15% loss at 100k rad 50% loss at 700k rad	
Mechanical property	less bending loss		
Cladding	Single / Double cladding		Match the cladding type of WLS fiber
Price	High	Low	

Table 9-2: The three types of fibers used in ECal detector.

For WLS fiber trapping efficiency is a very important factor, which mean the ratio of photons is caught in fiber for a specific sensitive wavelength range. The trapping efficiency is about 3% ~ 3.5% [80][81] for single cladding fiber, the multi-cladding fiber that

with an additional cladding has 50% higher light yield. So the multi-cladding fiber will be a preference for the fiber choice, and these two kinds of fibers have similar trapping efficiency.

The main advantage of Y11 compared to BCF91A is the less bending loss. The Y11-S type fiber is mechanically stronger against cladding cracking at the cost of transparency and has less bending loss, especially when the bending radius less than 5cm. However this mechanical improvement make the attenuation length of Y11-S 10% shorter than standard type, which means more light loss in transportation process. We tested the bending loss for different bending radius, the result is shown in Fig.9-4. Results shows Y11 has a minor superior for bending radius between 6cm and 10cm. Because the fiber in preshower is bent in a 9 cm radius, so we prefer to use Y11 in preshower. In fact, 6% light loss seems still acceptable, more study will be performed to verify if Y11-S worthing the cost.

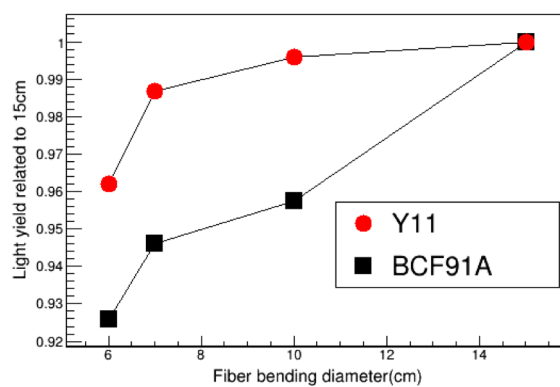


Figure 9-4: The relative light yield as a function of bending radius. We use the 15 cm bending radius as the reference. Y11 shows a less bending loss than BCF91A.

9.3.2 Fiber end mirror

Since the photons signal is collected from one end of fiber, a mirror reflector is applied at the other end. Only specular reflector, such as mirror, works in this case, diffuse reflector will change the angle of incident photons. To reflect the photon back with same incident angle, the fiber end must be polished finely, and the mirror must adhere to the end without gap. This is a very elaborate work, which needs align 96 tiny 1 mm fibers, and fix them to the mirror at the same time.

Several fiber end mirror with different methods are tried and tested, each has its Pros

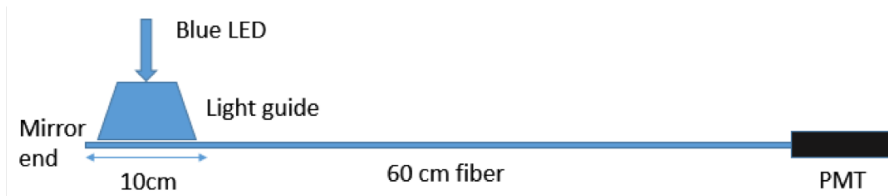


Figure 9-5: The sketch of mirror test setup. The mirror reflector is pasted at the end of fiber, only one fiber is tested at the same time. The light comes from blue LED, which could simulate the light generated from scintillator, is driven by a short pulse generator. 10 cm WLS fiber is exposed to the blue light through the light guide. To avoid the direct collection of blue light comes from LED, the incident direction of LED light is perpendicular to the fiber. The 60 cm length is corresponding to the fiber length in shashlik. The final light yield is evaluated by the output charge.

and Cons. For each method, we tested the improved light yield comparing with no mirror through the experiment setup shown in Fig.9-5. The light improvement is described as the light yield improvement percentage(0-100%) compared to no mirror. The two main methods are:

- Magnetron sputtering technique[82]. It uses a vacuum device to deposit the metal atom on the fiber end through heating. To achieve good reflectivity and stability, it needs three layers: (first layer, second, third)(ppt) This method will form a thin and uniform metal layer on the surface of fiber end. The advantage of this method is that the fibers could easily insert into the holes of module, and no need to fix the fibers. The best metal is Silver that has good reflectivity, the other choice is Aluminum that has good stability. The test result of Aluminum layer in ALICE experiment is only 25%[82] improvement. According to our quest, several batches of fibers with silver mirror are processed in different companies. The good batch could achieve 90% improvement, and the bad batch only reach 40%. The disadvantage is that the silver layer is liable to shed, and we have no confidence that if the layer has aging problem through sulfuration, since it's designed to work for several years. And the cost is higher than we expected.
- ESR. The most simple and direct method of adding mirror is pasting a whole reflector to all the end of fibers. However, it's hard to apply to module. 96 fibers must be aligned firstly, make sure no gap between the mirror and the fiber, then

glue them together. And the other end is polished while these fibers in modules, which is not as convenient as the metal mirror shown above. But it's the cheapest and stablest method. The best choice of reflector is ESR, and single fiber test shows that with good polishing and no air gap, a 90%+ improvement is acquired. For a whole module that all the fibers use one mirror reflector, a 80%+ improvement could be achieved.

We take many efforts with company to improve the quality of sputtering method, however, light yield improvement differs for fibers and batches in our test. When we suddenly found the ERS satisfy the mirror reflector requirement, we changed to this method and apply it to module building successfully.

9.3.3 Fiber connection and polishing

There are three situations using fiber connection: fiber and fiber end mirror, WLS fiber and clear fiber, fiber and PMT window. Each situation has its own connection method and processing method. To avoid light loss through photons transportation, the fiber end polishing quality must be controlled. The fiber is polished by a high-speed rotating milling cutter, which is made of diamond. The cutter could polish hundreds of fibers at the same time, and also guarantee good polishing quality. The Fig.?? shows the fibers of three situations after polishing. Here are the descriptions of these three situations:

- Fiber and fiber end mirror. The fibers are unconfined and a designed kit is used to fix the fibers when polished.
- WLS fiber and clear fiber. A special commercial connector kit is applied. It has three separated parts, WLS fiber and clear fibers are glued in the fiber hole of a separate part, then the fiber end is polished, and finally clutch three parts together. To make sure the fiber ends are connected tightly, the polishing depth and angle must be controlled precisely. The mounted fiber connector is shown in Fig.9-7, each kit could hold 10 fibers, and total 10 kits are needed for a shower detector readout.
- Fiber and PMT window. 96 fibers glued to a bundle in a holder, then polished them together. The flat holder end surface is couple to the PMT window.



a) Fiber and fiber end reflector b) WLS fiber and clear fiber c) Fiber and PMT window

Figure 9-6: a: Single fiber is fixed tightly in a kit. b: Fibers in connector. c: Fibers glued in a bundle, viewed by a microscope. The yellow part around the fiber is the optical glue.

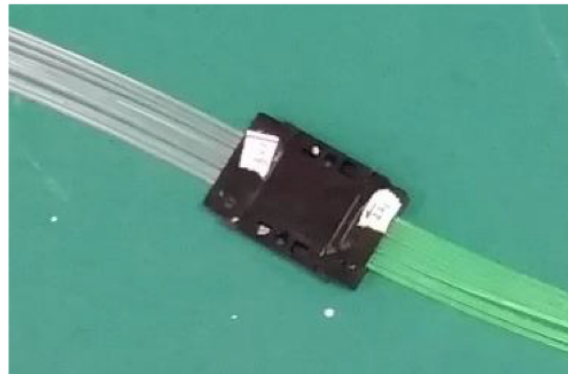


Figure 9-7: The picture of fiber connector kit.

9.4 Assembly

A special assembly tool is designed to align all the pieces of sheets and also compress the whole module to avoid air gap between sheets. As seen in Fig.9-8, three force sensors are used to monitor the force in the module. The force is imposed by pushing a big screw on the steel plate, and could be adjusted by three small screws.

To compress the module tightly, a total 5000N force is exerted through pushing the screws, and by adjusting three small screws to make sure each sensor has same force(1666N). As time goes on, the material will deform and shrink, and the force observed from sensor is getting less. To keep the original force, we need to repeat the adjusting process several times until the decrease of force is not significant.

To make the hundreds of layer stable, 2000N force needs to be kept in module while hanging on the detector frame. Once the module is compressed firmly, a part of the force imposed by compression tool will be transferred to six rods in shashlik detector. In this procedure, through turning the screws both in assembly tool and rods, total 2000N force is transferred to the six rods. A preliminary module with shashlik style is shape up now.



Figure 9-8: Left: Assembly tool for shashlik shower module. Right: The module in compression. Three pressure sensors are placed between the steel plated and shashlik detector to monitor the pressure.

To make the module tight-light and improve light yield from avoiding light leakage on the side of module, it's necessary to add coating on the side surface. After continuous trial, a mixture of TiO_2 powder and glue is applied as coating material, which has no air gap and convenient to handle the module. Comparing without coating, the coating have an additional 40% light yield improvement.

9.5 The material of shashlik prototype module

To verify the performance of material and the whole construction process, prototype must be built for test. We have built several shashlik modules in past several years' study process on ECal. At least 4 prototype modules are assembled in our Lab successfully, which could be seen in Table 9-3. The prototype module built posteriorly has better material and photon collection efficiency, and will result in a better light yield. Cosmic ray test result will be shown in next chapter.

Module No.	WLS fiber	Scintillator	Fiber reflector	Reflective layer	Coating
SDU #1	BCF91A-SC	Kedi	No reflector	Print paper	TiO ₂ +glue
SDU #2	BCF91A-SC	Kedi(enhanced)	Silver mirror	Print paper	TiO ₂ +glue
SDU #3	Y11-MC	Kedi(enhanced)	Silver mirror	Print paper	TiO ₂ +glue
SDU #4	BCF91A-SC	Kedi(enhanced)	ESR film	Powder coating	TiO ₂ +glue(1:1)

Table 9-3: The material list used in the shashlik prototype module.

9.6 Summary

We studied the material used in previous experiment, and also tested several new choice of material. The optimized material and component of ECal is shown in table??.

	Component	Material
Preshower	Scintillator	Kedi enhanced HND-S2
	Fiber	Y11-S-MC(multi-cladded)
	PMT	16ch-MaPMT
	Coating	Tyvek paper
Shower	Scintillator	Kedi enhanced HND-S2
	Reflective layer	Powder coating
	Fiber	BCF91A-MC or SC
	Fiber end mirror	ESR
	PMT	R11102
	Coating	$TiO_2 + glue$

The material selection overall consideration of property, cost and assembly. The initial purpose of experiment is pursuing the best performance, however high performance always means high cost. We could achieve good performance for single module prototype, but for batch production, cost is an important consideration. We could build a prototype in several months, but our purpose is building 2000 modules in two or three years, so the mass production and quality control will be a challenge.

Chapter 10

ECal prototype detectors test result

Once a new ECal prototype is built, the light yield of it will be tested by the cosmic ray test setup. This whole module test could show the combination property of all materials, and also the material machining quality in assembly process.

To get an accurate light yield, PMT for light readout is tested and calibrated to acquire its absolute gain and the linear range. The the prototype module coupled to calibrated PMT is tested by our built cosmic ray test setup.

The calorimeter response must reflect the energy deposited in it, and the beam test with fixed beam energy is necessary, which determines its property through energy resolution result. The discussion of beam test is shown in this chapter, and a preliminary beam test trial is also included.

The light yield of electron energy deposit could be evaluated from cosmic ray test result, base on the assumption that the energy deposit ratio is equal to the light yield ratio. We could get the energy deposit ratio from simulation, and once we get the cosmic ray test light yield, the light yield of electron will be calculated afterwards.

10.1 PMT test

PMT study is essential to the signal output and evaluate the light yield. The light yield could be evaluated as the Number of Photo-electron (NPE), which is calculated according to the ratio between the total charge collected in PMT and the single photo-electron (SPE) charge by the following equation:

$$NPE = Q/(e \times Gain) \quad (10-1)$$

where Q is total charge of a cosmic ray signal read out by Charge to Digital Converter(QDC, model CAEN V965)[83], e is electron charge, Gain is the amplification coefficient, and $e \times \text{Gain}$ equal to the charge of SPE. Once we get the gain of a PMT with specific HV, we could calculate the NPE. The NPE is an intrinsic character of detector, regardless of PMT property and HV.

The other important character of PMT is the linearity. Nearly thousands photons will be collected in PMT when high electron/photon depositing its energy in shower detector, and signal saturation will be a problem. When the saturation appears, the signal is not proportionable to the incident photons. One method to avoid saturation situation is using low gain. Lower gain means less electrons between dynodes, and help to increase upper limit of saturation. To check if the gain and HV divider design of PMT satisfy our requirement, test must be performed to get its saturation upper limit. The result is evaluated by the max PMT current of electron output, which is instantaneous upper limit.

Each PMT has its own parameter, and differs significantly between PMTs, which is caused from the process in manufacture and the tiny difference in material. So before using them, each one must be tested carefully to acquire its own parameter and check if its property satisfy the requirement. Here we focus on the head-on PMT test, the MaPMT test is similar as this test.

10.1.1 PMT test setup

The Fig.10-1 shows the PMT batch test system[84], which is designed for the test of more than 6000 PMTs used in LHAASO(Large High Altitude Air Shower Observatory) project. The test system could test 16 PMTs at the same time, including the gain, linearity, time resolution, cathode window scan and so on. The pulse light that simulate the scintillator light is generated from a blue LED, which is driven by a fast pulse generator. Then the light is divided into 16 bunches through fibers to realize the batch test. The whole system in controlled and monitored by a linux program to adjust the high voltage and decide the data taking. The test system will be adjusted and improved to test the PMTs used in ECal.

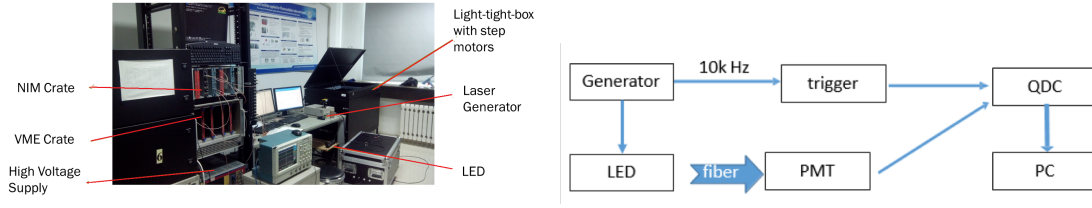


Figure 10-1: Left: The picture of PMT test system. Right: The PMT test system's schematic diagram.

10.1.2 SPE gain

The gain of single photon electron is the most basic character of PMT, which shows the amplification ability. To perform the gain test, we must get the single photon firstly. When voltage and duration time imposed on LED is low enough, the LED only emits out very dim light that even emits a single photon. The single photon detection needs the case that LED mostly emits single photon or nothing. The number of photons emitted from LED following the Poisson distribution:

$$P(N) = \frac{\lambda^N}{N!} e^{-\lambda}, \quad N = 0, 1, \dots \quad (10-2)$$

where N is the number of photons, the only parameter λ is the average photon number, which could be figured out from the fitting.

In the test, we adjust the HV imposed on LED until the signal events ratio compared to total trigger events is 0.1, which means $P(N = 0) = e^{-\lambda} = 0.9$ and $\lambda=0.105$. Then we get $P(N=1)=0.095$, and $P(N>1)=0.005$. So only 5% of the events that have signal are multi-photons events. Because the signal is weak, this test needs a relatively high gain and the lower range of QDC. A typical SPE spectrum is shown in Fig.10-2.

The SPE spectrum is fitted by the Landau convoluted with Gauss[85], described as:

$$f(q) = \sum_{N=1}^{20} C \frac{\lambda^N}{N!} e^{-\lambda} \frac{1}{\sqrt{2N\pi}\sigma} e^{-\frac{(q-Nq_0)^2}{2N\sigma^2}} \quad (10-3)$$

where q is the number of ADC channel that ready for fitting, q_0 is the peak value of SPE, σ is the width of SPE spectrum. The fitting will acquire the q_0 and the σ . The gain could be converted by q_0 through calculation:

$$Gain = \frac{q_0 \times Q_{ADC}}{e} \quad (10-4)$$

where Q_{ADC} is the charge of per ADC count of QDC, which is about 0.03 pC/count acquired from calibration.

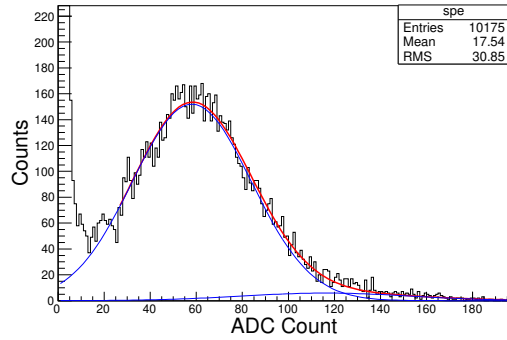


Figure 10-2: The single photon electron(SPE) spectrum readout by a precise QDC. The value in X axis is the raw ADC counts related to the peak of pedestal and could be converted to the charge. The left bins are the pedestal, the peak of which can't be seen in plot.

However this method only works for the high gain, and if we want to measure the low gain that will be used in the final working situation, the QDC and all other instruments are not precise to measure this weak signal of the SPE spectrum. There is an exponential relationship between gain and voltage, the gain of PMT roughly follow a simple equation:

$$Gain = A \times V^\beta \quad (10-5)$$

where A is the fitting constant, V is the high voltage, and β is the exponential efficient depend on each PMT. Fig.10-3 shows a typical relationship between the HV and gain.

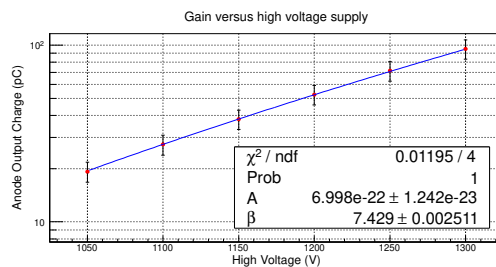


Figure 10-3: The relationship between HV and output charge(gain). The y axis is in exponential form.

Once the β value is acquired, taking a measured gain with a specific HV into calculation, we could get the gain of any HV. However this method only works for the gain is not very low. There is a large fitting error for the low gain, and the calculation result will have a non-neglectable error.

To minimum the aging problem caused from the high background, the gain of shower

PMT will be set to $10^4 \sim 10^5$, which is a rather low gain. Then to achieve a higher signal that in FADC readout range, the signal from PMT is connected to a pre-amplifier. This low gain requirement make it impossible to use the gain from calculation that has large error. In fact, we care more about the signal consistence of all PMTs rather than the accurate gain value of each PMT. When number N incident photons come to cathode, the output charge Q could be described as:

$$Q = N \times \eta \times Gain \quad (10-6)$$

where η is quantum efficiency, which is the ratio of photoelectrons number emitted from the photocathode compared to the number of incident photons, equal to NPE/N . For PMT type R11102, the typical value is 20% at 500 nm. Each PMT has a little bias on the value of η . To unify the signal output with same input light, a reference PMT will be used to make the other PMTs have same signal by adjusting their HV.

10.1.3 Maximum linear current

The maximum linear current of PMT is the max instantaneous current works in linear range. Only when the current of signal below this value, the output signal is linear to the incident light. Test must be performed to find out the maximum linear current value of each PMT, to make sure the PMTs work in linear range.

To measure the maximum linear current, a bi-distance method is developed in SDU. As seen in Fig.10-4, PMT is placed at far and near distance separately, and the light illuminating ratio λ is a constant between these two distances. If we increase the light intensity gradually, the signal of near distance that has larger light intensity will saturate firstly, and the far distance is still in linear range, which could be observed from the variation of ratio λ . The maximum linear current value is defined as the current of near distance when the ratio λ has a 5% variation.

The non-linearity deviation is defined as:

$$\delta = \left(\frac{Q_{near}}{Q_{far}} - \lambda \right) / \lambda \quad (10-7)$$

where the Q_{near} and Q_{far} is the charge of near and far distance separately, and λ is the light intensity ratio, which could be acquired from the fitting of linear range.

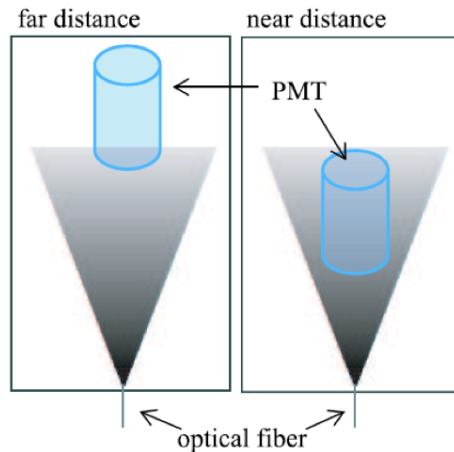


Figure 10-4: The sketch of bi-distance method. The light is given out from the point like light source, and the light intensity of near and far distance has a fixed ratio λ .

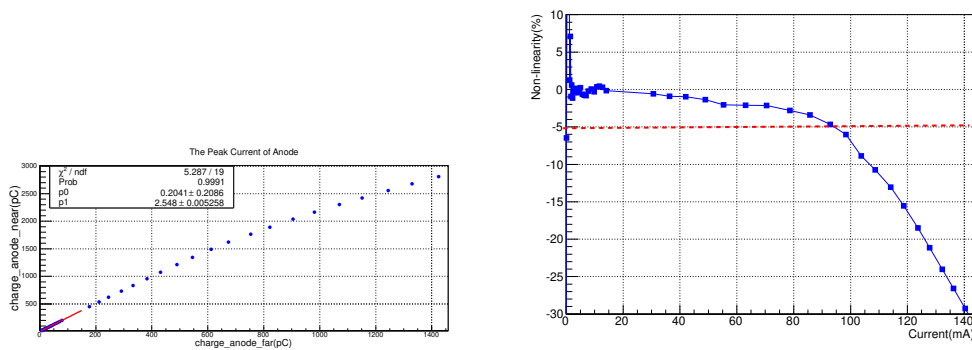


Figure 10-5: Left: Each points show the charge of near and far distance with increasing LED light intensity. The red line shows the fitting of the ratio λ . Right: The non-linearity of each point. The x axis is the max current of near distance, which is converted from the amplitude.

10.2 Cosmic ray test system

The cosmic ray test is the most convenient way to evaluate the performance of detector, and performed to study the light yield property of both the shashlik shower prototype and preshower. The dominant energy loss of cosmic ray, which are mostly muons, is ionization instead of electromagnetic shower. However the output signal still indicates other general property of calorimeter, especially the light yield. The rate of muon at sea level is

about $100 \text{ m}^{-2}\text{s}^{-1}\text{sr}^{-1}$ [7], and this high rate make the cosmic ray test efficiently.

10.2.1 Cosmic ray test setup and DAQ

For the shashlik shower ECal cosmic ray test, the test setup is shown in Fig.10-6. Two hexagon scintillators that have same lateral section as shashlik module are used as trigger, where A PMT is coupled directly to each scintillator to collect the photons signal. Since there is no tracking information in this setup, to make sure the cosmic ray get through the whole module and has similar tracking distance in detector, each trigger scintillator is placed at opposite side of shashlik module. All the detectors are placed in a large light-tight box to avoid the influence of ambient light.

A DAQ system is built for the cosmic ray test, which is shown in Fig.10-6. In this setup, the signal of shashlik detector is read out by a Flash Analog-to-Digital Converter(FADC), which could record the full waveform of signal. The signal of two PMTs coupled to trigger scintillator is sent to one channel of the discriminator separately, in which a -20 mV threshold is set. Only when the amplitude of scintillator signal exceed this given threshold, a standard NIM gate signal is generated as the output of discriminator. Then each gate signal is sent to a logic unit, which is set to "AND" function. If these two separate gate signal arrive at same time in coincidence, it means a cosmic ray particle pass through, the "AND" function is satisfied and the logic unit will generate a trigger decision signal to FADC. FADC will "freeze" immediately to record cosmic ray signal pass through shashlik shower detector. Finally, every triggered event is recorded automatically by a FADC control and readout script, and ready for offline analysis.

10.2.2 Flash Analog-to-Digital Converter(FADC)

The Flash Analog-to-Digital Converter(FADC) is essential to the signal recording and analysis in our test. The readout of ECal detector in JLab will also use another 250 MHz FADC, which is designed by JLab electronics group. The FADC that used here is the CAEN Mod. V1743[86], holding 16-ch 3.2GS/s Switched Capacitor Digitizer, having max capacity of 7 trigger events. It's a commercial multi-function digitizer, could work in waveform recording mode or the fast integral charge mode. The FADC even can be triggered by itself.

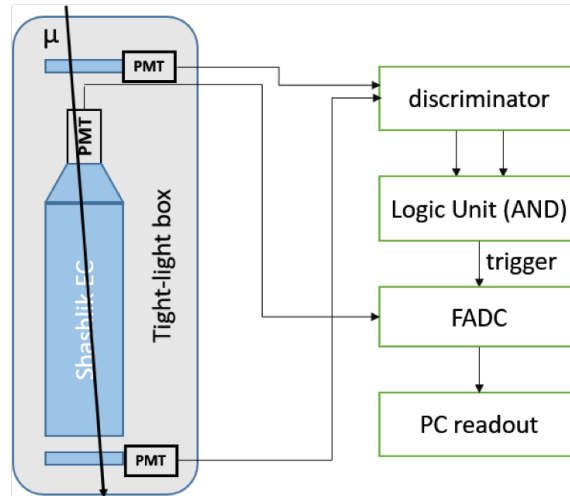


Figure 10-6: Circuit diagram of cosmic ray test setup and DAQ.

For the voltage measurement of signal, which is the vertical direction of waveform, the dynamic input range of digitizer is $2.5V_{pp}$ (DC coupled), and divided by 12 bits (total 4096 ADC bins). The DC offset is adjustable in ± 1.25 V range via a 16-bit DAC on each channel, which means it could measure the signal with max amplitude $+2.5$ V or -2.5 V.

For the time information of signal, which is the horizontal direction of waveform, it has a max sampling frequency 3.2 GS/s, equal to 312.5 ps for per point. Or choose a minimum 0.4 GS/s (2.5 ns) sampling frequency, with up to 1024 buffers of each event, a maximum $2.56 \mu s$ waveform could be recorded. The digitizer also has a built-in delay unit, so there is no need to use extra delay cable for the shashlik detector. The signal could be delayed by the so-called post-trigger delay, which finally provokes the freezing of the currently stored signal in the sampling capacitance cells. A typical scintillator signal read out by FADC is shown in Fig.10-7.

10.3 Cosmic test result

10.3.1 Shashlik ECal test result

The threshold of trigger amplitude is set to -20 mV, to ensure them are triggered by the real cosmic ray, rather than the random high rate noise that usually has lower amplitude. The trigger rate is very low, which is about 1 event/min, and a whole day is needed to take 1k events.

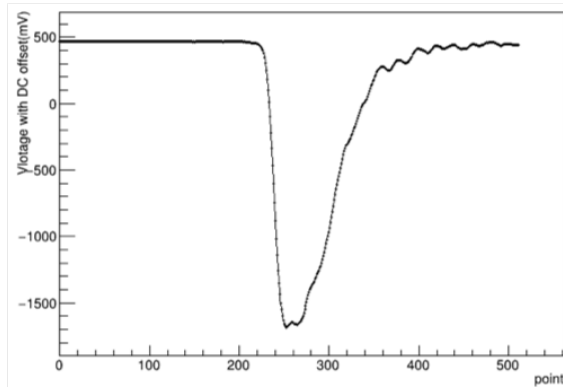


Figure 10-7: A typical single scintillator signal readout by FADC, total 512 points are recorded in this waveform.

The result is shown as the distribution of photon electron number. A typical NPE distribution of module #4 is shown in Fig.10-8. The signal is fitted by Gauss distribution, from which the mean value is 562.9 NPEs. Actually the signal should be fitted by the convolution of Gauss and Landau function. Since the NPE number is large, and the Gauss shape dominate the distribution, so the NPE distribution could be fitted by Gauss function approximately. As seen from the fitting plot, the χ^2 verified the good fitting of this approximation.

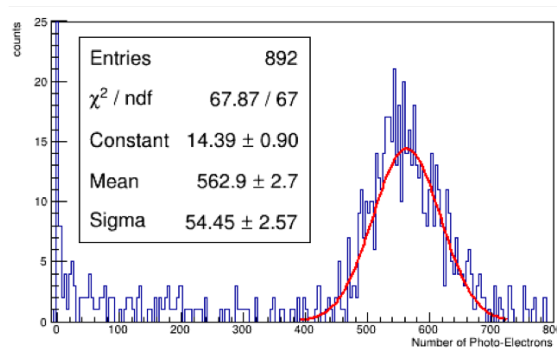


Figure 10-8: The NPE distribution of cosmic ray test for ECal prototype module #4. The peak at the 0 NPE is triggered by the noise coincidence of two trigger scintillators.

Table 10-1 shows the NPE result of four prototypes. Result shows the prototype module built posteriorly with better material has a better light yield (NPE). And the light yield improvement ratio is smaller than our expected ratio from individual material test, which shows the combination of all material as a whole module is much more complicated than individual material.

Module No.	NPEs	WLS fiber	Scintillator	Fiber reflector	Reflective layer	Coating
SDU #1	212.5	BCF91A-SC	Kedi	No reflector	Print paper	TiO ₂ +glue
SDU #2	413.8	BCF91A-SC	Kedi(enhanced)	Silver mirror	Print paper	TiO ₂ +glue
SDU #3	484.5	Y11-MC	Kedi(enhanced)	Silver mirror	Print paper	TiO ₂ +glue
SDU #4	563.2	BCF91A-SC	Kedi(enhanced)	ESR film	Powder coating	TiO ₂ +glue(1:1)

Table 10-1: The cosmic ray test result NPE of all four prototypes.

We could transfer this cosmic ray test result to the light yield of electron, base on the assumption that the energy deposit ratio is equal to the light yield ratio. From SoLID ECal simulation[87], the average energy deposit of muon in scintillator is 58 MeV, and the sampling ratio of electron deposit is 0.24, which means if a 1 GeV electron deposit its energy in ECal, 240 MeV will be deposited in scintillator. So the 563 NPEs in cosmic ray test is equivalent to 2330 NPEs for 1 GeV electron.

10.3.2 Preshower test result

The preshower scintillator is also tested wusing the same test setup, and the only difference is replacing the shower detector with preshower detector. This replacement shorten the distance between two trigger scintillators mush shorter, which means a higher cosmic ray trigger rate.

Two WLS fibers are embed in the groove of preshower scintillator to guide the light out for readout. To enhance the light yield, the scintillator is wrapped by tyvek paper, and the four WLS fiber ends are coupled to scintillator directly without clear fiber connection. As seen from Fig.10-9, the signal of preshower detector is not as high as the shower detector, so the gauss fitting not work, and the NPE distribution of preshower is fitted by the landau convoluted with gauss function. With 5 circles WLS fiber embed in preshower, about 70+ photo-electron yield is achieved, and consistent result is also presented from the separate test in University of Virginia (UVA).

10.4 Beam test

The beam test is vital to the determination of calorimeter's energy resolution. The test use pure high energy electron with known energy to hit the calorimeter, and usually

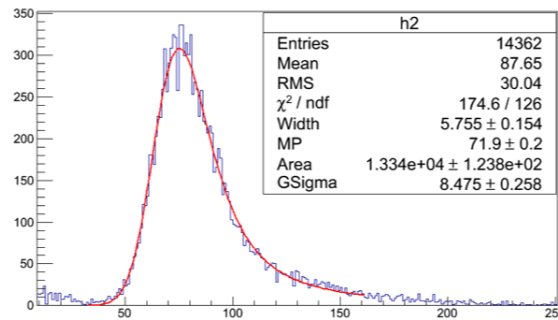


Figure 10-9: Cosmic ray test result of preshower detector with the distribution of photoelectron number(X axis: number of photon electron; Y axis: events counts). The light yield is fitted by the function that Landau convoluted with Gauss. The light yield is regarded as the peak of Landau part, which is shown in the fitting parameter table as MP.

several energy points need to be acquired to fit the energy resolution as the function of energy, which follows Eq.8-1. Several modules are already built, it's important to verify if these modules satisfy the requirement, which will decide the next step of prototype construction. If it satisfies the requirement, we will focus on the budget saving and batch production, and if not, more work will taken to the property improvement including using better material.

We have investigated several candidate laboratories, the beam test is an overall consideration of beam availability, other detector requirement, convenience and budget. A very rough beam test is initially performed in JLab Hall A, utilizing the beam setup of SBS GEM detector. However this test can't offer PID information and even if the electron could be identified, we don't know the electron energy, which make the test low efficient. More detail about this beam test will be shown in the following content.

We considered the potential beam test opportunity in Beijing IHEP facility and Fermilab. These facilities are considered firstly for their convenience and beam availability. Each one has its advantage and disadvantage:

- The Beijing IHEP facility E3 line uses electron beam(not single electron) hitting target to generate secondary low energy electron, could provides 100 MeV/c and 200 MeV/c electron or positron, and has much more superior detector conditions that could offer trigger, PID and position information. However, the 100 MeV/c and 200 MeV/c beam energy are a bit low for our purpose, and it's impossible to

fit the energy resolution trend by the only two points. The other problem is the low rate($2 \sim 3/min$) makes the test low efficient. Even so, simulation shows about 10% energy resolution for 200 MeV/c and 15% for 100 MeV/c, and once the beam test result is acquired, could be used to compare with simulation result and offer the simulation correction.

- For the Fermilab beam test, the electron beam condition is suitable for us. But we need to bring extra detector system, including tracking, PID, scintillator trigger detector and even the electronics.

We are prefer to perform the test in Fermi Lab, and pushing the beam test in Fermi Lab now. However, since the unanticipated coronavirus situation, the test plan is postponed. Once the Lab is open again to us, we will schedule the beam time, and prepared for the beam test.

10.4.1 A preliminary beam test in JLab Hall A

In the 2016 fall run of JLab Hall A, Super Bigbite Spectrometer[88](SBS) group perform a parasitic GEM[89](Gas Electron Multiplier) detector test, and our ECal group joined the test. The test utilize the GMp[90] experiment configuration that using up to $60 \mu A$ electron beam to hit 15 cm Liquid hydrogen target. As seen in the left of Fig.10-10, the detector package is placed at the left side the beam line with about 80° to the beam line. The scattered electron and other secondary particle generated from the target that in the center of hall will be detected.



Figure 10-10: Left: Top schematic view of Hall A and the location of the test equipment. Middle: The picture of detector package. Right: illustration of the detector setup. Three shashlik prototypes are stacked together, with preshowers are placed in front.

As seen from Fig.10-10, the detector package contains three main detectors, from front to back, they are:

- The front three scintillator paddles for charged particle trigger.
- The 5 layers of GEM detector for tracking.
- The calorimeter for energy measurement and coincidence trigger. Our shashlik is put beside the SBS group's calorimeter, to utilize the spare space of GEM tracking.

The trigger is set as the coincidence of front scintillator paddle and calorimeter, which means only charged particles are detected. With this trigger configuration, we set the threshold of calorimeter a little higher to reject the pion and restrain high background. This detector setup could detect all electrons with unknown energy. The events distribution as a 2D function of preshower and shower signal is shown in Fig.10-11. In the plots, the events are divided to three parts, and the part with lower shower signal and no preshower signal comes from the PMT noise in one module. We could identify the electron event clearly by the events both shower and preshower having signal. The part that has normal shower signal and no preshower signal may be the high energy photon.

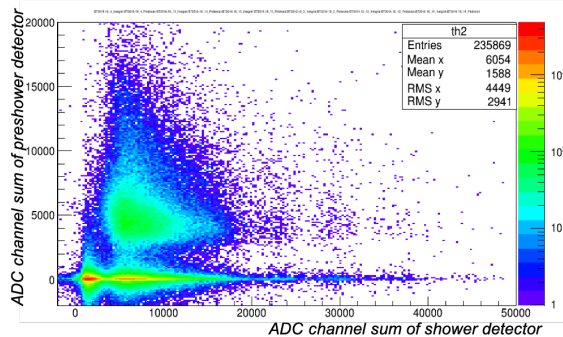


Figure 10-11: The two dimension events distribution histogram. The X axis is shower signal, and Y is preshower signal. In the histogram, the electrons are the events in the middle area. The high pile up events that near the ordinate origin comes from the PMT noise of one module.

This test is our first trial of ECal beam test, and inevitably, we encounter some problems, such as radiation damage to electronics and computer and the light yield loss as time goes by. If any problems happen, we can't go to the Hall in time but have to wait for the beam shut down gap, which make the test is low efficient. Although the test situation is not ideal, it also could accumulate the experience of test and get ready for the any

opportunity of future beam test.

10.5 Summary

This chapter describes the cosmic ray test of the ECal prototype, and we get a good light yield. With the absolute gain calibration of PMT, the light yield is evaluated by NPE.

Once we acquire the NPEs of cosmic ray test, according to the muon particle energy deposit in simulation, we could transfer this value to the light yield of electron, which could offer an evaluation of energy resolution through photon collection statistic. For the best 563 NPEs result, it is equivalent to about 2300 NPEs[87] for 1 GeV electron. This high light yield could significantly improve the energy resolution.

The beam test is essential to get the energy resolution of ECal. The beam test in Fermi lab is in preparation now, and the test will verify if the ECal prototype satisfy the energy resolution requirement.

Chapter 11

Conclusion and outlook

The SoLID program, as one of JLab 12 GeV detector upgrade, was proposed to a rich science program that require both high luminosity and large acceptance. The high luminosity and large acceptance challenge the detector design and trigger system. To verify or correct the generator used in simulation, data must be taken to compare with generator result.

The first part of dissertation described the measurement of inclusive π^0 cross section from the existing DVCS experiment E12-06-11 at 8.5 GeV and 11 GeV, and also compared this cross section result with modified Hall D generator.

The inclusive π^0 events are found in non-coincident time window that not related to the electron trigger, based on three vital factors: DIS trigger events, the long ARS time window and continuous beam structure. To reconstruct the single photon events from the pile-up signal, the calorimeter analysis is important to get a good time and energy information. With delicate care on calorimeter analysis, we acquire an improved energy calibration coefficient, and get an excellent 0.7 ns time resolution that could separate 4 ns beam bunches.

The cross section is acquired through comparing with simulation, based on the fact that the event yield ratio of data and simulation is equal to the cross section ratio. From error analysis, we achieved a global 5.5% systematic error, the result which is acceptable for this analysis purpose. However, the kinematic bins on the detector acceptance edge have both larger systematic error and statistical error, and more attention will be paid to the error of these bins.

The other purpose of inclusive π^0 cross section measurement is to check and correct the modified Hall D generator. Comparison result show the new result is larger than the generator result, and the ratio is dependent on the energy and θ angle. This higher ratio means the real trigger rate will be larger than the previous evaluated trigger rate. But considering that the high ratio kinematic bins are always have large energy and θ angle, in which the cross section is very low, so the rate difference mostly contribute from the low energy θ , the ratio of which is below 50%.

The π^0 kinematic acceptance is restricted by the calorimeter geometry, and the PbF_2 calorimeter has good time response to separate pile-up events but has low energy resolution, both will lead to the failure of low energy π^0 measurement. To detect low energy photon, a large acceptance calorimeter with low energy threshold is necessary, and it could be measured from SoLID data in future.

The shashlik style sampling ECal has been developed and used in many experiments based on the improvement of energy resolution over the past few decades. It has the advantage that lower price, good radiation hardness and moderate energy resolution, which is selected as the SoLID ECal design and even will be used in future EIC ECal.

In the ECal optimization and construction work, we successfully build several prototypes following its initial design with improved light yield. The whole design work includes material selection, machining process and the whole module assembly.

To test and improve the light yield of both material and prototype, we built a LED test setup and a cosmic ray test setup. Cosmic ray muon result shows 560 NPEs is achieved for best prototype, this light yield is equivalent to 2300 NPEs for 1 GeV electron, which satisfy ECal design requirement. A new prototype with best material, such as multi-cladding fiber and ESR as reflecting layer, is under construction, which is expected to achieve nearly 1000 NPEs.

We are pushing the beam test in Fermi Lab now, which could acquire an absolute energy resolution of prototype and verify if it satisfy the energy resolution requirement. This test will be performed once the beam line is reopen to user after this pandemic.

The prototype light yield study of ECal is just the first but most important step in ECal construction. In the following years, the design of final product optimized with cost, the batch production and the quality test system must be taken into consideration.

Appendix A

Large-angle SPD(LASPD) time resolution test

The Large-angle SPD work, as describe in Sect.7.2.3, is a part of our ECal group's work. The desired performance of 150 ps time resolution is the baseline to perform PID, we must satisfy it firstly, then consider the photo rejection. I spent months on the cosmic ray test and analysis of data, and get a very good time resolution result. Since the SPD test is not main part of my thesis work, just a brief description here.

A thicker scintillator will improve the time resolution significantly, but it also makes the photon rejection low efficient because of the more possibility to create the electron/positron pair. However, the 150 ps time resolution is the baseline of PID, we must satisfy it firstly, then consider the photo rejection.

The cosmic ray test of LASPD is performed in JLab, after the beam line test. The hit position on LASPD influence the time resolution, so tracking information is required, which is supplied by the GEM detector. Three other 5cm × 5cm × 30cm scintillator bars are used to offer trigger and also for the test of time resolution themselves that is also the system's time resolution. The signal of all PMTs are read out by both FADC and TDC.

A..1 "Three-bar test" of trigger scintillators

Before the test of LASPD, the time resolution of the test system must be tested firstly, and this error will influence the LASPD result, which will be subtracted in the final analysis. The time resolution of the trigger scintillator is tested by the "Three-Bar Cosmic Ray Method[91]". As shown in Fig.1-1 of trigger scintillator, this method must use three same scintillator bars, and the distance between adjacent bars is same. Each bar

has two PMTs read out at each side which means the average time of both sides readout could offset the hit position influence on time, so there is no need of tracking information in this method. Besides, the time resolution of 6 PMTs signal could be regarded as same because of the three identical scintillator bars. All these coincidences simplify the test and analysis.



Figure 1-1: The picture of 3-bar test setup. Each scintillator bar is read out by both sides, and the time t means the time of each PMT. A blue foam is placed between scintillators to make sure the gap distance is same.

In this method, we define the time T is:

$$T = \frac{t_{top} + t_{bottom}}{2} - t_{middle} = \frac{t_0 + t_3 + t_2 + t_5}{4} - \frac{t_1 + t_4}{2} \quad (1-1)$$

where the time t is not the original time get from TDC, but corrected by the time walk correction. If the time measurement has no error, the T value should be a constant. However, apparently, since the time measurement error is inevitable, the time T has a deviation σ_T , which is calculated as:

$$\sigma_T^2 = \frac{\sigma_0^2 + \sigma_3^2 + \sigma_2^2 + \sigma_5^2}{16} + \frac{\sigma_1^2 + \sigma_4^2}{4} = \frac{3}{4}\sigma_{PMT}^2 \quad (1-2)$$

Since the time of each scintillator is defined as $t_{scin} = (t_{left} + t_{right})/2$, the time resolution of scintillator is $\sigma_{scin} = \sigma_{PMT}/\sqrt{2}$. Taken it to the σ_T calculation, we get:

$$\sigma_T^2 = \frac{2}{3}\sigma_{scin}^2 \quad (1-3)$$

Once the σ_T is acquired, we could get the σ_{scin} value from this equation. The σ_{scin} is the time resolution of scintillator itself(related to PMT time resolution). The test result is shown in Fig.1-2, from which we get the time resolution of scintillator is 85.7 ps. If we use these scintillators as trigger, this value means the time measurement error of test system, and should be subtracted from the final time resolution result.

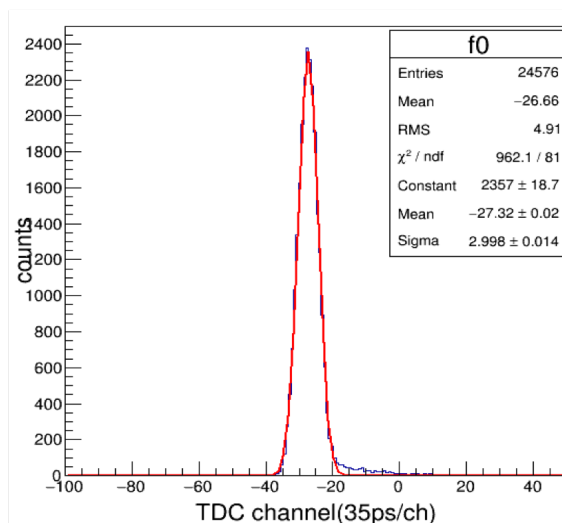


Figure 1-2: The time distribution of T, from which the time resolution σ_T is 105 ps(3×35).

A..2 LASPD test

After the test of the system, we add the LASPD to the test. As we can see from the left Fig.1-3, the LASPD replaces the middle bar in 3-bar test, and is placed in the middle between the top and bottom trigger bar. The signal is only read out by the wide side in SoLID design, which is the right side in the picture. The GEM detector is located under the scintillators, which could offer cosmic ray tracking information with $80\mu\text{m}$ position resolution.

We tested several relative positions between trigger bar and SPD, to test the time resolution in different position of SPD. The positions could be seen in the right of Fig.1-3. For the worst situation that particle hits at the SPD near the narrow side and transmits a long distance to the wide side, so if the time resolution in this situation still satisfy the requirement, the other positions will satisfy too.

The SPD test need hitting position information because the one side readout can't eliminate the time difference caused by position. So this test is more complicated than 3-bar test. To achieve a good time resolution, the analysis need a very dedicate care to the data. For time correction, there are two main factors: time walk(amplitude) and hit position. The whole process of this time resolution analysis includes:

- FADC cut on small signal.
- Time walk correction on one of the trigger PMT that determine the starting time.

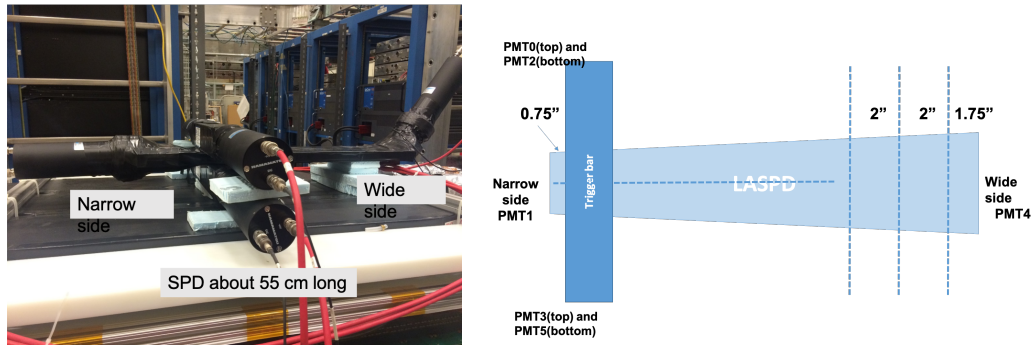


Figure 1-3: Left: the setup picture of SPD test. We use both end read in test, but the final analysis only use the wide side on the right. Right: top view of test setup sketch with different relative position of SPD and trigger bar.

The time of this PMT is special and corrected separately, because it decides the starting time. If you look into the plot that time vs. charge(FADC) like other PMTs, you can't find any relation between these two variables. This PMT is corrected by adjusting parameter of the correction function to get the minimum time resolution of T.

- Time walk correction on the other PMTs. ($time \propto 1/\sqrt{charge}$)
- Time correction based on hit position(only Y direction applied, which is along the SPD).

Similar as the 3-bar calculation, the time difference T to wide side is:

$$T = \frac{t_{top} + t_{bottom}}{2} - t_{wide} = \frac{t_0 + t_3 + t_2 + t_5}{4} - t_4 \quad (1-4)$$

And the time resolution at the wide side of SPD is calculated as:

$$\sigma_{wide} = \sqrt{\sigma_T^2 - \frac{1}{2}\sigma_{scin}^2} \quad (1-5)$$

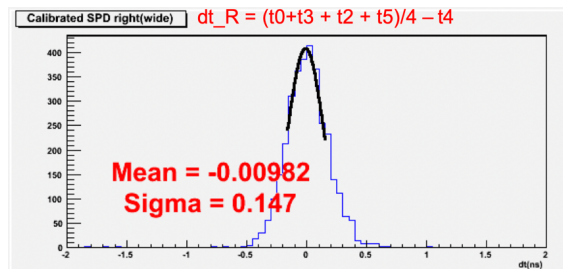


Figure 1-4: The time distribution of T, also equal to the measurement error of SPD wide side. The system error is contained in this result.

As we can see from Fig.10-11, the result shows the sigma of T is 147 ps. Taken this value into Eq.1-5, we get final time resolution of wide side readout is **134 ps**, less than 150 ps. So the conclusion is that the design satisfy the 150 ps time resolution requirement.

The time could be affected by the amplitude, the hit position of x and y. Since the statistics restriction, we only correct the amplitude and hit position in y direction. For the x direction, we did a rough cut that keep the events in the center of SPD, and if we could scan the SPD with a $1\text{ cm} \times 1\text{ cm}$ bin, the time resolution will get a little better.

This test shows the 2 cm thickness LASPD of cosmic ray test satisfies the 150 ps time resolution. However, the real beam run situation is much complicated and worse than the cosmic ray test. One problem is that the beam run has more low energy particle background. The other problem is since the PMT is placed under high magnetic field, the selection of PMT also need to be considered carefully, and fine-mesh PMT[92] would be a choice.

Bibliography

- [1] S. Durr, Z. Fodor, J. Frison, C. Hoelbling, R. Hoffmann, S. D. Katz, S. Krieg, T. Kurth, L. Lellouch, T. Lippert, and et al. Ab initio determination of light hadron masses. *Science*, 322(5905):1224–1227, Nov 2008.
- [2] Murray Gell-Mann. A Schematic Model of Baryons and Mesons. *Phys. Lett.*, 8:214–215, 1964.
- [3] R.P. Feynman. The behavior of hadron collisions at extreme energies. *Conf. Proc. C*, 690905:237–258, 1969.
- [4] J. D. Bjorken and E. A. Paschos. Inelastic electron-proton and γ -proton scattering and the structure of the nucleon. *Phys. Rev.*, 185:1975–1982, Sep 1969.
- [5] David J. Gross and Frank Wilczek. Ultraviolet behavior of non-abelian gauge theories. *Phys. Rev. Lett.*, 30:1343–1346, Jun 1973.
- [6] H. David Politzer. Reliable perturbative results for strong interactions? *Phys. Rev. Lett.*, 30:1346–1349, Jun 1973.
- [7] M. Tanabashi et al. Review of particle physics. *Phys. Rev. D*, 98:030001, Aug 2018.
- [8] B. Andersson, G. Gustafson, and G. IngelmanWalker. Parton fragmentation and string dynamics. *Physics Reports*, 97(2):31 – 145, 1983.
- [9] Cedric Lorce and Barbara Pasquini. Wigner distributions and quark orbital angular momentum. *Int. J. Mod. Phys. Conf. Ser.*, 20:84–91, 2012.
- [10] Sidney D Drell and Tung-Mow Yan. Partons and their applications at high energies. *Annals of Physics*, 66(2):578 – 623, 1971.

-
- [11] J. Ashman et al. An Investigation of the Spin Structure of the Proton in Deep Inelastic Scattering of Polarized Muons on Polarized Protons. *Nucl. Phys. B*, 328:1, 1989.
- [12] V.Yu. Alexakhin et al. The Deuteron Spin-dependent Structure Function $g_1(d)$ and its First Moment. *Phys. Lett. B*, 647:8–17, 2007.
- [13] E.S. Ageev et al. Measurement of the spin structure of the deuteron in the DIS region. *Phys. Lett. B*, 612:154–164, 2005.
- [14] R.L. Jaffe and Aneesh Manohar. The g_1 problem: Deep inelastic electron scattering and the spin of the proton. *Nuclear Physics B*, 337(3):509 – 546, 1990.
- [15] Andr Walker-Loud. Dissecting the mass of the proton. 2018.
- [16] Yi-Bo Yang, Jian Liang, Yu-Jiang Bi, Ying Chen, Terrence Draper, Keh-Fei Liu, and Zhaofeng Liu. Proton mass decomposition from the qcd energy momentum tensor. *Phys. Rev. Lett.*, 121:212001, Nov 2018.
- [17] Xiangdong Ji. Qcd analysis of the mass structure of the nucleon. *Physical Review Letters*, 74(7):1071–1074, Feb 1995.
- [18] Xiaochao Zheng. Precision measurement of neutron spin asymmetry a_1^n at large x_{Bj} using cebaf at 5.7 gev. *PhD thesis*, 2002.
- [19] A. Shalit and H. Feshbach. *Theoretical Nuclear Physics: Nuclear structure*. Theoretical Nuclear Physics. Wiley, 1974.
- [20] G A Miller. *Nucleon Resonances and Nucleon Structure*. 1992.
- [21] The SoLID Collaboration. Solid (solenoidal large intensity device) updated preliminary conceptual design report. 2019. <https://hallaweb.jlab.org/12GeV/SoLID/files/solid-precdr-Nov2019.pdf>.
- [22] Xiangdong Ji, Jian-Ping Ma, and Feng Yuan. Three-quark light-cone amplitudes of the proton and quark orbital-motion-dependent observables. *Nuclear Physics B*, 652:383–404, 2003.

- [23] H. Gao J.P. Chen et al. Beam time request for e12-10-006: Target single spin asymmetry in semi-inclusive deep-inelastic ($e, e'\pi^\pm$) reaction on a transversely polarized ^3He target at 8.8 and 11 gev. *JLab PAC*, 2008.
- [24] J. Huang W. B. Yan J.-P. Chen, Y. Qiang et al. Asymmetries in semi-inclusive deep-inelastic ($e, e'\pi^\pm$) reactions on a longitudinally polarized ^3He target at 8.8 and 11 gev. *JLab PAC*, 2010.
- [25] A. Kolarkar et al. Target single spin asymmetry in semi-inclusive deep-inelastic ($e, e'\pi^\pm$) reaction on a transversely polarized proton target. *JLab PAC*, 2011.
- [26] P. A. Souder et al. Precision measurement of parity-violation in deep inelastic scattering over a broad kinematic range. *JLab PAC*, 2008.
- [27] Y. X. Zhao. Parity violation in deep inelastic scattering with the solid spectrometer at jlab, 2017.
- [28] J. P. Chen, H. Gao, T. K. Hemmick, Z. E. Meziani, P. A. Souder, and the SoLID Collaboration. A white paper on solid (solenoidal large intensity device), 2014.
- [29] The ATHENNA Collaboration et al. Near threshold electroproduction of j/ψ at 11 gev. *JLab PAC*, 2012.
- [30] S.J. Brodsky, E. Chudakov, P. Hoyer, and J.M. Laget. Photoproduction of charm near threshold. *Physics Letters B*, 498(1-2):23–28, Jan 2001.
- [31] David E. Wisner. Inclusive photoproduction of protons, kaons, and pions at slac energies. *PhD thesis, Wisconsin U., Madison*, 1977.
- [32] Bhr et al. Herwig++ physics and manual. *The European Physical Journal C*, 58(4):639–707, Nov 2008.
- [33] Torbjrn Sjstrand, Stephen Mrenna, and Peter Skands. A brief introduction to pythia 8.1. *Computer Physics Communications*, 178(11):852–867, Jun 2008.
- [34] T Gleisberg, S Hoeche, F Krauss, A Schaelicke, S Schumann, and J Winter. Sherpa 1. , a proof-of-concept version. *Journal of High Energy Physics*, 2004(02):056–056, Feb 2004.

-
- [35] PING Rong-Gang. Event generators at besiii. *Chinese Physics C*, 32(8):599, 2008.
- [36] S. J. Patrick Riordan, Nguyen Dang Ton, Zhiwen Zhao, and Xiaochao Zheng. Comparison between wiser rates calculation and data from transversity and pvdis experiments. 2014.
- [37] E. Chudakov the GlueX Collaboration and A. Somov. Hall d trigger simulation. *JLab System and Infrastructure Design Review*, 2008.
- [38] Rakitha S. Beminiwattha. Hadron generator summary. 2015. https://hallaweb.jlab.org/DocDB/0002/000212/001/HallD_Gen_Summary.pdf.
- [39] Y. S. Tsai. Erratum: Pair production and bremsstrahlung of charged leptons. *Review of Modern Physics*, 1974.
- [40] V. M. Budnev, I. F. Ginzburg, G. V. Meledin, and V. G. Serbo. The two-photon particle production mechanism. physical problems. applications. equivalent photon approximation. *Physics Reports*, 15(4):181–282, 1975.
- [41] E. fermi,z.physik 29(1924)315.
- [42] Enrico Fermi. On the theory of collisions between atoms and electrically charged particles. *Electromagnetic Probes of Fundamental Physics*, Sep 2003.
- [43] S. Agostinelli et al. Geant4—a simulation toolkit. *Nuclear Instruments and Methods in Physics Research Section A: Accelerators, Spectrometers, Detectors and Associated Equipment*, 506(3):250 – 303, 2003.
- [44] J. Roche. Measurement of the Electron-Helicity Dependent Cross Section of Deeply Virtual Compton Scattering with CEBAF at 12 GeV. 2006.
- [45] K. Goeke, M.V. Polyakov, and M. Vanderhaeghen. Hard exclusive reactions and the structure of hadrons. *Progress in Particle and Nuclear Physics*, 47(2):401 – 515, 2001.
- [46] Mongi Dlamini. Measurement of hard exclusive electroproduction of 0 meson cross section in hall a of jlab with cebaf at 12 gev. *PhD thesis*, 2018.

-
- [47] Jozef Dudek et al. Physics Opportunities with the 12 GeV Upgrade at Jefferson Lab. *Eur. Phys. J.*, A48:187, 2012.
- [48] Christoph W. Leemann, David R. Douglas, and Geoffrey A. Krafft. The continuous electron beam accelerator facility: Cebaf at the jefferson laboratory. *Annual Review of Nuclear and Particle Science*, 51(1):413–450, 2001.
- [49] Reza Kazimi et al. CEBAF injector achieved world’s best beam quality for three simultaneous beams with a wide range of bunch charges. In *9th European Particle Accelerator Conference (EPAC 2004)*, 7 2004.
- [50] Jefferson Lab. Conceptual design report (cdr) for the science and experimental equipment for the 12 gev upgrade of cebaf. *jlabs.org*, 2005.
- [51] Basic instrumentation for hall a at jefferson lab. *Nuclear Instruments and Methods in Physics Research Section A: Accelerators, Spectrometers, Detectors and Associated Equipment*, 522(3):294 – 346, 2004.
- [52] K. Unser. A Toroidal DC Beam Current Transformer with High Resolution. *IEEE Transactions on Nuclear Science*, 28:2344, June 1981.
- [53] D. Higinbotham. Determination of the beam energy. <https://www.jlab.org/indico/event/197/session/3/contribution/12/material/slides/0.pdf>.
- [54] David. Hall a cryogenic target lower target stack assembly (spring 2014). Draw No. TGT-101-1010-0002.
- [55] Sauli Fabio. Instrumentation In High Energy Physics. pages 195–198, 1992.
- [56] M. Defurne, M. Amaryan, K. A. Aniol, M. Beaumel, H. Benaoum, P. Bertin, M. Brossard, A. Camsonne, J.-P. Chen, E. Chudakov, and et al. E00-110 experiment at jefferson lab hall a: Deeply virtual compton scattering off the proton at 6 gev. *Physical Review C*, 92(5), Nov 2015.
- [57] Bishnu Karki. BCMs and Charge For E12-060114:DVCS. 2017. Private communication.
- [58] Frederic Georges. Two pulses analysis - χ^2 thresholds. 2014. Private communication.

-
- [59] B. Wojtsekhowski. Hall a anuual report 2002. pages 31–34, 2002. <https://hallaweb.jlab.org/publications/AnnualReports/AnnualReport2002.pdf>.
- [60] R.T. Jones, M. Kornicer, A.R. Dzierba, J.L. Gunter, R. Lindenbusch, E. Scott, P. Smith, C. Steffen, S. Teige, P. Rubin, and E.S. Smith. A bootstrap method for gain calibration and resolution determination of a lead-glass calorimeter. *Nuclear Instruments and Methods in Physics Research Section A: Accelerators, Spectrometers, Detectors and Associated Equipment*, 566(2):366 – 374, 2006.
- [61] V. Breton, H. Fonvieille, P. Grenier, C. Guicheney, J. Jousset, Y. Roblin, and F. Tamin. Application of neural networks and cellular automata to interpretation of calorimeter data. *Nuclear Instruments and Methods in Physics Research Section A: Accelerators, Spectrometers, Detectors and Associated Equipment*, 362(2):478 – 486, 1995.
- [62] Argus: A universal detector at doris ii. *Nuclear Instruments and Methods in Physics Research Section A: Accelerators, Spectrometers, Detectors and Associated Equipment*, 275(1):1 – 48, 1989.
- [63] D. Kirkby W. Verkerke. RooFit users manual v2.91. https://root.cern.ch/download/doc/RooFit_Users_Manual_2.91-33.pdf.
- [64] Rooargusbg class reference. <https://root.cern.ch/doc/master/classRooArgusBG.html>.
- [65] Bishnu Karki. Systematic error evaluation of current and deadtime. 2018. Private communication.
- [66] M. Gupta; et al. Calculation of radiation length in materials. *PH-EP-Tech-Note*, 2010.
- [67] 谢一冈等. 粒子探测器于数据获取. 科学出版社, page 12, 2003.
- [68] Ye Tian (Syracuse). Update of solid ecal energy resolution simulation. 2017. <https://hallaweb.jlab.org/experiment/PVDIS/SoLID/EC/meetings/20170601/06012017.pdf>.

- [69] G. S. Atoian, V.V. Issakov, O.V. Karavichev, T.L. Karavicheva, A.A. Poblaguev, and M.E. Zeller. Development of shashlyk calorimeter for kopio. 531(3):467–480.
- [70] Boris Shwartz Claus Grupen. Particle detectors, second edition. *Cambridge*, page 126, 2008.
- [71] William R. Leo. Technique for nuclear and particle physics experiments. page 159, 1994.
- [72] Hamamastu head-on photomultiplier tube type. https://www.hamamatsu.com/eu/en/product/optical-sensors/pmt/pmt_tube-alone/head-on-type/index.html.
- [73] Photomultiplier tubes: Basic and applications. *Hamamatsu Photonics K.K.*, 2007. https://www.hamamatsu.com/resources/pdf/etd/PMT_handbook_v3aE.pdf.
- [74] Hamamatsu. Photomultiplier tube r11102, r11102-01. 2012. https://www.hamamatsu.com/resources/pdf/etd/R11102_-01_TPMH1324E.pdf.
- [75] Beijing Gaoneng Kedi Science and Technology Co. LTD. http://www.gaonengkedi.com/pro_show.asp?classID1=28&classID2=38&id=227.
- [76] Ang LI, Si-yuan FENG, Zhong-quan ZHANG, and Jian-bin JIAO. Optical performance studying for the R eflector used in shashlyk electromagnetic calorimeter. *Nuclear Electronics & Detection Technology*, 8:873, 2016.
- [77] M. Amenomori, X.J. Bi, and D. Chen. Study of the large Tyvek bag technique for the water Cherenkov detector in TIBET AS+MD. 6:411, 3 2015.
- [78] Wikipedia. Powder coating. https://en.wikipedia.org/wiki/Powder_coating.
- [79] Titanium Dioxide Manufacturers Association (TDMA). What is titanium dioxide? <https://tdma.info/what-is-titanium-dioxide/>.
- [80] Saint Gobain Co. Scintillating optical fibers. <https://www.crystals.saint-gobain.com/sites/imdf.crystals.com/files/documents/fiber-brochure.pdf>.
- [81] Ltd. Kuraray Co. Plastic scintillating fibers. https://www.kuraray.com/uploads/5a717515df6f5/PR0150_psf01.pdf.

-
- [82] P Cortese, T Peitzmann, AP de Haas, GJL Nooren, CJ Oskamp, A van den Brink, CG Ivan, R Kamermans, PG Kuijer, MAJ Botje, et al. Alice electromagnetic calorimeter technical design report, 2008.
- [83] CAEN. Technical information manual mod.v965/v965a. 2008.
- [84] Xu Wang et al. Setup of a photomultiplier tube test bench for lhaaso-km2a. *Chinese Physics C*, 40(8):086003, 2016.
- [85] I. Chirikov-Zorin et al. *Nucl. Instrum. Methods. Phys.Res.A*, 456:310–324, 2001.
- [86] CAEN. Technical information manual mod.v1743 & vx1743. 2015.
- [87] Ye Tian (Syracuse). Ecal digitization updates. 2020. Privatecommunication.
- [88] The super bigbite apparatus webpage. <https://www.eudet.org/e26/e28/e182/e283/eudet-memo-2007-11.pdf>.
- [89] Kondo Gnanvo, Nilanga Liyanage, Vladimir Nelyubin, Kiadtisak Saenboonruang, Seth Sacher, and Bogdan Wojtsekhowski. Large size gem for super bigbite spectrometer (sbs) polarimeter for hall a 12gev program at jlab. *Nuclear Instruments and Methods in Physics Research Section A: Accelerators, Spectrometers, Detectors and Associated Equipment*, 782:77 – 86, 2015.
- [90] J. Huang B. Moffit (spokesperson); et al W. Bertozzi, S. Gilad (spokesperson). Precision measurement of the proton elastic cross section at high q^2 . *Jefferson Lab PAC32 Proposal*, 2007.
- [91] Robert Steinman Ralf Gothe, Evan Phelps and Ye Tian. Clas12 forward time-of-flight at usc: A comprehensive update. 2009.
- [92] V. Sulkosky, L. Allison, C. Barber, T. Cao, Y. Ilieva, K. Jin, G. Kalicy, K. Park, N. Ton, and X. Zheng. Studies of relative gain and timing response of fine-mesh photomultiplier tubes in high magnetic fields. *Nuclear Inst & Methods in Physics Research A*, 827(aug.11):137–144.